Measurements of capillary pressure and electric permittivity of gas–water systems in porous media at elevated pressures

Application to geological storage of CO_2 in aquifers and wetting behavior in coal

Measurements of capillary pressure and electric permittivity of gas–water systems in porous media at elevated pressures

Application to geological storage of CO_2 in aquifers and wetting behavior in coal

Proefschrift

ter verkrijging van de graad van doctor
aan de Technische Universiteit Delft,
op gezag van rector Magnificus prof.dr.ir. J.T. Fokkema,
voorzitter van het College voor Promoties,
in het openbaar te verdedigen,
op dinsdag 16 oktober 2007 om 12:30 uur

door

Willem-Jan PLUG

civiel ingenieur

geboren te Katwijk aan Zee

Dit proefschrift is goedgekeurd door de promotor:
Prof.dr. J. Bruining

Toegevoegd promotor:
Dr.ir. E.C. Slob

Samenstelling promotiecommissie:

Rector Magnificus	voorzitter
Prof.dr. J. Bruining	Technische Universiteit Delft, promotor
Dr.ir. E.C. Slob	Technische Universiteit Delft, toegevoegd promotor
Prof.dr.ir. S.M. Hassanizadeh	Universiteit van Utrecht
Prof.dr.ing. R. Helmig	Universität Stuttgart
Dr. K.H.A.A. Wolf	Technische Universiteit Delft
Prof.dr.ir. J. van Turnhout	Technische Universiteit Delft
Dr.ir. F.J. Vermolen	Technische Universiteit Delft
Prof.dr.ir. F.B.J. Barends	Technische Universiteit Delft, reservelid

The research described in this thesis is performed at the Petroleum Engineering Section, Department of Geotechnology, Delft University of Technology and is carried out in the framework of the DIOC Water and the CATO project.

ISBN 978-90-6464-171-8

Printed by Ponsen & Looijen BV, the Netherlands
Cover design by Adriaan Geene

Voor Wilma

Contents

Chapter 1 Introduction

1.1 Reduction of CO_2 emission

The present world emission of CO_2 is 25 gigatonnes/year and this is still increasing. Scientific evidence is found for a strong influence on the climate by the emission of greenhouse gases. Atmospheric CO_2 is a "greenhouse gas", because it traps outgoing infrared and thermal radiation, thereby increasing near surface temperatures. Some evidence exists from climate modeling that increased atmospheric concentrations of CO_2 may be the main contributor to global warming, currently estimated as 0.3-0.6°C over the last 150 years [*Pruess*, 2003; *Ledley et al.*, 1999; *Orr*, 2004b].

To successfully face the observed climate change, a consensus must be formed for the reasons of climate change. Still, there is continuing debate on the magnitude and timing of impacts of greenhouse gases on global climate [*Orr*, 2004b]. Emission of greenhouse gases, e.g. carbon dioxide (CO_2) and methane (CH_4), from fossil fuel consumption is primary considered as the problem for the global heating. Sufficient scientific knowledge and social input has been compiled to take this problem very seriously. Global measures to stabilize the climate change are established at the Kyoto Convention of the United Nations [*Wikipedia*]. This convention aimed for "stabilization of greenhouse gas concentrations in the atmosphere at a level that would prevent dangerous anthropogenic interference with the climate system". In 1997, the Kyoto protocol is formulated and is started up in 2005. The protocol aims for a reduction of emission of greenhouse gases, such as, CO_2, CH_4, NO_x, HFK´s and PFK´s. The industrial countries have agreed to establish the reduction of emission of greenhouse gases, with 5% in 2005-2012 compared to 1990. Scientists agree more that to stabilize the CO_2 concentration, a reduction of 50% is necessary, i.e. 550 ppm. This requires more-efficient use of energy and development of a variety of new technologies [*Hoffert et al.*, 2002; *Orr*, 2004b]. The main challenges for CO_2 reduction can be summarized into [*CATO*]:

- Energy efficiency improvements (including efficient use of materials).
- Use of renewable energy sources, which emit no (or little) CO_2.
- Clean use of fossil fuels, by capturing and storing CO_2.

Because approximately one third of all CO_2 emissions due to human activity comes from fossil fuels used for generating energy, the application of clean use of fossil fuels is very attractive [*Capture and Storage*].

1.2 Geological storage of CO_2

Several organizations have initiated technology programs to assess and to develop techniques to reduce atmospheric disposal of CO_2. One of the most promising concepts involves disposal or sequestration of CO_2 in geological formations [*Pruess*, 2003; *Orr*, 2004b]. At least three options exist for geological storage of CO_2 [*Orr*, 2004b]:

- (Depleted) oil and gas reservoirs
- Deep saline aquifers
- Unmineable coal seams

In Table 1.1 and Figure 1.1 the storage capacities for each of these options are shown, and are based on the work of *Parson and Keith* [1998], and *Orr* [2004]. It must be said that the estimates, presented in literature show strong deviations [*CATO*; *Capture and Storage*; *Anderson et al.*, 2005].

Storage option	*Capacity (Gt CO_2)*	*Impact*
(depleted) Oil and gas reservoirs	920	45% of world emissions until 2050
(deep) Saline aquifers	up to 10.000	20 to 500% of world emissions until 2050
Unmineable coal beds	40 to 150	$<$ 2% of world emissions until 2050

Table 1.1 Geological storage capacities for CO_2

The total storage capacity of underground reservoirs compared to today's emission rates is equivalent of hundreds of years of storage capacity [*IEAGREEN*], especially for deep saline aquifers. Thereby, the attractiveness of subsurface storage is found in the wide spread of different geological formations all over the world and the current knowledge about the deep subsurface. The current storage costs of CO_2 are estimated at $ 20/tonne or less [*Orr*, 2004b]. The worldwide availability of CO_2 and resolving of scientific research questions strongly influences the economics of CO_2 sequestration.

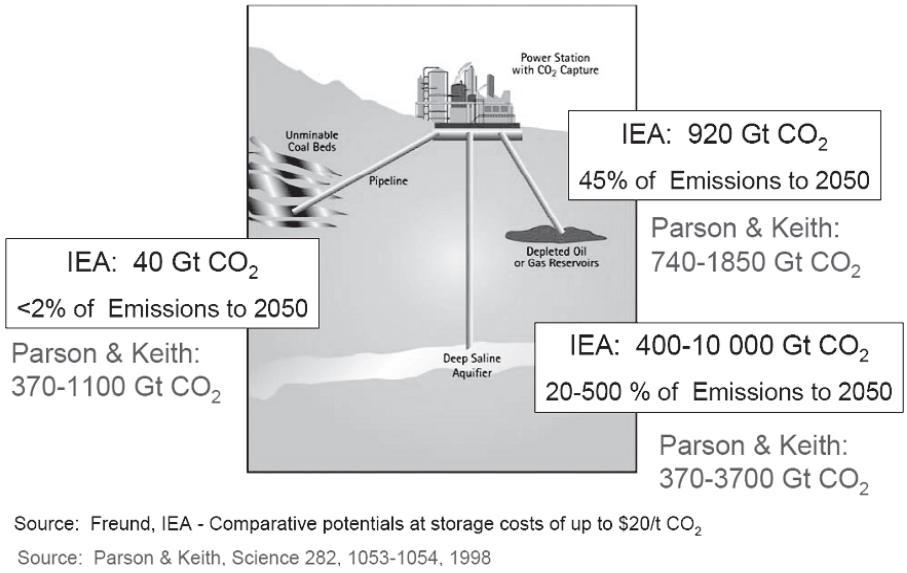

Figure 1.1 Underground CO_2 sequestration applications and their capacities [*Orr*, 2004].

The technologies for CO_2 injection are well established, based on the experience in enhanced oil (EOR) and gas (EGR) recovery [*Orr*, 2004]. In general, the primary objective of carbon dioxide sequestration in depleted oil and gas reservoirs is to enhance the oil production [*Scott et al.*, 2004; *Izgec et al.*, 2005] and the gas and condensate recovery [*Sobers et al.*, 2004]. When the reservoir pressure is close to or above the minimum miscibility pressure (MMP), CO_2 can displace oil efficiently in the invaded zones of the reservoir. Here the composition of the oil and the pressure and temperature conditions play a role [*Orr*, 2004b]. The accompanying storage of CO_2 occurs by dissolution in the formation water and in the undisplaced oil. The use of gas reservoirs for CO_2 sequestration has been proposed but not attempted. CO_2 could be used for pressure maintenance or for condensate vaporization [*Orr*, 2004b]. Utilization of gas and oil reservoirs has the advantage that these specific reservoirs are well characterized and the injection sites are located in the vicinity of CO_2 emission sources such as power plants or the reservoir itself (e.g., the Sleipner project see *Baklid et al.* [1996] and *Sengul* [2006]). Figure 1.2 shows an overview of ongoing and planned sequestration projects all over the world.

The option of sequestration in deep saline aquifers has less economical advantages. However, the storage capacities are much larger and saline aquifers are more common worldwide. The general mechanisms to store CO_2 in aquifers are: storage of CO_2 as free-phase gas in the pore spaces (hydrodynamic and capillary trapping and displacement of in-situ fluids), dissolved CO_2 in the formation water and mineral trapping through geochemical reactions [*Kumar et al.*, 2005; *Doughty and Pruess*, 2004; *Izgec et al.*, 2005; *Mo*, 2005; *Orr*, 2004b]. Opposed to sequestration in oil reservoirs, the flow will not be dominated by well-induced pressure gradients. In aquifers, gravity induced mitigation is dominant and this requires different approaches and strategies.

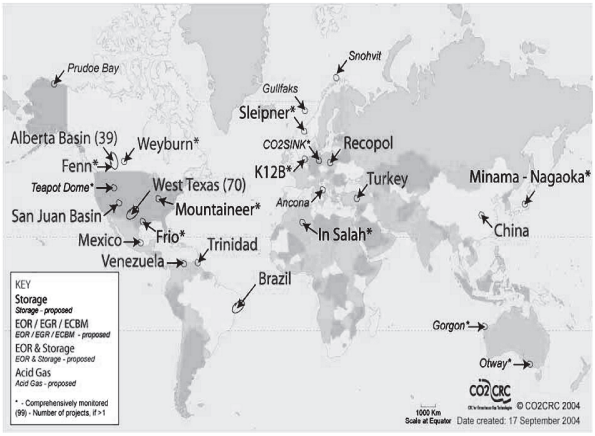

Figure 1.2 Overview of existing and planned CO_2 sequestration projects [*Orr*, 2004]

Coal seams have the opportunity to sequester large volumes of CO_2 for several reasons, i.e. sorbing large volumes of CO_2 into the coal and enhancement of methane production (Enhanced Coal Bed Methane, ECBM) [*Reeves*, 2001]. The mechanism by which CO_2 can enhance the coal bed methane recovery process, and CO_2 is sequestered, is a complex mix of physical and chemical interactions that must achieve equilibrium simultaneously in the sorbed state and the gaseous state [*Reeves*, 2001]. From numerical, experimental and field scale investigations, one can conclude that physical mechanisms and flows are complex. Indeed this offers challenges as well as opportunities. *Orr* [2004b] concluded that of the three options presented, the sequestration of CO_2 in coal beds is the least well understood. However, together with storage in oil and gas reservoirs, this technique is

considered the most economical and has the smallest environmental impact [*Smith et al.*, 2003].

1.3 Reservoir mechanisms during CO_2 sequestration

Within the framework of this thesis, in this paragraph a more detailed overview is given of the reservoir mechanisms, which are considered important for the application of CO_2 storage in aquifers and coal seams.

At depths below 800 to 1000 m, CO_2 is in its supercritical stage (P>73.8 bar and T>31°C) and has a liquid-like density that provides the potential for efficient utilization of geological storage. The properties of the injected CO_2 require sufficient characterization of the geological formation for different reasons. The density difference between the in-situ fluids and the CO_2 results in buoyancy forces. This drives the injected CO_2 upward in the formation until a geological seal is reached [*Kumar et al.*, 2005]. This transport behavior strongly depends on the phase behavior of CO_2. The density and viscosity of CO_2 depends on the temperature and pressure conditions. Variation of these reservoir properties can change CO_2 continuously from super-critical to sub-critical phases, i.e. gaseous or liquid CO_2, without phase boundaries [*Pruess*, 2003]. These phenomena lead to complex behavior of the water-CO_2 mixture [*Spycher et al.*, 2003] and proper understanding is required to assess the sequestration.

Another issue in sequestration applications is the permanence and long-time storage behavior. Here the integrity of the seal or so-called caprock is important [*Jimenez and Chalatu*, 2002; *Kumar et al.*, 2005]. Crucial elements in CO_2 sequestration in aquifers are the permanent storage for the time frame of interest, from a several hundreds to several thousands of years [*Chiquet et al.*, 2005], the prediction and monitoring of CO_2 mitigation behavior and storage volumes [*Sengul*, 2006]. Potential leakage behavior must be considered and taken seriously.

The challenges in reservoir knowledge are found in the heterogeneous system. The heterogeneity or permeability structure directly influences the so-called sweep efficiency of the injected CO_2 and affects the mitigation. High permeability streaks and fractures are making preferential flow a significant effect, especially when coupled with the strong buoyancy forces [*Doughty and Pruess*, 2004]. Moreover, the ratio between the vertical and horizontal permeability influences the percentage of trapped gas [*Mo et al.*, 2005]. Mineral trapping of CO_2 results in changing porosity

and permeability. *Pruess et al.* [2003b] concluded that the porosity decreases because of added CO_2 mass to the solid matrix and lower densities of altered mineral products. A small decrease in porosity can result in significant decrease in permeability. This decrease could reduce the CO_2 injectivity.
Sequestration in coal beds shows analogous behavior, however, the system is more complex. Due to the coal rank, lithology and maceral effects, coals demonstrate different pore structures, sorption capacity and gas transport behavior [*Wei et al.*, 2005]. It is generally accepted that the coal structure consists of the macro cleat and fracture system (>50 nm) and the coal matrix (<50 nm). The macro fracture system is initially filled with water and provides the conduits where the mass flow is dominated by Darcy's law. The coal matrix can be subdivided in meso cleats (from 2 to 50 nm), micro cleats (from 0.8 to 2 nm) and the micro pores (< 0.8 nm). The matrix system is relatively impermeable and the mass transfer is dominated by diffusion. After a dewatering stage, CO_2 is injected and flows through the larger cleats of the coal. Subsequently CO_2 is transported through the smaller cleats and is sorbed in the matrix blocks [*Siemons et al.*, 2006]. Generally, the gas sorption rate is controlled by diffusion. Because methane is replaced by CO_2 in a ratio of 1:2, a multi-component gas mixture exists with difficult sorption and (counter) diffusion characteristics. Non-linear behavior for both properties is encountered because of matrix swelling and shrinkage. The change of the matrix also results in changes in stress and strain. Moreover, water effects are exhibited on the gas transport in the coal matrix because of the cleat system and dual porosity system.

1.4 Capillary pressure and wettability in CO_2 sequestration applications

It can be concluded that a variety of reservoir properties determines the efficiency, capacity, safety and success of the storage process. Summarized; heterogeneity of the formation, gas trapping, phase behavior, adsorption capacity of the rock (or coal) and the sealing integrity are considered as the most important reservoir parameters. Two important properties, which have not been given sufficient interest, are capillary pressure and wetting behavior of the geological formation. Unfortunately, there are no reported capillary pressure data for rock-CO_2-water and the coal -CO_2-water systems at elevated pressures, let alone at supercritical conditions.

By convention, capillary pressure is defined as the pressure difference between the non-aqueous and the aqueous phase and can be seen as a function of the water saturation. The wettability of the reservoir rock is defined by the tendency of one fluid to spread on or adhere to a solid surface in the presence of other immiscible fluids and can be obtained by capillary pressure measurements [*Anderson*, 1986] (see also Appendix A). Depending on the heterogeneous structure, capillary effects can have a positive or negative effect on the sequestration efficiency. In all heterogeneous media, fluid displacement will be characterized by a sequence of drainage (decreasing water saturation) and imbibition (increasing water saturation) events [*van Duijn and de Neef*, 1995]. Therefore, capillary hysteresis is an important aspect of CO_2 storage, especially when CO_2 is stored in an immobile form, which is the most significant mechanism [*Kumar et al.* 2005]. Thereby the wettability behavior of heterogeneous media influences the fluid displacement characteristics [*van Lingen et al.*, 1996].

Moreover, the sealing capacity of the caprock depends on the capillary behavior. Here, the capillary sealing potential (threshold pressure) of the caprock is the critical parameter and plays an important role on the storage safety [*Chiquet et al.*, 2005; *Jimenez and Chalaturnyk*, 2002]. The threshold pressure can be negatively influenced by the change in wettability. Examples of wetting alteration by CO_2 of shaly caprocks have been reported by *Chiquet et al.* [2005].

The efficiency of CO_2 sequestration in coal seams (ECBM) strongly depends on the coal type, the pressure and temperature conditions of the reservoir *[Siemons et al.*, 2006] and the interfacial interactions of the coal-gas-water system [*Keller,* 1987]. In coal layers the efficiency, storage capacity and diffusion rates of CO_2 are related to the wetting behavior of the coal-CO_2-water system. *Siemons et al.* [2006, 2006b] described the pressure dependency of the contact angle for the CO_2-water-coal system. They concluded that wetting alteration from water-wet to CO_2-wet, for high rank coal already occurred at pressures above 2.7 bar. For medium rank coal, the alteration was observed for pressures in the range of 80 to 85 bar.

Because wetting behavior can be determined by capillary pressure characteristics, proper understanding of the capillary pressure behavior is required for CO_2 sequestration applications. Thereby, capillary pressure is essential for safety analysis, especially when the long-term behavior must be predicted for the containment of the injected CO_2 in assessing the suitability and potential of CO_2 sequestration for different applications.

1.5 Capillary pressure in porous media

Capillary pressure (P_c) is well described throughout the years and numerous measurements are conducted and theories are proposed to understand capillary pressure behavior in porous media. In Appendix A, the basic principles of capillary pressure are discussed. By convention, the capillary pressure is defined as the pressure difference between the non-aqueous and the aqueous phase. It is known that the capillary pressure depends on the water saturation (S_w), the saturation history (hysteresis) and a rate component [*Hassanizadeh et al.*, 2002]. Therefore, static drainage (imbibition) capillary pressures can be considered when $\partial S_w / \partial t \to 0$.

It has been asserted that transient effects of capillary pressures can be observed while redistribution of phases takes place [*Morrow*, 1970]. The hysteresis in capillary pressure behavior is found by comparison of the drainage to imbibition curves. *Leverett* [1941] proposed to use the static capillary pressure also during transient conditions. This approach is successfully used in reservoir engineering applications. However, it can be shown that dynamic capillary pressure is important in applications for (enhanced) oil recovery, e.g. Water-Alternating-Gas, geological CO_2 sequestration and spreading of non-aqueous phase contamination in the saturated and unsaturated zone. Therefore, dynamic capillary pressure is the subject for many theoretical [*Morrow*, 1970; *Hassanizadeh and Grey*; 1993, *Hassanizadeh et al.*, 2002; *Pavone*, 1990; *Kalaydjian*, 1992] and experimental studies [*Labastie et al.*, 1980; *Kalaydjian*, 1992; *Honarpour*, 1996; *Topp et al.*, 1967; *Wanna-Etyem*, 1982; *O'Caroll et al.*, 2005; *Wildenschild et al.* 2001; *Hammervold et al.*, 1998]. Considerations based on non-equilibrium thermodynamics show that the dynamic capillary pressure is related to the static capillary pressures, P_c^{eq}, as follows

$$P_c = P_c^{eq} - \tau\left(\psi, S_w\right)\frac{\partial S_w}{\partial t} + \Delta P_d\left(\Delta S_w\right)U\left(-\frac{\partial S_w}{\partial t}\right) - \Delta P_{im}\left(\Delta S_w\right)U\left(\frac{\partial S_w}{\partial t}\right) \quad (1.1)$$

where τ is a material (damping) coefficient that depends on the properties of the fluids and the porous media, $U\left(x\right)$ is the unit step function, $\psi = \pm 1$ denotes imbibition and drainage respectively. In this formulation P_c^{eq} is the surface free-energy change that occurs when a unit of non-wetting fluid phase is injected.

Moreover, *Morrow* [1970] in his classical paper suggests that ΔP_d (ΔP_{im}) describes the contribution due to Haines jumps during the drainage and imbibition process. Haines jumps occur at pore scale level and are irreversible internal fluid redistributions that decrease the surface energy. For the case of hysteresis between drainage and imbibition, *Hassanizadeh and Gray* [1993] found that capillary pressure is a function of the specific area of the fluid-fluid interface per unit volume, as well as of saturation. They attribute the difference between imbibition and drainage capillary pressure to the increase of the non-wetting/wetting interface during the entire drainage/imbibition cycle. *Reeves and Celia* [1996] performed theoretical studies, which supports this idea. Experiments with a micro-pore model are conducted by *Cheng et al.* [2004]. They found different fluid-fluid areas for similar saturations and ascribe the phenomena for hysteresis to the creation and destruction of interfaces.

The material coefficient τ [kg m $^{-1}$s $^{-1}$] starts to play a role when $\partial S_w / \partial t \neq 0$ and transient conditions are considered. This coefficient may not be constant in a specific system and may be a function of saturation [*Hassanizadeh et al.*, 2002] or inversely proportional to the total flow rate [*Kalaydjian*, 1992]. From existing studies, *Hassanizadeh et al.* [2002] estimated the average τ_{av} based on Eq. 1.1, with $U\left(x\right) = 0$. They found τ_{av} to be in the range between $3 \times 10^4 - 5 \times 10^7$ [kg m-1 s-1] and dynamic effects were absent in or less significant in fine-textured soils for drainage conditions. However, clear physical processes cannot be attributed to describe dynamic capillary pressure well.

Experimental investigation of the dynamic behavior of P_c is performed in different ways. Traditional static capillary pressure experiments, as found in literature, are based on the multi-step method or a continuous phase injection (transient conditions). This thesis partly focuses on measuring capillary pressure for the quasi-static conditions where specific injection rates are applied. In the work of *Hassanizadeh et al.* [2002], an overview of experimental work that is done over the last 50 years is presented. They conclude that most of the experimental work that deals with dynamic capillary pressure is related to unsaturated flow. *Topp et al.* [1967] determined drainage data between water and gas in the unsaturated zone on a coarse sandy soil by static, steady state and transient conditions. The static conditions indicate no fluid movement at all, in contrast to the steady state

situation where no movement of the liquid-gas interfaces, but only flow of the liquid through the liquid-filled pores is assumed. Dynamic conditions are created with constant gas injection. They observed no significant flow rate dependency during unsteady-state drainage processes (drainage time of 330 minutes, 237 minutes and 110 minutes). Furthermore, no clear transient (dynamic) effect is found by comparison of the capillary pressure curves for static and steady state conditions. When transient conditions are resumed after the phase distribution was equilibrated, capillary pressures were found to be in between the static and transient curves whereas resuming static conditions after transient conditions seems not to restore the capillary pressure towards the static curve [*Friedman et al.*, 1999]. Moreover, static and dynamic imbibition and drainage experiments in four different soil types are reported by *Wanna-Etyem* [1982]. He observed a difference between the static and transient main imbibition curves; however, an increasing injection rate during transient measurements did not show a significant effect for the imbibition process.

Furthermore, *Kalaydjian* [1992] conducted imbibition experiments on limestone (163 mDarcy) and sandstone (174 mDarcy) and he demonstrates very pronounced dynamic effects for different injection rates (1, 5 and 15 ml/h) for the water-oil system. *Labastie et al.* [1980] conclude that for a water-wet medium (92 mDarcy) the imbibition capillary pressure is insensitive to the flow rate. For mixed-wet media the imbibition capillary pressure is negative and becomes more negative as the flow rate increases. *Kokkedee* [1994] developed an experimental set up that measures drainage capillary pressure of Berea sandstone applying a continuous oil injection rate of 10 PV/d decreasing towards 0.01 PV/d near residual water saturation. He interpreted the experiments in order to obtain both the static capillary pressure data and relative permeability curves and reports on flow rate dependency for the low water saturation range. As observed by *Labastie et al.* [1980] there exists a hysteresis in flow rate dependency between drainage and imbibition processes.

To approach the static conditions, *Wildenschild et al.* [2001] carried out quasi-static experiments for the gas-water system applying a small injection rate of 0.5 ml/h ($= 0.17$ PV/d). These results are comparable with the multi-step data. In the work of *Hammervold et al.* [1998] a quasi-steady-state situation was created for both imbibition and drainage by a continuous change in capillary pressure, applying small injection rates (0.05 PV/d).

1.6 Electric permittivity, capillary pressure and interfacial area

The electrical permittivity is related to hydraulic properties of porous media, such as, saturation, porosity, wettability, saturating fluid properties, etc. Therefore, it is proposed to investigate the relationship between the electric permittivity and capillary pressure. Both have in common that they depend on the water saturation and on interfacial characteristics. In the previous section, it is mentioned that the interfacial area can be used together with the water saturation, to uniquely describe the capillary pressure and its hysteresis. Different authors [*Knight*, 1991; *Knight and Abad*, 1995; *Chelidze and Gueguen* 1999; *Chelidze et al.*, 1999] reported on the interfacial contribution to electric permittivity, ε'_s. In order to be able to do accurate simultaneous measurements of permittivity, saturation and capillary pressure, a new measuring procedure was already developed by *Nguyen* [2001]. Moreover, the work of *Gorriti* [2005] forms also the basis to describe the relation and interpretation of electric permittivity as function of water saturation.

To understand the non-uniqueness in capillary pressure (hysteresis), where the drainage and imbibition capillary pressure do not follow a single unique trajectory, we proposed in this work that the electric permittivity will improve the physical and fundamental understanding of capillary pressure. The electric permittivity is a quantity that is related to the ability of the mixture to transmit or permit an electric field. It is widely accepted that a porous medium can be seen as a dielectric medium and thus highly resistant to electric currents. The static part of the permittivity is also known as the dielectric constant, and is usually measured relative to vacuum. Furthermore, the (di)electric permittivity is a function of frequency, and depends on the volume ratio of the different constituents.

Lots of experimental and theoretical work is done to understand the permittivity behavior of multi-component systems. The key questions for the experimental studies were: the validity and the applicability of the experimental tools, the design and the interpretation of the measurements and the influence of the water saturation on the permittivity behavior. Theoretical considerations, are dealing with the effective medium theory (up-scaling) and the mixture's behavior as a function of frequency, presence of water and the distribution of the phases.

1.7 Objectives of this research

The objectives of this thesis are:

- The development of an experimental apparatus that can measure drainage and imbibition capillary pressure in the range of 1 to 100 bar and constant elevated temperatures.
- Fast and accurate capillary measurements applying a constant injection, such that viscous forces can be neglected and static capillary pressure curves can be obtained.
- The investigation of the capillary pressure behavior of the CO_2-water-sand system for gaseous, liquid and super-critical CO_2 (sequestration applications).
- The development of a numerical simulator that assist in the interpretation of the experimental results.
- Investigation of the capillary pressure behavior of the CO_2-water-coal system to evaluate the wetting properties during ECBM.
- The development of an experimental tool that can simultaneously measure the electric permittivity as a function of the frequency and the capillary pressure as a function of the water saturation.
- The investigation of the uniqueness of capillary pressure as a function of water saturation and electric permittivity.

1.8 Thesis Layout

The thesis is based on 4 articles, respectively included in chapter 2-5. Chapter 2 deals with the capillary pressure behavior of the gas (CO_2/N_2)-distilled water-sand system. The comparison between CO_2 and N_2 experiments can be used to observe dissolution effects. The capillary pressures decrease with increasing CO_2 pressures corresponding to the pressure dependence of the interfacial tension. Dissolution rate effects are only observed at low pressures, whereas at higher pressures instantaneous equilibrium can be assumed. These observations are evaluated with a numerical model (discussed in Appendix B). In chapter 3, the capillary pressure and the derived wetting behavior in coal is discussed. To facilitate the interpretation of the coal experiments the results are compared to the results discussed in chapter 2. During primary drainage, the coal behaves water-wet, whereas during imbibition CO_2-wet behavior is observed. If CO_2 injection is

stopped, the capillary pressure decreases significantly. Vice versa, the imbibition capillary pressure increases when water injection is stopped. Similar effects are absent or much smaller in the CO_2-water-sand experiments. A numerical model shows that viscous force induced rate effects are negligible. The rate behavior can be explained by water film and gas film rupture effects, as is extensively discussed in the papers by *Hirasaki et al.* [1991]. It can be concluded that the wetting behavior of coal is most conveniently obtained from the imbibition behavior. In chapters 4 and 5, the combined non-destructive measurement of capillary pressure and electric permittivity is described. Chapter 4 deals with calibration, precision and validity of the newly developed impedance tool. The background and theory of permittivity measurements and the data analysis are discussed in more detail in Appendix C. In chapter 5, the data of the capillary pressure as a unique function of the electric permittivity (low frequency, 100 kHz) and the water saturation is presented. The results for this frequency show a typical behavior that is also observed in measurements and computations of interfacial area.

Bibliography

Anderson, W.G. (1986), Wettability Literature Survey- Part 1: Rock/oil/brine interactions and the effects of core handling on wettability, *JPT*, 1125-1144, SPE 13932.

Anderson, J. et al. (2005), Underground geological storage, IPCC report, Ch. 5.

Baklid, A., R. Korbol, and G. Owren (1996), Sleipner vest CO_2 disposal, CO_2 injection into a shallow underground aquifer, SPE paper no. 36600, presented at the SPE Annual Technical Conference and Exhibition, 6-9 October, Denver, Colorado, SPE 36600.

Brusseau, M.L., N.T. Nelson, and M. S. Costanza-Robinson (2003), Partitioning tracer tests for characterizing immiscible-fluid saturations and interfacial areas in the vadose zone, *Vadose Zone Journal*, *2*, 138–147.

Chelidze, T. L., and Y. Gueguen (1999), Electrical spectroscopy of porous rocks: a review –I. Theoretical model, *Geophys. J. Int.*, *137*, 1-15.

Chelidze, T. L., Y. Gueguen, and C. Ruffet (1999), Electrical spectroscopy of porous rocks: a review –II. Experimental results and interpretation, *Geophys. J. Int.*, *137*, 16-34.

Cheng, J.T., L.J. Pyrak-Nolte, D.D. Nolte, and N.J. Giordano (2004), Linking pressure and saturation through interfacial areas in porous media, *Geoph. Res. Lett.*, 31, L08502, doi:10.1029/2003GL019282.

Chiquet, P., D. Broseta, and S. Thibeau (2005), Capillary alteration of shaly caprocks by carbon dioxide, SPE paper no. 94183, presented at the SPE Europec/EAGE Annual Conference, 13-16 June, Madrid, Spain, SPE 94183.

Dalla, E., M. Hilpert, and C.T. Miller (2002), Computation of the interfacial area for two-fluid porous medium systems, *Journal of Contaminant Hydrology*, *56*, 25–48.

Doughty, C., and K. Pruess (2004), Modeling supercritical carbon dioxide injection in heterogeneous porous media, *Vadose Zone Journal*, *3*, 837-847.

Fraily, S. M., J. P. Grube, and R .J. Finley (2004), Investigation of liquid CO_2 sequestration and EOR in low temperature oil reservoirs in the Illinois basin SPE paper no. 89342, presented at the SPE/DOE Symposium on Improved Oil Recovery, 17-21 April, Tulsa, Oklahoma.

Friedman, S. P. (1999), Dynamic contact angle explanation of flow rate-dependent saturation–pressure relationships during transient liquid flow in unsaturated porous media, *J. Adhesion Sci. Technol*, *13 (12)*, 1495–1518.

Gorriti, A..G. (2004), Electrodynamic response of soils", Delft University of Technology.The Netherlands, Dissertation.

Hammervold, W.L., and O. Knutsen (1998), Capillary pressure scanning curves by micropore membrane technique, *Journal of Petroleum Science and Engineering*, *20*, 253–258

Hassanizadeh, S.M., W.G. Gray (1993), Thermodynamic basis of capillary pressure in porous media, *Water Resources Research*, *29 (10)* 3389-3405,

Hassanizadeh, S. M., M. A. Celia, H. K. Dahle (2002), Dynamic effect in the capillary pressure-saturation relationship and its impacts on unsaturated flow, *Vadose Zone Journal*, *1*, 38-57.

Held, R.J., and M.A. Celia (2001), Pore-scale modeling extension of constitutive relationships in the range of residual saturations, *Water Resources Research*, *37 (1)*, 165–170.

Hirasaki, G.J. (1991), Wettability: fundamentals and surface forces, *SPEFE*, 217-226, SPE 17367.

Hoffert, M. I., et al. (2002), Advanced technology paths to global climate stability: energy for a greenhouse planet, *Science, 298 (5595)*, 981-987.

Izgec, O., B. Demiral, H. Bertil, and S. France (2005), CO_2 injection in carbonates, SPE paper no. 93773, presented at the SPE Western Regional Meeting, 30 March - April 01, Irvine, California.

Izgec, O., B. Demiral, H. Bertin, and S. Akin (2005b), Experimental and numerical investigation of carbon sequestration in deep saline aquifers, SPE paper no. 94697, presented at the SPE/EPA/DOE Exploration and Production Environmental Conference, 7-9 March, Galveston, Texas.

Jimenez, J. A., and R .J. Chalaturnyk (2002), Integrity of bounding seals for geological storage of greenhouse gases, SPE paper no. 78196, presented at the SPE/ISRM Rock Mechanics Conference, 20-23 October, Irving, Texas.

Kalaydjian, F. J.-M. (1992), Dynamic capillary pressure curve for water/oil displacement in porous media: Theory vs. experiment, SPE paper no. 24813, presented at the SPE Annual Technical Conference and Exhibition, 4-7 October, Washington, D.C.

Keller, D. V. Jr. (1987), The contact angle of water on coal, *Colloids Surf.*, *22*, 21-35.

Knight, R. (1991), Hysteresis in the electrical resistivity of partially saturated sandstones, *Geophysics*, *56*, 2139-2147.

Knight, R., and A. Abad (1995), Rock /water interaction in dielectric properties: Experiments with hydrophobic sandstones, *Geophysics*, *60*, 431-436.

Kokkedee, J.A. (1994), Simultaneous determination of capillary pressure and relative permeability of a displaced phase, SPE paper no. 28827, presented at the European Petroleum Conference , 25-27 October, London, United Kingdom.

Kumar, A., R. Ozah, M. Noh, G. A. Pope, S. Bryant, K. Sepehrnoori, and L. W. Lake (2005), Reservoir simulation of CO_2 storage in deep saline aquifers, *SPE Journal*, *10 (3)*, 336-348.

Labastie, M., M. Guy, J. P. DelClaud, and R. Iffly (1980), Effects of flow rate and wettability on water-oil relative permeabilities and capillary pressure, SPE paper no. 9236, presented at the SPE Annual Technical Conference and Exhibition, 21-24 September, Dallas, Texas.

Ledley, T. S., E. T. Sundquist, S.E. Schwartz, D.K. Hall, J.D. Fellows, and T. L. Killeen (1999), Climate change and greenhouse gases, *EOS Trans.*, *80 (39)*, 453–458.

Leverett M. C. (1941), Capillary behavior in porous solids, *Trans. AIME*, *142*, 152-168.

Mo, S., I. Akervoll (2005), Modeling long-term CO_2 storage in aquifers with a black-oil reservoir simulator, SPE paper no. 93951, presented at the SPE/EPA/DOE Exploration and Production Environmental Conference, 7-9 March, Galveston, Texas.

Morrow, N. (1970), Physics ad thermodynamics of capillary action in porous media, *Ind. Eng. Chem.*, *62(6),* 32-56.

Nguyen, B.L. (1999), Frequency domain reflectometry for oil saturation measurements, Delft University of Technology. Uitgave: Delft University of Technology, Delft, The Netherlands, 127 p. ISBN: 90-9013-329-1.

O'Caroll, D.M., and T. J. Phelan (2005), Exploring dynamic effects in capillary pressure in multistep outflow experiments, *Water Resources Research*, *41*, 1–14.

Orr Jr., F. M., Geological storage of carbon dioxide, SPE paper no. 101630 presented at the 2004 ATCE, September 27 (keynote presentation).

Orr Jr., F. M. (2004b), Storage of carbon dioxide in geological formations, *JPT*, *56 (9)*, 90-97.

Parson, E. A., D. W. Keith (1998), Fossil fuels without CO_2 emissions, *Science*, *282 (5391)*, 1053-1054.

Pavone, D. (1990), A Darcy's law extension and a new capillary pressure equation for two-phase flow in porous media, SPE paper no. 20474, presented at the SPE Annual Technical Conference and Exhibition, 23-26 September, New Orleans, Louisiana.

Pruess, K. (2003), Numerical simulation of leakage from a geological disposal reservoir for CO_2, with transitions between super- and sub-critical conditions, Proceedings, TOUGH Symposium 2003, Lawrence Berkeley National Laboratory, Berkeley, California, May 12–14.

Pruess, K., T. Xu, J. Apps, and J. Garcia (2003b), Numerical modeling of aquifer disposal of CO_2, *SPE Journal*, *8 (1)*, 49-60.

Reeves, P., and M. A. Celia (1996), A functional relationship between capillary pressure, saturation and interfacial area as revealed by a pore-scale network model, *Water Resources Research*, *32 (8)*, 2345–2358.

Reeves, S. R. (2001), Geological sequestration of CO_2 in deep, unmineable coalbeds: An integrated research and commercial-scale field demonstration project, SPE paper no. 71749, presented at the SPE Annual Technical Conference and Exhibition, 30 September-3 October, New Orleans, Louisiana.

Sengul, M. (2006), CO_2 sequestration - A safe transition technology, SPE paper no. 98617, presented at the SPE International Health, Safety & Environment Conference, 2-4 April, Abu Dhabi, UAE.

Siemons, N., J. Bruining, H. Castelijns, and K. H. Wolf (2006), Pressure dependence of the contact angle in a CO_2–H_2O–coal system, *J. Colloid Sci., 297*, 755-761.

Siemons, N., J. Bruining, K .H. Wolf, and W. -J. Plug (2006), Pressure dependence of the CO_2 contact angle on bituminous coal and semi-anthracite in water, paper no. 0605, International Coalbed Methane Symposium, Tusculoosa, Alabama, May 22-26.

Smith, D. H., G. Bromhal, W. N. Sams, S. Jikich, and T. Ertekin (2003), Simulating carbon dioxide sequestration/ECBM production in coal seams: Effects of permeability anisotropies and the diffusion-time constant *SPEREE*, *8 (2)*, 156-163.

Sober, L.E., S.M. Fraily, and A.S. Lawal (2004), Geological sequestration of carbon dioxide in depleted gas reservoirs, SPE paper no. 89345, presented at the SPE/DOE Symposium on Improved Oil Recovery, 17-21 April, Tulsa, Oklahoma.

Spycher, N., K. Pruess, and J. Ennis-King (2003), CO_2-H_2O mixtures in the geological sequestration of CO_2. I. Assesment and calculation of mutual solubilities from 12 to 1000°C and up to 600 bar, *Geochimica et Cosmochimica Acta, 67 (16)*, 3015–3031.

Topp, G., A. Klute, and D. Peters (1967), Comparison of water content-pressure head data obtained by equilibrium, steady-state, and unsteady-state methods, *Soil. Sci. Soc. Am. Proc.*, *31*, 312–314.

Van Duijn, C.J., M. de Neef (1995), The effect of capillary forces on immiscible two-phase flow in strongly heterogeneous porous media, Report, TU Delft.

Van Lingen, P., J. Bruining, C. van Kruijsdijk (1996), Capillary entrapment caused by small-scale wettability heterogeneities, *SPE Res. Eng.*, *11 (2)*, 93–100.

Wanna-Etyem, C. (1982), Static and dynamic water content–pressure head relations of porous media. Ph.D. diss. Colorado State University, Fort Collins, CO.

Wei, X. R., G. X. Wang, and P. Massarotto (2005), A review on recent advances in the numerical simulation for coalbed methane recovery process, SPE paper no. 93101, SPE Asia Pacific Oil and Gas Conference and Exhibition, 5-7 April, Jakarta, Indonesia.

Wildenschild, D., J. Hopmans, and J. Simunek (2001), Flow rate dependence of soil hydraulic characteristics, *Soil Sci. Soc. Am. J.*, *65*, 35–48.

Wikipedia: http://nl.wikipedia.org/wiki/Kyoto-protocol

CATO: http://www.co2-cato.nl

Capture and Storage: http://www.co2captureandstorage.info

IEAGREEN: http://www.ieagreen.org.uk/ccs.html

Chapter 2 Capillary pressure of the sand-CO_2-water system[1]

2.1 Introduction

There is increasing evidence that the emission of CO_2 contributes to the global warming problem. Geological storage of CO_2 in deep (saline) aquifers, abandoned hydrocarbon reservoirs and unmineable coal seams (Enhanced Coal Bed Methane) has the potential to reduce the problem of global warming. Sequestration of CO_2 in aquifers is achieved by the following processes: (1) storage of CO_2 as free-phase gas in the pore spaces (hydrodynamic and capillary trapping), (2) dissolution of CO_2 in the formation water and (3) mineral trapping through geochemical reactions [*Doughty and Pruess*; 2004, *Kumar et al.*; 2005; *Izgec et al.*, 2005]. According to *Kumar et al.* [2005], the residence time of the CO_2 in aquifers for sequestration applications is of the order of 10.000 years and different times scales for the different processes must be considered. Dissolution of CO_2 in water is rapid and strongly depends on the contact between the phases, whereas the time scale for trapping of CO_2 as free gas is much longer (the life time of the project) and strongly depends on the reservoir properties. Geochemical reactions (e.g., mineral trapping) are in general very slow, however, under some conditions the rate may be comparable to other transport processes [*Kumar et al.*, 2005].

One of the key-issues considered in CO_2 sequestration are the capillary pressure related properties of porous media. *Kumar et al.* [2005] concluded that capillary trapping of CO_2, i.e., as residual gas or as gas trapped below an internal layer, is the most relevant mechanism for underground storage of CO_2. Other mechanisms for which the capillary pressure behavior is important, are the alternate imbibition and drainage processes in heterogeneous media [*van Duijn and de Neef*, 1995], which results in capillary hysteresis. This non-uniqueness in capillary pressure can be explained by irreversible fluid redistributions [*Morrow*, 1970] and the difference between specific areas of the fluid-fluid interface per unit of injected volume [*Hassanizadeh and Gray*, 1993; *Reeves and Celia*, 1996]. For sequestration

[1] This chapter is accepted for publication in Advances in Water Resources on 23-5-2007
doi: 10.1016/j.advwatres.2007.05.010

applications, the hysteresis is of relevance when the fluid displacement leads to residual saturations [*Kumar et al.*, 2005]. Furthermore, capillary pressure is a direct measure for wetting effects [*Anderson*, 1987; *van Lingen et al.*, 1996]. This wetting behavior is relevant for the integrity of the caprock as a geological seal [*Jimenez and Chalaturnyk*, 2002; *Kumar et al.*, 2005]. The seal capacity of the caprock during the project's lifetime is therefore a measure of the sustainability of CO_2 sequestration. From literature, it is found that CO_2 can alter the wettability of the rock [*Chiquet et al.*, 2005; *Plug et al.*, 2006; *Siemons et al.*, 2006a,b]. These wetting alterations are observed for shaly caprocks by determining the contact angle between brine and CO_2 on a mica and quartz surface [*Chiquet et al.*, 2005]. Similar behavior is reported for coal by *Siemons et al.* [2006a,b] and *Plug et al.* [2006]. They concluded, from contact angle measurements and capillary pressure data, that the system becomes CO_2-wet near critical conditions.

Therefore, understanding of the capillary pressure behavior is essential in assessing the suitability and potential of CO_2 sequestration in aquifers. In the literature, there is a lack of experimental data of capillary pressures for the rock-water-CO_2 systems in the relevant temperature and pressure range. The only reference with data on capillary pressures at relevant conditions are the indirect (relative permeability) measurements reported by *Bennion and Bachu* [2006a,b].

For capillary pressure measurements involving CO_2, the complexity of the phase behavior of the CO_2-water system in porous media system requires both sophisticated theoretical and experimental investigations at conditions of practical interest [*Class et al.*, 2002; *Spycher et al.*, 2003; *Ebigbo et al.*, 2006]. The non-linear behavior for the CO_2 density and viscosity, as function of temperature and pressure [*Ebigbo et al.*, 2006] near the critical point, is well described by *Span and Wagner* [1996], *Fenghour et al.* [1999] and *Duan and Sun* [2003]. The solubility of CO_2 in water for various pressures and temperatures is experimentally investigated by *Wiebe and Gaddy* [1940] and a thermodynamic description is given by *Duan and Sun* [2003]. *Chun and Wilkinson* [1995] investigated the interfacial tension for CO_2-H_2O mixtures for a wide range of temperatures and pressures. The results showed a minimum for the interfacial tension at the critical point of CO_2. Numerical and analytical models for the prediction of CO_2 sequestration on the long term can be found in the work of *Pruess and Garcia* [2002], *Class et al.* [2002], *Spycher et al.* [2003], *Nordbotten et al.* [2005] and *Ebigbo et al.* [2006]. For the validation and

applicability of these models, experimental measurements are needed to provide the essential input parameters.

The literature describes a number of techniques, which in principle can be used to measure the capillary pressure at the relevant pressure and temperature conditions. Most techniques are based on the porous plate technique [*Christoffersen and Whitson*, 1995], the micro-pore membrane technique [*Jennings et al.*, 1988; *Longeron et al.*, 1995], mercury drainage experiments [*Anderson*, 1987] and the centrifuge method [*Firoozabadi and Aziz*, 1986; *Newsham et al.*, 2004]. Conventional capillary pressure studies use the multi-step method, where after a finite pressure increment an equilibrium water saturation distribution is established. Experimental data are also available in the literature where continuous phase injection is applied [*Topp et al.*, 1967; *Labastie et al.*, 1980; *Wanna-Etyem*, 1982; *Kalaydjian*, 1992; *Kokkedee*, 1994; *Honarpour et al.*, 1996; *Hammervold et al.*, 1998; *Wildenschild et al.*, 2001; *O'Caroll et al.*, 2005;]. These experimental data can be considered as quasi-static because small displacement rates are applied.

In this study, we performed capillary pressure measurements on the unconsolidated sand-CO_2-distilled water system up to near critical conditions. The reason we choose to investigate the capillary behavior of unconsolidated samples is that the experimental set-up is not suitable for consolidated cores.

The objective of this work is to develop a method with which static drainage and imbibition capillary pressures for CO_2 can be measured continuously as a function of saturation at various temperature (T) and pressure (P) conditions and to investigate the effects of the dissolution of CO_2 in water during the CO_2 sequestration process. Quasi-static conditions are achieved by applying small injection rates (0.01-0.1 PV/h). To understand the influence of the dissolution process for the CO_2 experiments, nitrogen (N_2) experiments are conducted for which the dissolution effects are much smaller.

From the measurements we expect to observe the mass transfer effects of CO_2 on the injection and production curves because the fluid velocities are very small compared to the mass transfer rate. To understand the effects of dissolution on capillary pressure and the cumulative water production, a quasi-1D, fully implicit numerical model is developed. Moreover, the measurement procedure is validated by this model, which simulates the drainage experiments. The simulator is based on the upstream finite volume method that incorporates the CO_2-H_2O phase

behavior, mass transfer and dissolution of one phase into another. The mathematical model is explained in Appendix B.

2.2 Experimental design

2.2.1 Experimental set-up

The equipment is an optimized version of the set-up presented in *Mazumder et al.* [2003] and *Plug et al.* [2007], and is based on the porous plate technique combined with the micro-pore membrane technique, discussed by *Jennings et al.* [1988], *Longeron et al.* [1995] and *Christoffersen and Whitson* [1995]. This set-up is suitable to measure the capillary pressure for water-gas (N_2 and CO_2) system in unconsolidated quartz sand for different fluid pressures (from P_{atm} to 85 bar) and temperatures. An overview of the temperature and pressure properties of each experiment performed, are listed in Table 2.1.
In Figure 2.1, the schematic diagram of the set-up is shown and the cross section of the sample holder is shown in Figure 2.2 and discussed in Section 2.2.2. A photo impression of the experimental set-up is given in Appendix D. Two syringe pumps (ISCO pump, 260D) are connected to the in- and outlet of the sample holder and can be set to a constant injection rate (accuracy ± 0.005 ml/h) or a constant pressure (accuracy ± 0.01 bar). The gas phase is injected or produced at the top of

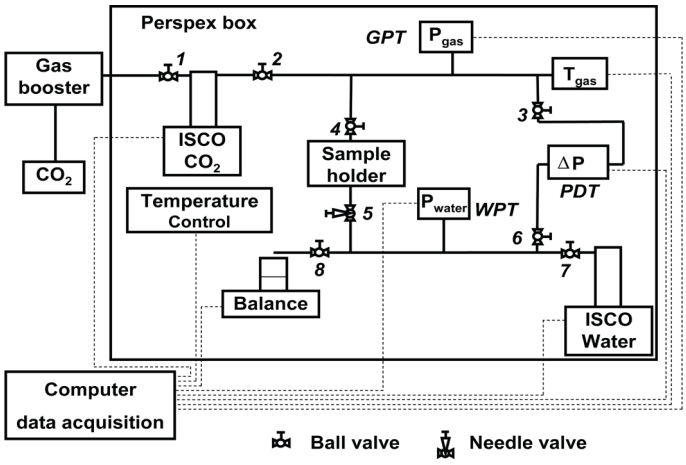

Figure 2.1 Schematic layout of the experimental set-up.

the sample holder and the water is collected or injected at the bottom using the water syringe pump for pressures above 1 bar. For primary drainage experiments at atmospheric conditions, valve 7 is closed and valve 8 is open and the water is produced in a beaker placed on a balance (accuracy ± 0.005 g). A layer of paraffin on top of the water surface avoids evaporation. The gas pressure transducer (GPT) and the water pressure transducer (WPT) record the single-phase pressures (range 0 to 100 bar, accuracy ± 0.01 bar). The differential pressure between the gas and the water phase is measured by the pressure difference transducer (PDT, range $0-500$ mbar, accuracy ± 0.1 mbar), which is located at the same height as the middle of the sample, such that no correction for gravity effects is required.
To maintain a constant temperature we cover the entire set-up with a Perspex box, sealed by polystyrene. Inside the box two 60 W light-bulbs, which switch on and off, regulate the temperature in the range between $25-40\pm 0.5\,^{\circ}$C. We allow temperature equilibration for at least two days for gaseous and liquid CO_2/N_2 and at least three days for supercritical CO_2.

2.2.2 The sample holder

The sample holder, as shown in Figure 2.2, consists of 3 parts: two end-pieces and a ring that contains the unconsolidated sample. In this work, 2 types of rings are used: a stainless steel ring with a height of $H = 25$ mm and a PEEK (Polyetheretherketone) ring with a height of $H = 27$ mm. (see Chapter 4 and 5; *Plug et al., 2007*). The sand pack with a permeability of $k \approx 2\times 10^{-10}$ m^2, is kept in place using a combination of plates at the top and bottom of the sample. At the bottom, two porous plates (*SIPERM R, Cr-Ni-Steel basis*), with a permeability of 2×10^{-12} m^2 and a porosity of 0.32, support the sample and protect the hydrophilic Millipore membrane used in primary drainage experiments. Two stainless steel plates both with 32 perforations ($D_p = 5$ mm) are used at the top directly above the sample in combination with a nylon filter (see appendix D). Between these plates, a hydrophobic membrane is placed for the primary imbibition process, prohibiting water production. To avoid leakage of gas or water over the hydrophobic or hydrophilic membranes, we seal the outer perimeters with a Viton O-ring. Concentric flow grooves in the end-pieces redistribute the injected and produced phase over the total sample area to avoid preferential flow and fast breakthrough of the injected phase (see Appendix D).

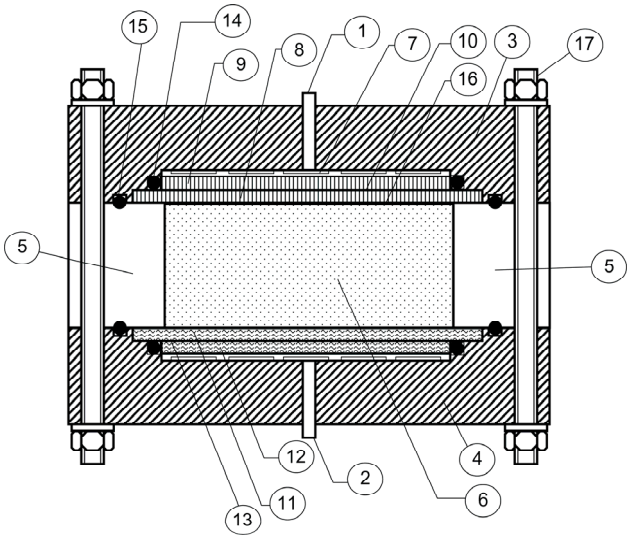

Figure 2.2 Cross section of the sample-holder: 1. gas-inlet; 2. water-inlet; 3. stainless steel end-piece 1; 4. stainless steel end-piece 2; 5. stainless steel ring (height $H = 25$ mm); 6. porous medium (diameter, $D_{sample} = 84$ mm); 7. concentric grooves; 8. perforated plate (diameter, $D_{ss,1} = 90$ mm); 9. perforated plate (diameter, $D_{ss,2} = 84$ mm); 10. hydrophobic filter (diameter, $D_w = 90$ mm , pore size, 0.45 μm); 11. SIPERM filter (diameter, $D_{s,1} = 90$ mm); 12. SIPERM filter (diameter, $D_{s,2} = 84$ mm); 13. water-wet filter (diameter, $D_G = 90$ mm , pore size, 0.1 μm); 14. O-rings (2.1 mm); 15. O-rings (4 mm); 16. nylon filter (pore size 210 μm); 17. stainless steel bolts.

2.2.3 Experimental procedure

At the start of each experiment, the set-up is cleaned and the porous plates are dried. The assembly of the sample holder is from the bottom upward. For each experiment we use new Millipore filters and new O-rings. When end-piece 2, the porous plates, the hydrophilic membrane and the O-rings included, and the ring are mounted together, we pour the unconsolidated sample in the sample holder. The sample is vibrated for 10 minutes to obtain a better packing and similar sample densities, ρ_s (Table 2.1). The last step in assembling the sample holder is to put end-piece 1, the perforated plates, the hydrophobic filter, the nylon filter and O-rings included, on top of the ring and to close the sample holder. The sample holder is placed in between valve 4 and 5 and the entire system is evacuated for 1 hour. During the evacuation, valve 4 is closed.

The next step is to determine the porosity, φ, with helium. Therefore we measure the void volume of the empty sample holder ($V_{void,empty}$, situation 1) and the sample holder containing the sand ($V_{void,sample}$, situation 2). Both volumes and the sample volume are used and φ can be defined as follows:

$$\varphi = 1 - \frac{V_{void,empty} - V_{void,sample}}{\frac{1}{4}\pi\left(D_{sample}\right)^2 H}. \tag{2.1}$$

In Eq. 2.1, $V_{void,empty}$ and $V_{void,sample}$ include the void volume between valve 4 and 5, the gas tubing (between valves 1, 3 and 4) and the gas pump (see Figure 2.1). In both situations, we start with an initial helium equilibrium pressure, $P_{g,1}$, and after moving the piston of the gas pump upwards, we measure the final equilibrium pressure, $P_{g,2}$. From the difference in gas pump volume, ΔV_{pump}, and the two helium pressures we can determine $V_{void,empty}$ and $V_{void,sample}$ from

$$V_{void,empty/sample} = \frac{P_{g,1}\Delta V_{pump}}{Z_2\left(\frac{P_{g,2}}{Z_2} - \frac{P_{g,1}}{Z_1}\right)} - V_{pump,2} - V_{tubing}, \tag{2.2}$$

where Z_1 and Z_2 are the compressibilities of helium, $V_{pump,2}$ is the final gas pump volume and V_{tubing} is the volume of the gas tubing. For both $V_{void,empty}$ and $V_{void,sample}$ this procedure is repeated 5 times and the average volume can be obtained. The average volume of the sample holder filled with sand is denoted as V_{helium} and presented in Table 2.1. For the sand samples we found a porosity in the range of 0.36 to 0.38 (Table 2.1). Subsequently, the total system is again evacuated for 1 hour and filled with water from the water pump by closing valve 4 and opening valve 5 (Figure 2.1). The values for the water volume, V_{water}, are presented in Table 2.1. Comparison between V_{helium} and V_{water} shows small deviations (~1%), which can be explained by systematic measurement errors and the accuracy of the measurement devices. Since we use helium, the system is leak-tested before each experiment.

When an experiment starts with the primary drainage process, the hydrophobic filter is left out. This makes it easier to pressurize the system. Due to the high

pressure, small air bubbles carried along with the distilled water are dissolved. Similar to the primary drainage process, the hydrophilic filter is removed for primary imbibition tests. In this work we consider 3 types of experiments: *A*. Primary drainage experiments at atmospheric pressure (P_{atm}), *B*. primary drainage and *C*. secondary imbibition experiments at pressures above P_{atm} .

(A) The total sample holder is initially filled with water between valve 4 (closed) and valve 5 (see Figure 2.1). Subsequently the water pump is used to apply a pressure of 10 bar to remove all possible air and to obtain 100% water saturation. When the pressure becomes 10 bar, the water pump is stopped and valve 7 is closed. Subsequently, valve 8 is opened and the water pressure decreases towards the atmospheric pressure. The gas tubing and the gas pump are filled and flushed with either N_2 or CO_2. Finally, we set a constant temperature and let the system equilibrate for 48 hours. The primary drainage experiment starts when a constant gas injection rate is applied and valve 4 is opened. Due to operational restrictions of the *ISCO* pumps for pressures below 1 bar, no imbibition tests are conducted for atmospheric conditions.

(B) For high-pressure experiments the sample holder is initially filled with water and the water pump is set to the fluid pressure we apply during the drainage measurement. Valve 4 is closed and the gas tubing and pump are filled with CO_2 (or N_2). A gas booster, connected to valve 1 (Figure 2.1) is used to bring up the gas pressure. We set a constant temperature and let the system equilibrate. Subsequently, when both the water and gas pressure are equal, a constant gas injection rate is applied, the water pump is set to a constant pressure and valve 4 is opened.

(C) After the primary drainage process, the secondary imbibition process starts when the water pump is set to a constant injection rate and the gas pump is set to a constant production pressure.

2.3 Data analysis procedure

The water saturation (S_w) is obtained by the mass of water produced for the atmospheric conditions and by the change in volume of the water pump for high-pressure conditions ($P > 1$ bar). At the end of the experiment, the integral mass balance is checked by weighing all the separate parts of the sample holder, from which an estimation of the final water saturation in the sample can be obtained.

For the high-pressure drainage experiments, the amount of water in the pump is measured to validate whether only negligible amounts of 'free' gas are produced. After the imbibition tests, we apply essentially the same procedure to validate that there is only negligible water production. It turns out that the gas volume in the water pump never exceeds one percent of the volume [*Jennings et al.*, 1988]. The capillary pressure curves are obtained based on the following:

- The decrease (increase) in water saturation can be obtained from the mass/volume produced (injected).
- The initial water (gas) saturation for primary drainage (imbibition) is 1.
- For small injection rates (<1 ml/h), the viscous pressure drop over the sample holder is negligible (~0.04 Pa).
- For the drainage experiments all the water from end-piece 1 and the perforated plates is drained before the gas reaches the sample (Figure 2.2).
- During the drainage process, all the water remains in pore space of the *SIPERM* plates, hydrophilic filter and the void space of end-piece 2 (Figure 2.2).
- The compressibility of water is neglected for all pressure conditions.
- The porosity for all samples used is constant during the drainage and imbibition process.
- The capillary pressure is defined as the difference in the gas and water bulk phase pressures and measured by the PDT device.

As an illustration we discuss the procedure to obtain the capillary pressure curve for a primary drainage experiment conducted with a constant CO_2 injection rate at a system pressure of $P = 85$ bar and $T = 27\,°C$. Figure 2.3 shows the cumulative water production and gas injection data together with P_c as a function of time. The drainage process starts at point A, where the capillary entry pressure is reached. A fast increment in differential pressure, from 0 to 5 mbar is observed and the corresponding cumulative water production and gas injection volume are 12.75 ml and 13.75 ml respectively. The produced water volume is in agreement with the total void volume of endpiece 1.

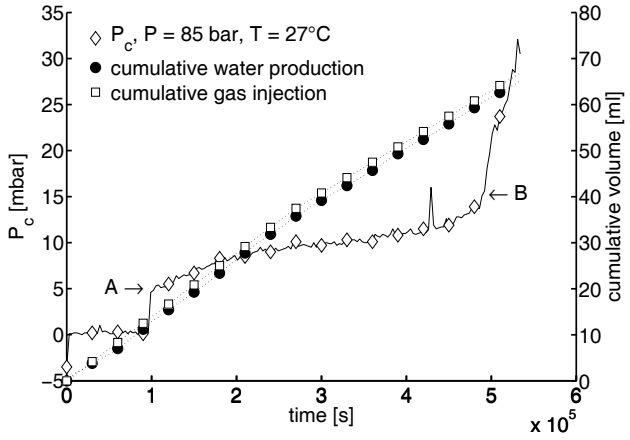

Figure 2.3 The drainage capillary pressure, cumulative water production and gas injection (0.5 ml/h) as function of time for CO_2 injection at 85 bar and 27°C. From these data we obtain the start (A) and end (B) of the primary drainage process. In Figure 2.7 the corresponding capillary pressure curve is shown.

The drainage process ends at point *B*. At this moment, a steep rise in capillary pressure is observed and the liquid CO_2 attains the *SIPERM* filter. The cumulative water production and gas injection at this point is 61.67 ml and 63.03 ml, respectively.

The irregularity in the measured P_c is due to the delay in response of the water pump, which is set to a constant production pressure. The water pump measures the pressure with an accuracy of 10 mbar, and consequently the data consist of a series of spikes, which are not shown in most of the cases, by plotting only local minima. In some exceptional cases, however, the local minima still show these irregularities.

To obtain the $P_c - S_w$ curve, we compute the water saturation from the water production volume using the following expression

$$S_w(t) = 1 - \frac{V_{wp}(t) - V_{wp}(t_s)}{\varphi V_{sample}}, \tag{2.3}$$

where V_{wp} is the water pump volume and φV_{sample} is the pore volume of the sample. The corresponding capillary pressure curve (experiment 12) is shown in Figure 2.7 and the details of this measurement are further discussed in Section 4.2.2.

2.4 Experimental results

In this section the experimental results are presented for the unconsolidated sand-CO_2-water system. Nitrogen (N_2) experiments are performed to facilitate the interpretation of the CO_2 experiments with the strong dissolution effects. We also describe the repeatability of the experimental method and the effects of different sand packs used. To clarify the correlation between the experiments and the numbering, an overview of the sample and system properties applied during the experiments is given in Table 2.1.

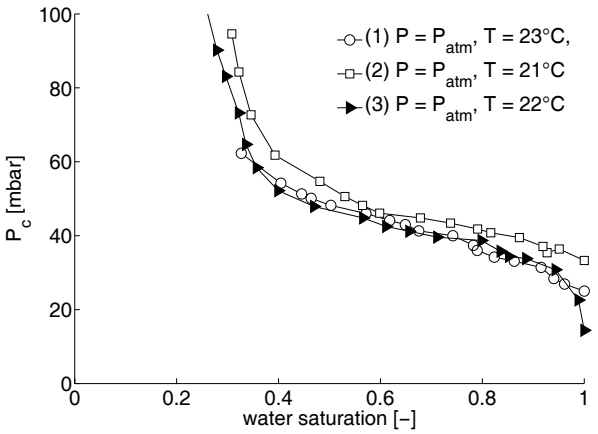

Figure 2.4 Primary drainage capillary pressure curves for CO_2 injection in fine sand ($160 < D_{50} < 210\,\mu m$) for atmospheric conditions. In each case the CO_2 injection rate is 0.5 ml/h. The differences observed are an indication of the repeatability of the experimental method.

Nr.	*gas*	P [bar]	T [°C]	σ^* [N/m^2]	ρ_s [kg/m^3]	V_{helium}^{**} [m]	V_{water} [ml]	φ [-]
1	CO_2	P_{atm}	23	71	no data	no data	no data	0.36
2	CO_2	P_{atm}	21	71	no data	no data	no data	0.34
3	CO_2	P_{atm}	22	71	no data	no data	no data	0.35
4***	N_2	P_{atm}	24	71	1660	93.8	92.0	0.37
5	N_2	P_{atm}	27	71	1658	94.4	95.2	0.37
6	CO_2	P_{atm}	24	71	1661	93.8	94.5	0.36
7	CO_2	P_{atm}	26	71	1661	95.6	96.4	0.38
8	CO_2	8	26	68	1657	93.9	93.6	0.37
9	CO_2	8	28	67	1666	93.7	93.3	0.37
10	CO_2	8	28	67	1666	94.1	93.1	0.37
11	N_2	8	27	71	1656	93.1	93.0	0.37
12***	CO_2	85	27	30	1656	93.5	93.15	0.37
13***	CO_2	85	40	32	1671	91.8	91.3	0.36
*	Data obtained from *Chun and Wilkinson* [1995].							
**	The average helium volume for five measurements.							
***	Experiments conducted with the stainless steel ring ($H = 25$ mm).							

Table 2.1 Correlation between the experiment numbers and the experimental properties and conditions.

2.4.1 Experimental results at atmospheric pressures

To assess the repeatability of the experimental method and of the way we construct the unconsolidated porous medium, we have conducted 3 primary drainage experiments for 3 different sand packs, using fine unconsolidated sand with an average particle size of $160 < D_{50} < 210$ μm. For the intermediate water saturation range ($0.4 < S_w < 0.8$), the capillary pressure curves are repeatable with a deviation in P_c of ± 1.5 mbar. The repeatability slightly decreases near the end point saturations ($P_c \pm 3$ mbar).

The second series of experiments at atmospheric conditions is performed on 4 different coarse sand packs with an average grain size range of $360 < D_{50} < 410$ μm. This coarse sand is also used for high pressures measurements ($P > P_{atm}$). We

apply gas injection rates of $u_{inj} < 0.02$ PV/h, and therefore we can assume that the $P_c - S_w$ curves are obtained under quasi-static conditions (see assumption 3, Section 2.2.4). Two primary drainage curves are measured with N_2 (experiment 4 and 5) and two with CO_2 (experiment 6 and 7). The results for the primary drainage curves are presented in Figure 2.5. The differences in capillary pressures are mainly due to different sand packing and temperature conditions. Indeed, the $P_c - S_w$ curves show the repeatability of the experimental method and the results are within the precision of the experimental method (see Figure 2.4). The peak at $S_w = 0.5$ (experiment 6) is attributed to an experimental artifact. A difference in residual water saturation (S_{wc}) is observed between the CO_2 drainage and N_2 drainage experiments.

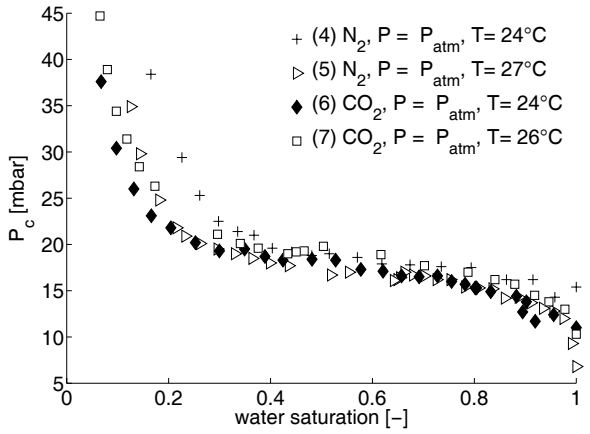

Figure 2.5 Primary drainage $P_c - S_w$ curves for N_2 and CO_2 injection at atmospheric conditions. The capillary pressures for both gases are in the same range due to similar interfacial tensions. For experiment 4, S_w is higher compared to the other experiments. This is a result of the relatively high injection rate, $u_g = 2$ ml/h, applied for the saturation range between 0.18 and 0.27.

Comparing both the N_2 experiments, S_{wc} is 0.16 and 0.11 for experiment 4 and 5, respectively. In the case we use CO_2, the difference in residual water saturation is much smaller, $S_{wc} = 0.06$ and $S_{wc} = 0.08$ for experiment 6 and 7, respectively. Finally, from Figure 2.5 we observe that the drainage curves of the N_2-water system and the CO_2-water system are slightly different, but in the same range.

This can be explained by the small difference in interfacial tension between CO_2 and N_2 (see Table 2.1).

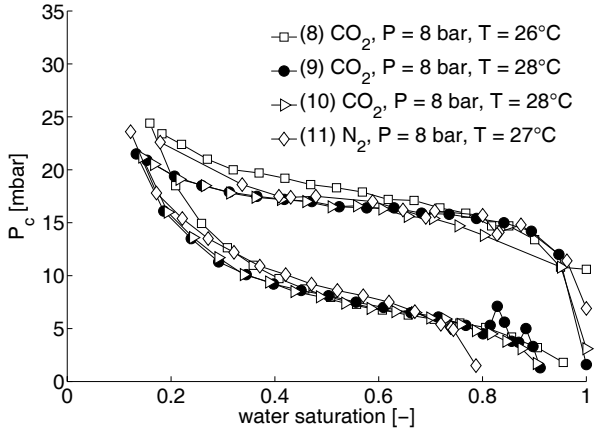

Figure 2.6 $P_c - S_w$ primary drainage (upper curves) and secondary imbibition curves at 8 bar, for experiment 8, 9, 10 and 11 obtained for the coarse sample with CO_2 and N_2 and a flow rate of 0.5 ml/h. The reproducibility of the experiment is excellent.

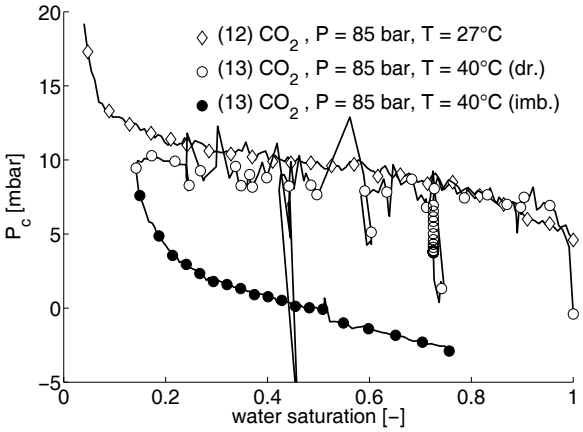

Figure 2.7 Primary drainage capillary pressure curves for liquid (exp. 12) and supercritical CO_2 (exp. 12). The irregularities observed for experiment 13 are due to spontaneous imbibition events and temporarily CO_2-wet behavior. The secondary imbibition curve for supercritical conditions is represented by the closed circles (exp 13). Note that for experiment 13 the capillary pressure becomes negative for $S_w > 0.5$.

2.4.2 Experimental results at high pressures, $P > 1$ bar

The $P_c - S_w$ relationships for the coarse sand sample are investigated at conditions of practical interests. Applying different pressure and temperature conditions we can compare the capillary pressure behavior for different interfacial tensions of CO_2 (Table 2.1), which will result in a pressure dependent capillary pressure. Moreover, the effect of the dissolution of carbon dioxide into the water phase as function of the fluid pressure can be determined by comparing the CO_2 and N_2 capillary pressure curves.

For the 8 bar conditions we performed 3 measurements with CO_2 and one with N_2. The primary drainage and secondary imbibition curves for experiments 8-11 are presented in Figure 2.6. In these four measurements the boundary conditions are such that the gas pressure is set to a constant pressure during the total capillary cycle. Consequently, the water pump is set to a refill rate of 0.5 ml/hr. Except at low water saturations the reproducibility for both the drainage and imbibition processes appears to be excellent, considering the different sand packs [*Plug et al.*, 2007].

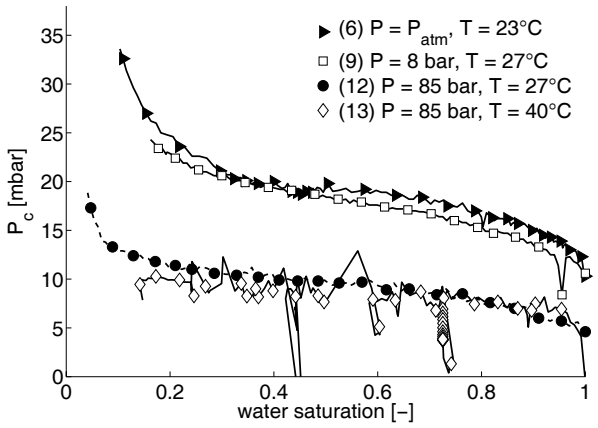

Figure 2.8 Primary drainage capillary pressure curves for CO_2 injection in coarse sand at various pressure and temperature conditions. Varying CO_2 injection rates, ≤ 1 ml/h are applied in experiment 6. The CO_2 injection rate is 0.5 ml/h for experiment 12 and 13. In experiment 9 the water extraction rate is 0.5 ml/h. The differences between the low and high-pressure capillary pressure curves are explained by the decrease in interfacial tension for increasing CO_2 pressures (see also Figure 2.10).

The small irregularities at high water saturations for the secondary imbibition experiment (experiment 9, Figure 2.6) are attributed to summer temperatures in the laboratory, exceeding the upper limit of the temperature control system. For the primary drainage experiment 10 (Figure 2.6) there are no data points between $0.85 < S_w < 0.95$. For both the secondary imbibition experiments 9 and 10, the residual gas saturation is determined at $S_w = 0.92$. Different sand packing combined with the lower temperature (26°C for 8 and 28°C for 9 and 10) result in a small deviation for the saturation range of $0.15 < S_w < 0.5$ and a lower residual gas saturation of $S_{gr} = 0.02$.From Figure 2.6 it is clear that the N_2 injection test shows drainage and imbibition capillary pressures similar to the CO_2 measurements. However, as a consequence of different dissolution properties between N_2 and CO_2 the residual gas saturation with N_2 is higher than for CO_2, where S_{gr} for N_2 is 0.21.

In Figure 2.7 the results are presented for measurements performed at system pressures above 80 bars. Experiment 12 is conducted with liquid CO_2 ($T = 27$ °C) and supercritical conditions are applied for experiment 13 ($T = 40$ °C). It can be seen that the drainage capillary pressure for liquid CO_2 and supercritical CO_2 is of the same range. For the supercritical situation the primary drainage shows significant irregular behavior as a result of sudden imbibition events, whereas for the liquid CO_2 conditions a smooth $P_c - S_w$ curve is measured. The secondary imbibition curve shows negative capillary pressure values for $S_w > 0.5$ (Figure 2.7). To show the pressure dependence of the capillary pressure for drainage, we compare in Figure 2.8 the primary drainage curves for CO_2 pressures of 1, 8 and 85 bar. The secondary imbibition curves for experiment 8, 10 and 13 are compared in Figure 2.9. For both the primary drainage and the secondary imbibition a decrease in capillary pressure is measured for increasing CO_2 pressures. The pressure dependence of the drainage capillary pressure is a result of the interfacial tension [*Chun and Wilkinson*, 1995] (Table 2.1). Hence, the capillary pressure curves can be scaled according to the interfacial tension, as shown in Figure 2.10. Here, P_c / σ is plotted as function of S_w and small deviations between the three pressure conditions are observed. Contrary to the drainage curves, the secondary imbibition curves cannot be properly scaled by the interfacial tension. In Figure 2.11 we show that the values of P_c / σ for supercritical conditions are much smaller than for

gaseous CO_2 ($P = 8$ bar), implying that other mechanisms influence the capillary pressure at high pressures and temperatures. This will be further discussed in Section 2.5.

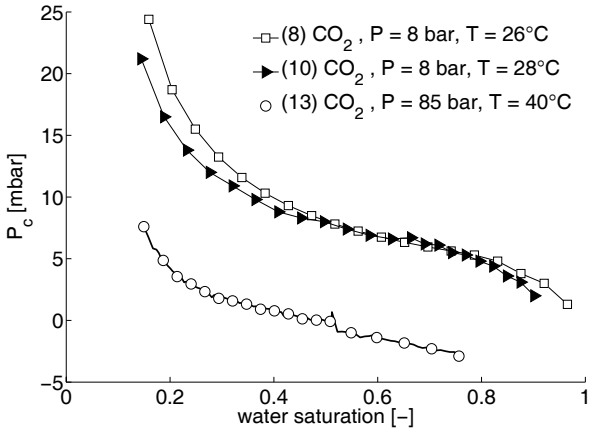

Figure 2.9 Secondary imbibition capillary pressure curves for the CO_2-water system in coarse sand for gaseous CO_2 (experiment 8 and 10) and supercritical CO_2 (experiment 13). The water injection rate is 0.5 ml/h for all experiments. The differences between the low and high-pressure capillary pressure curves are explained by wetting alteration (see also Figure 2.11).

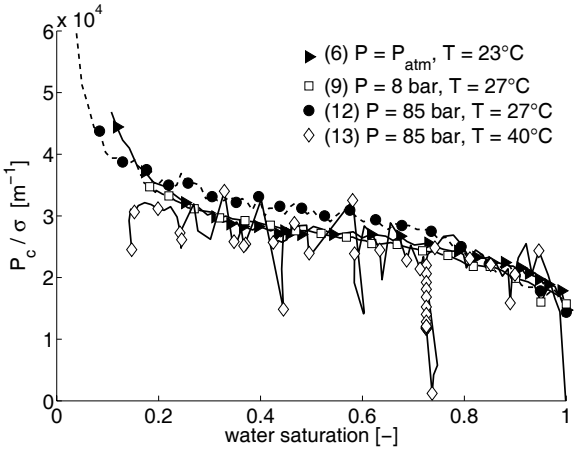

Figure 2.10 Primary drainage capillary pressure scaled by the interfacial tension (P_c / σ) for different CO_2 pressures. The interfacial tensions are obtained by *Chun and Wilkinson* [1995] and are listed in Table 2.1. Small deviations are observed.

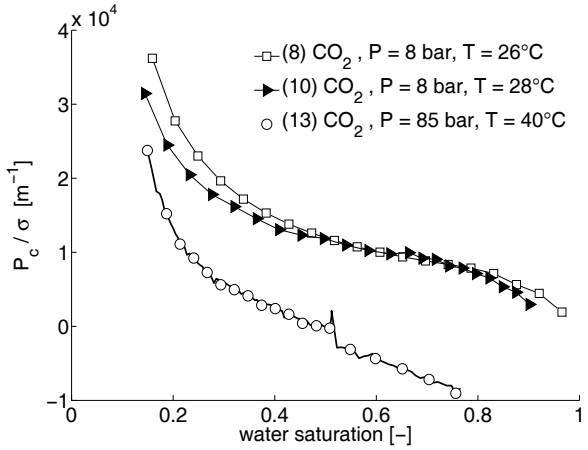

Figure 2.11 Secondary imbibition capillary pressure scaled by the interfacial tension (P_c / σ) for gaseous CO_2 (experiment 8 and 10) and supercritical CO_2 (experiment 13). The significant difference between the gaseous and supercritical curve is a result of wetting alteration due to increasing contact angles (*Chiquet et al.*, 2005) (see also Figure 2.9).

2.4.3 Production and injection behavior during primary drainage

In this section we describe the results obtained for the injection and production behavior of 5 primary drainage experiments. Figures 2.12 and 2.13 show the cumulative water production and gas injection for N_2 at atmospheric pressure (experiment 4) and 8 bar (experiment 11), respectively. For both experiments the N_2 injection rate is 0.5 ml/h. At $t = 3.4 \times 10^5$ s the gas injection rate is changed from 0.5 ml/h to 2 ml/h for experiment 4. During the measurements with N_2, the injected and produced cumulative volumes are similar. A discrepancy between the water production and gas injection volumes for the atmospheric condition is observed near S_{wc}, which can be explained by viscous forces. For the high pressure N_2 case (8 bar), the measured water production shows an irregular behavior, which is attributed to temperature effects. The production and injection curves for primary drainage experiments with CO_2 are presented in Figures 2.14, 2.15 and 2.16. The differences between the injected and produced volumes for the atmospheric case (Figure 2.14) and the 8 bar experiment (Figure 2.15) can be explained by the dissolution effects of CO_2 in water (Section 2.5). When liquid CO_2 is injected (Figure 2.16) these effects are not observed and the cumulative gas volume injected is almost equal to the cumulative water volume produced. The

details of the measured injection and production curves for both N_2 and CO_2 are compared with the numerical results and are further discussed in the next section.

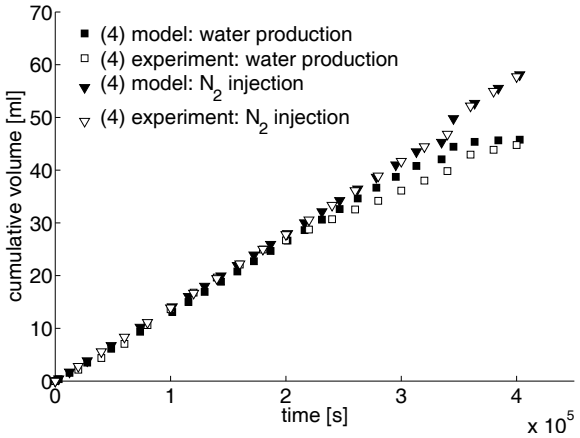

Figure 2.12 Experimental and numerical results for the cumulative water production and N_2 injection volume during primary drainage for experiment 4 ($u_g = 0.5$ ml/h, $P = P_{atm}$, $T = 24$ °C). The experimental results are well predicted by the numerical model. Due to the low solubility of N_2 in water, the production and injection curves coincide for $t < 3 \times 10^5$ s. Viscous forces explain the discrepancy near S_{wc} .

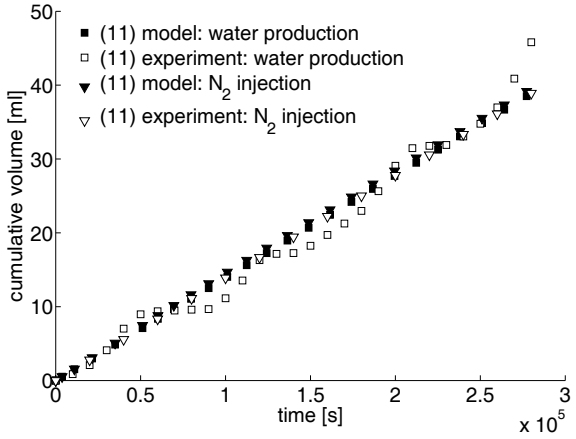

Figure 2.13 Experimental and numerical results for the cumulative water production and N_2 injection volume during primary drainage for experiment 11 ($P = 8$ bar, $T = 27$ °C). Good agreement is found between the experimental and numerical results and the production and injection curves coincide, as a result of the insignificant mass transfer between N_2 and water.

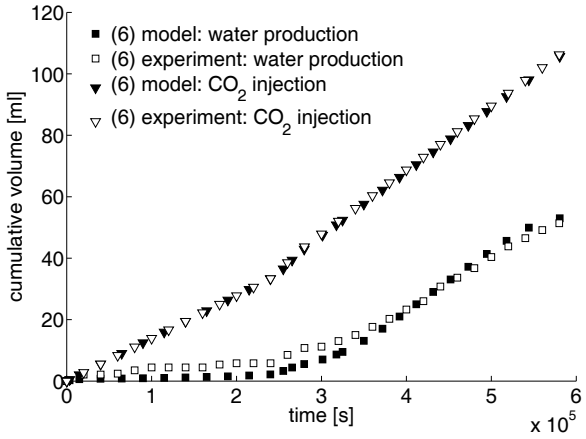

Figure 2.14 The cumulative water production and CO_2 injection volume during primary drainage for experiment 6 at atmospheric conditions and $T = 24$ °C. Good agreement is found between the experimental and numerical results. As a result of the dissolution of CO_2 in water, the production and injection curves deviate significantly and the water production starts to increase after the water is saturated with CO_2 ($t \approx 3$ days).

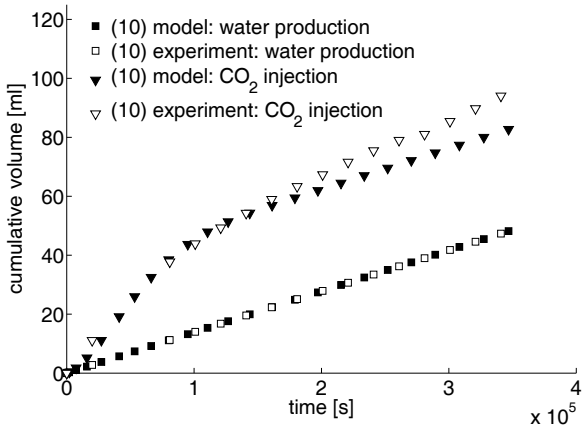

Figure 2.15 The cumulative water production and CO_2 injection volume during primary drainage for experiment 10 at 8 bar and $T = 28$ °C. Good agreement is found between the experimental and numerical results for $t < 1.5 \times 10^5$ s. The CO_2 mass transfer is observed and results in a difference between the production and injection volumes. The discrepancy between the model and experimental results can be explained by CO_2 diffusion in water from the sample to the water production pump.

2.5 Discussion

To get a better understanding of the different processes and mechanisms observed in the experiments, we have developed a one-dimensional, fully implicit flow simulator. The model equations are derived in Appendix B and the model input parameters are presented in Table B.1.

Figure 2.17 plots the experimentally and the numerically obtained $P_c - S_w$ curves for the CO_2-water system at atmospheric conditions (experiment 6). It is clear that the measured capillary pressure curve shows good agreement with the predicted capillary pressure curve, based on the bulk gas and water pressure (see Eq. B.18). This indicates that the experimental method is validated by the numerical model and that the assumptions, listed in Section 2.3 are justified. Small discrepancies between the measured and predicted curves near the end point saturations are a result of the input capillary pressure curve, based on the Leverett-J function (see Eq. B.8, Appendix B). Moreover, the numerical simulations show that the *SIPERM* plates at the bottom have no effect on the measured $P_c - S_w$ curve for the flow conditions applied. Indeed, it can be expected that for viscous dominated displacement, i.e. higher injection rates, the effects of the *SIPERM* plates on P_c are observed [*van Lingen*, 1998].

The small values for S_{wc} measured for low and high pressure primary drainage experiments with CO_2 can be explained by the quasi-static conditions. For the small injection rates, the displacement is capillarily dominated ($Ca \sim 10^{-8}$) and entrapment of water plays a minor role [*Wildenschild et al.*, 2001]. For the drainage process with N_2, experiment 4 in Figure 2.5, we conclude that the exceptional high gas injection rate applied near S_{wc} (2 ml/h) causes more hydraulic isolation of water filled pores [*Wildenschild et al.*, 2001]. Hence the water phase becomes more disconnected and viscous forces start to dominate for higher saturations [*Kokkedee*, 1994]. An increase in S_{wc} compared to the other experiments is than observed. This behavior is also predicted by the model, where near S_{wc} the production of water tends to zero and a fast increment in P_c is computed (e.g., Figure 2.12).

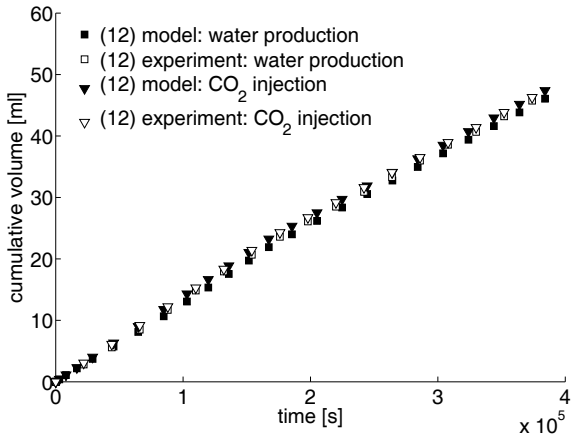

Figure 2.16 Experimental and numerical results for the cumulative water production and liquid CO_2 injection volume ($P = 85$ bar, $T = 27$ °C). Good agreement is found between the experimental and numerical results. Although the CO_2 will dissolve in the water, the production and injection curve coincide because the mass transfer of CO_2 barely influences the CO_2 pressure.

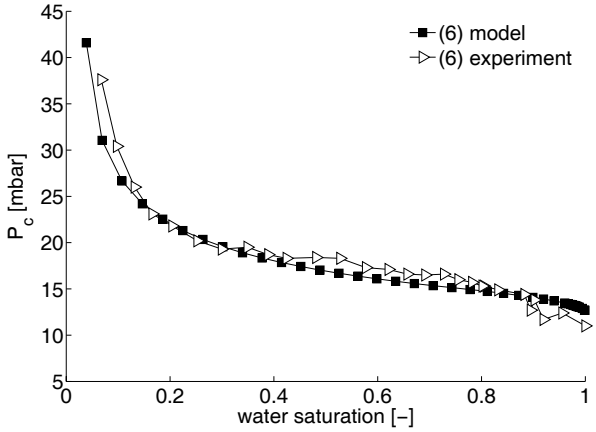

Figure 2.17 Primary drainage capillary pressure curves, measured and predicted for CO_2 injection at atmospheric conditions (experiment 6). The CO_2 injection rate is 0.5 ml/h. The numerical results are computed from Eq. B.18 and good agreement is found with the measured $P_c - S_w$ curve.

Differences in S_{gr} between CO_2 and N_2 imbibition experiments (Figure 2.6) are a result of the dissolution behavior. This effect is observed in experiment 10 where water breakthrough occurs for almost one day and a reasonable amount of water is produced (12.4 ml). After we start the secondary drainage experiment (not shown here), the volumetric water balance is derived, and only 9 ml of water is produced before the increment of P_c is observed (similar to event A in Figure 2.3). Under the assumptions that no water remains in the stainless steel filters and the gas tubing (see Figure 2.2) and $c_{ww} / c_{wW} \approx 1$ (Eq. B.13, Appendix B), the water saturation at the start of the secondary drainage process approximates $S_w = 1$. This indicates that the total amount of residual CO_2, present at the moment of water breakthrough after imbibition, has been dissolved in the water. Therefore, we assume that the water phase is not fully saturated with CO_2 at the end of the imbibition process.

One of the objectives of this work is to provide experimental data for the capillary pressure, measured for the rock-water-CO_2 systems in the relevant temperature and pressure range, e.g. experiment 12 and 13 (Figure 2.7). The only reference with data on capillary pressures with which we can compare our results are the measurements reported by *Bennion and Bachu* [2006b]. They reported on positive drainage capillary pressures for the supercritical CO_2-brine systems, ranging from 0.1 ($S_w = 1$) to 1000 bar ($S_w = S_{wc}$). However, these capillary pressures were obtained from indirect measurements (relative permeability) and for low permeable cores ($2.1 \times 10^{-14}\,m^2$).

The complex behavior of the CO_2-water system is observed during supercritical displacement (experiment 13, Figure 2.7) and is explained by phase instabilities in the vicinity of the critical point. Small system perturbations, like temperature variations and corresponding thermal expansion effects, will cause density and viscosity changes. This results in occasional water imbibition during continuous CO_2 injection (observed as fast drops in P_c). In addition, temporary CO_2-wet conditions are considered. Because the CO_2 trapped in the crevices of the sand will not instantaneously dissolve in the water, the water will 'see' a surface consisting of sand and gas patches.

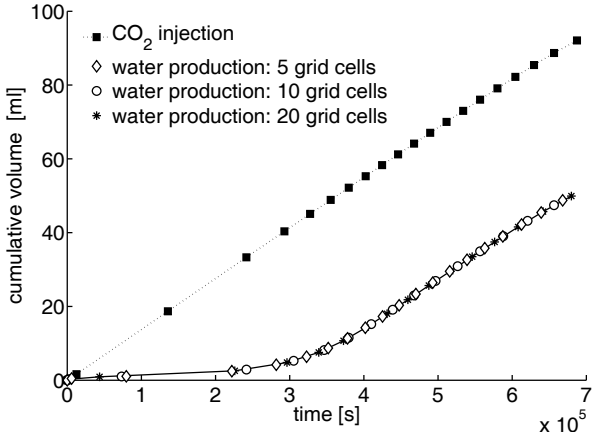

Figure 2.18 Numerical computations for CO_2 injection at atmospheric conditions for 3 different discretizations. As input parameters we have: $u_{g,inj} = 0.5$ ml/h, $D_L = 1 \times 10^{-2}$ m, $T = 28$ °C and the capillary pressure data from experiment 6 (see Table B.1). No effect of the grid size on the water production behavior is computed.

The negative secondary imbibition capillary pressures, measured for $S_w > 0.5$ (Figure 2.9), indicate that the CO_2-water-sand system becomes intermediate wet. *Chiquet et al.* [2005] already concluded that the wettability of minerals, such as quartz, can be significantly altered in the presence of CO_2 under typical sequestration conditions. For these high pressures and temperatures, the solvent properties of CO_2 improve and together with the decrease of pH of water, the surface charges become less negative. This will reduce the electrostatic interfacial forces that favor positive capillary pressures. In addition to this, the contact angle increases for supercritical conditions. This is shown in Figure 2.11, which shows that imbibition capillary pressure does not scale with the interfacial tension.

To obtain a correct interpretation of the diffusion and dissolution mechanisms, and their impact on the capillary pressure, the experimental results for the water production and the gas injection behavior are compared to the model predictions. From the numerical simulations it appears that the results in cumulative volumes are independent of the discretization (Figure 2.18). The injection and production characteristics for the primary drainage experiments with N_2 and CO_2 are presented in Figure 12-16. Good agreement between the predicted and measured volumes is found for both the low and high pressure conditions.

For the 8 bar N_2 experiment (Figure 2.13), the measured water production curve is on average a straight line, which is also predicted by the model. Due to the low solubility of N_2 in water ($k_H \approx 8\times10^9$ Pa), the mass transfer rate, defined by the right hand side of Eq. B.2, does not have a significant effect on the water production curves.

Contrary to the experiments with N_2, the dissolution rate and the diffusion of CO_2 in water influence the water production profiles for $P = P_{atm}$ and $P = 8$ bar (see Figures 2.14 and 2.15). The water production during CO_2 injection at atmospheric conditions (Figure 2.14) is initiated very slowly (stage 1) because the CO_2 dissolves into the water and the process is dominated by diffusion. The duration of stage 1 corresponds to the characteristic diffusion time, defined by $t_c = H^2 / D_g$. Because the water saturation does not decrease significantly, we assume H (the water column in the sample) to be constant during stage 1. For constant H and $D_g = 2\times10^{-9}\,\mathrm{m^2/s}$ [*Gmelin*, 1973], $t_c \approx 3$ days. For $t > t_c$, the gas pressure starts to build up and the water production increases (stage 2). Subsequently, the production curve becomes parallel to the gas injection profile, until S_{wc} has reached (stage 3). From this moment the water production is almost horizontal (stage 4).

For the 8 bar CO_2 experiment, (Figure 2.15), different boundary conditions were applied ($P_{g,z=0} = \text{constant}$, $u_{w,z=-L} = \text{constant}$). The constant water production is indicated by the constant slope. Similar to the atmospheric case (experiment 6) the gas injection curve is subject to the CO_2 dissolution rate in the first stage of the experiment, $t < 1.2\times10^5$ s. As a result of the constant water production, the water column in the sample decreases, which results in a smaller t_c. The model predicts similar behavior as observed during the measurement. However, a discrepancy in cumulative gas production is found between the simulated and measured data after $t \approx 1.5\times10^5$ s. This results in an underestimation of the predicted cumulative CO_2 volume at the end of 12.2 ml.

For the liquid CO_2 case (Figure 2.16) the dissolution and diffusion effects do not influence the water production behavior, and both the experimental and numerical results show an incompressible-like displacement. Because $c_{gg} >> c_{wg}^{eq}$ (Eq. B.2), the influence of the mass transfer on the CO_2 pressure, is negligible. Here, c_{gg} is the concentration of CO_2 in the liquid CO_2 phase. Comparison of experiment 12 with experiments 6 and 10, shows that the solubility of gaseous CO_2 is relatively smaller than for liquid CO_2 [*Duan and Sun*, 2003]. A small deviation in cumulative

production and injection of approximately 1 ml is found over the period $t < 4 \times 10^5$ s. Different mass transfer rates are investigated for the liquid CO_2 conditions, and indeed, no effect on the water production profiles is predicted.
The comparison between the gaseous CO_2 and N_2 experiments shows the large effect of the dissolution of CO_2 on the injection/production behavior. However, the capillary pressure is not influenced by dissolution effects, because the capillary pressure curves obtained for the CO_2-water and N_2-water system (Figures 2.5 and 2.6) are all in the same range.

2.6 Conclusions

- A capillary pressure set-up has been developed and validated that can be used to measure the capillary pressure behavior for CO_2 sequestration applications.
- For the small injection rates applied, the viscous forces are negligible and the capillary pressure curves are considered as static.
- The numerical results show that the *SIPERM* filters do not influence the measured $P_c - S_w$ curves for the applied flow conditions.
- Increasing CO_2 pressures result in decreasing primary drainage capillary pressures for all samples used. This can be explained by the decrease in interfacial tension [*Chun and Wilkinson*, 1995].
- From the comparison between the N_2 and CO_2 experiments, we conclude that the capillary pressure is not influenced by the dissolution of CO_2 in water.
- Measurements close to the critical point of CO_2 show alternate drainage and imbibition events during CO_2 injection. This is a result of small perturbations that change the density and viscosity of CO_2 and temporary CO_2 wet behavior.
- The wettability of the quartz sand is altered to intermediate wet in the presence of CO_2 under supercritical conditions. This is a result of improving solvent properties of CO_2 and the decreasing pH of water [*Chiquet et al.*, 2005].
- Good agreement is found between the experimental results and the model prediction for both the CO_2 and N_2 injection drainage experiments.
- The model shows that the water production and gas injection behavior depends largely on mass transfer rate and diffusion of CO_2 in water. These effects become negligible for the injection of liquid CO_2.
- The capillary pressure behavior must be considered in CO_2 sequestration application, e.g., the caprock integrity [*Chiquet et al.*, 2005] and drainage and

imbibition events in heterogeneous rocks [*van Lingen et al.*, 1996]. Our measurements show that wetting alteration and the abrupt phase changes and accompanying density and viscosity changes may affect the success of CO_2 sequestration.

Bibliography

Anderson, W. G. (1987), Wettability literature survey - Part 4: Effects of wettability on capillary pressure, *JPT*, 1283–1300, SPE 15271.

Bennion, B., and S. Bachu (2006a), The impact of interfacial tension and pore-size distribution/capillary pressure character on CO_2 relative permeability at reservoir conditions in CO_2-brine systems, paper presented in SPE/DOE Symposium on Improved Oil Recovery, 22-26 April, Tulsa, Oklahoma, USA, SPE 99325-MS.

Bennion, D. B., and S. Bachu (2006b), Supercritical CO_2 and H_2S-brine drainage and imbibition relative permeability relationships for intergranular sandstone and carbonate formations, paper presented in SPE Europec/EAGE Annual Conference and Exhibition, 12-15 June, Vienna, Austria, SPE 99326-MS.

Chiquet, P., D. Broseta, and S. Thibeau (2005), Capillary alteration of shaly caprocks by carbon dioxide, paper presented in SPE Europec/EAGE Annual Conference, 13-16 June, Madrid, Spain, SPE 94183-MS.

Christoffersen, K. R., and C. H. Whitson (1995), Gas/oil capillary pressure of chalk at elevated pressures, *SPE Formation Eval.*, *10 (6)*, 153–159, SPE 26673-PA.

Chun, B. -S., and G. T. Wilkinson (1995), Interfacial tension in high-pressure carbon dioxide mixtures, *Ind. Eng. Chem. Res., 34*, 4371–4377.

Class, H., R. Helmig, and P. Bastian (2002), Numerical simulation of non-isothermal multiphase multicomponent processes in porous media. 1. An efficient solution technique, *Adv. Water Resour., 25*, 533–550.

Doughty, C., and K. Pruess (2004), Modeling supercritical carbon dioxide injection in heterogeneous porous media, *Vadose Zone J.*, *3*, 837–847.

Duan, Z., and R. Sun (2003), An improved model calculation CO_2 solubility in pure water and aqueous NaCl solutions from 273 to 533 K and from 0 to 2000 bar, *Chem. Geology, 193*, 257–271.

Ebigbo, A., A. Bielinski, A. Kopp, H. Class, and R. Helmig (2006), Numerical modeling of CO_2 sequestration with MUFTE-UG, paper presented in CMWR XVI, June, Copenhagen.

Fenghour, A., W. A. Wakeham, and V. Vesovic (1999), The viscosity of carbon dioxide, *J. Phys. Chem. Ref. Data, 27 (1)*, 31–44.

Firoozabadi, A., and K. Aziz (1986), Relative permeability from centrifuge data, paper presented in SPE California Regional Meeting, 2-4 April, Oakland, California, SPE 15059.

Gmelin, L. (1973), Gmelin Handbuch der Anorganischen Chemie, 8. Auflage Kohlenstoff, Teil C3, Verbindungen.

Hammervold, W. L., O. Knutsen, J. E. Iversen, and S. M. Skjaeveland (1998), Capillary pressure scanning curves by micropore membrane technique, *J. Petrol. Sci. Eng., 20 (3)*, 253–258.

Hassanizadeh, S.M., and W. G. Gray (1993), Thermodynamic basis of capillary pressure in porous media, *Water Resources Research, 29 (10)*, 3389–3405.

Honarpour, M. M., D. D. Huang, and A. H. Dogru (1996), Simultaneous measurements of relative permeability, capillary pressure, and electrical resistivity with microwave system for saturation monitoring, *SPE J., 1 (3)*, 283–294, SPE 30540.

Izgec, O., B. Demiral, H. Bertin, and S. Akin (2005), Experimental and numerical investigation of carbon sequestration in saline aquifers, paper presented in SPE/EPA/DOE Exploration and Production Environmental Conference, Galveston, Texas, SPE 94697-STU.

Jennings, J. W., D. S. McGregor, and R. A. Morse (1988), Simultaneous determination of capillary pressure and relative permeability by automatic history matching, *SPE Formation Eval.*, *3 (3)*, 322–328.

Jimenez, J. A., and R. J. Chalaturnyk (2002), Integrity of bounding seals for geological storage of greenhouse gases, paper presented in SPE/ISRM Rock Mechanics Conference, 20-23 October, Irving, Texas, SPE 78196-MS.

Kalaydjian, F. J-M. (1992), Dynamic capillary pressure curve for water/oil displacement in porous media: Theory vs. experiment, paper presented in SPE Annual Technical Conference and Exhibition, 4-7 October, Washington, D.C., pp. 491–506, SPE 24813.

Kokkedee, J. A. (1994), Simultaneous determination of capillary pressure and relative permeability of a displaced phase, paper presented at European Petroleum Conference, London, 25-27 October, 213–222.

Kumar, A., R. Ozah, M. Noh, G. A. Pope, S. Bryant, K. Sepehrnoori, and L. W. Lake (2005), Reservoir simulation of CO_2 storage in deep saline aquifers, *SPE J., 10 (3)*, 336–348, SPE 89343-PA.

Labastie, A., M. Guy, J. P. DelClaud, and R. Iffly (1980), Effects of flow rate and wettability on water-oil relative permeabilities and capillary pressure, paper presented in SPE Annual Technical Conference and Exhibition, 21-24 September, Dallas, Texas, SPE 9236-MS.

Longeron, D., W. L. Hammervold, and S. M. Skjaeveland (1995), Water-oil capillary pressure and wettability measurements using micropore membrane technique, paper presented at International Meeting on Petroleum Engineering, Beijing, 14-17 November, pp. 543–553, SPE 30006.

Mazumder, S., W.-J. Plug, and J. Bruining (2003), Capillary pressure and wettability behavior of coal-water-carbon dioxide system, paper presented at SPE Annual Technical Conference and Exhibition, Denver, Co., 5-8 October, SPE 84339.

Morrow, N. R. (1970), Physics and thermodynamics of capillary action in porous media, *Ind. Eng. Chem., 62 (6)*, 32–56.

Newsham, K. E., J. A. Rushing, P. M. Lasswell, J. C. Cox, and T. A. Blasingame (2004), Comparative study of laboratory techniques for measuring capillary pressures in tight gas sands, paper presented at SPE Annual Technical Conference and Exhibition, Houston, Texas, 26-29 September, SPE 89866.

Nordbotten, J. M., M. A. Celia, and S. Bachu (2005), Injection and storage of CO_2 in deep saline aquifers: Analytical solution for CO_2 plume evolution during injection, *Transp. Porous Media, 58 (3)*, 339–360.

O'Caroll, D. M., T. J. Phelan, and L. M. Abriola (2005), Exploring dynamic effects in capillary pressure in multistep outflow experiments, *Water Resources Research, 41*, 1–14.

Plug, W.-J., S. Mazumder, J. Bruining, N. Siemons, and K. Wolf (2006), Capillary pressure and wettability behavior of the coal-water-carbon dioxide system at high pressures, paper presented at 2006 Int. CBM Symposium, Tuscaloosa, Al., 22-26 May.

Plug, W-J., E. C. Slob, J. Bruining, and L. M. Moreno-Tirado (2007), Simultaneous measurement of hysteresis in capillary pressure and electric permittivity for multiphase flow through porous media, *Geophysics Letters, 72 (3)*, A41–A45.

Pruess, K., and J. Garcia (2002), Multiphase flow dynamics during CO_2 injection into saline aquifers, *Environmental Geology, 42*, 282 – 295.

Reeves, P. C., and M. A., Celia (1996), A functional relationship between capillary pressure, saturation and interfacial area as revealed by a pore-scale network model, *Water Resources Research, 32 (8)*, 2345–2358.

Siemons, N., J. Bruining, H. Castelijns, and K. Wolf (2006a), Pressure dependence of the contact angle in a CO_2-H_2O-coal system, *J. Colloid. Sci., 297 (2)*, 755–761.

Siemons, N., J. Bruining, K. Wolf, and W. J. Plug (2006b), Pressure dependence of the CO_2 contact angle on bituminous coal and semi-anthracite in water, paper presented at 2006 Int. CBM Symposium, Tuscaloosa, Al., 22-26 May.

Span, R., and W. Wagner (1996), A new equation of state for carbon dioxide covering the fluid region from the triple-point temperature to 1100 K at pressures up to 800 MPa, *J. Phys. Chem. Ref. Data, 25 (6)*, 1509–1596.

Spycher, N., K. Pruess, and J. Ennis-King (2003), CO_2-H_2O mixtures in the geological sequestration of CO_2. I. Assesment and calculation of mutual solubilities from 12 to 1000°C and up to 600 bar, *Geochimica et Cosmochimica Acta, 67 (16)*, 3015–3031.

Topp, G. C., A. Klute, and D. B. Peters (1967), Comparison of water content-pressure head data obtained by equilibrium, steady-state, and unsteady-state methods, *Soil Sci. Soc. Am. Proc.*, *31*, 312–314.

van Duijn, C. J., and M. de Neef (1995), The effect of capillary forces on immiscible two-phase flow in strongly heterogeneous porous media, Report, TU Delft.

van Lingen, P. P., J. Bruining, and C. P. J. W. van Kruijsdijk (1996), Capillary entrapment caused by small-scale wettability heterogeneities, *SPE Res. Eng., 11 (2)*, 93–100.

van Lingen, P. P. (1998), Quantification and reduction of capillary entrapment in cross-laminated oil reservoirs, Ph.D. thesis, Delft University of Technology.

Wanna-Etyem, C. (1982), Static and dynamic water content - pressure head relations of porous media., Ph.D. thesis, Colorado State University, Fort Collins, CO.

Wiebe, R., and V. L. Gaddy (1940), The solubility of carbon dioxide in water at various temperatures from 12 to 400°C and at pressures to 500 atmospheres. Critical phenomena, *J. Am. Chem. Soc., 62*, 815–817.

Wildenschild, D., J. W. Hopmans, and J. Simunek (2001), Flow rate dependence of soil hydraulic characteristics, *Soil Sci. Soc. Am. J.*, *65*, 35–48.

Chapter 3 Capillary pressure and wettability behavior of the coal-CO_2-water system[2]

3.1 Introduction

Geological sequestration [*Orr*, 2004] of carbon dioxide (CO_2) is one of the viable methods to stabilize the concentration of greenhouse gases in the atmosphere and to satisfy the Kyoto protocol. The main storage options are depleted oil and gas reservoirs [*Pawar*, 2004; *Shtepani*, 2006], deep (saline) aquifers [*Pruess et al.*, 2003; *Pruess*, 2004; *Kumar et al.*, 2005], and unmineable coal beds [*Reeves*, 2001]. Laboratory studies and recent pilot field tests [*Mavor et al.*, 2004; *Pagnier et al.*, 2005] demonstrate that CO_2 injection has the potential to enhance methane (CH_4) production from coal seams. This technology can be used to sequester large volumes of CO_2, thereby reducing emissions of industrial CO_2 as a greenhouse gas. The efficiency of CO_2 sequestration in coal seams (ECBM) strongly depends on the coal type, the pressure and temperature conditions of the reservoir [*Siemons et al.*, 2006a,b] and the interfacial interactions of the coal-gas-water system [*Gutierrez-Rodriguez et al.*, 1984; *Gutierrez-Rodriguez and Aplan*, 1984]. It can be expected that in highly fractured coal systems the wetting behavior positively influences the efficiency of ECBM. It is generally accepted that the coal structure consists of the macro cleat and fracture system ($>$ 50 nm) and the coal matrix ($<$ 50 nm). The macro fracture system is initially filled with water and provides the conduits where the mass flow is dominated by Darcy's law. The coal matrix can be subdivided in meso cleats (from 2 to 50 nm), micro cleats (from 0.8 to 2 nm) and the micro pores ($<$ 0.8 nm). The matrix system is relatively impermeable and the mass transfer is dominated by diffusion. After a dewatering stage, CO_2 is injected and flows through the larger cleats of the coal. Subsequently CO_2 is transported through the smaller cleats and is sorbed in the matrix blocks [*Siemons et al.*, 2006a].

[2] This chapter is submitted to SPE Journal, November 1, 2006, and is based on SPE 84339 and the conference proceedings for the International CBM Symposium, Tuscaloosa, 2006, paper 606.

Depending on the wettability of coal we can distinguish the following gas exchange mechanisms:

- The coal is water-wet and CO_2 and CH_4 diffuse in the water filled cleats.
- The coal is CO_2-wet or gas-wet and counter-current capillary diffusion can take place.
- The coal is gas-wet and binary diffusion of CO_2 and CH_4 occurs.

Capillary diffusion finds its origin in capillary pressure (P_c) effects where P_c is defined as the pressure difference between the non-aqueous and aqueous phase. The storage rate for CO_2 is much smaller if the micro cleat system is water-wet. This is because of the small CO_2 molecular diffusion coefficient ($D_{CO_2} \approx 2\times10^{-9}\,\mathrm{m^2/s}$). For gas-wet conditions a faster and more efficient sorption rate is expected and the molecular diffusion is much larger, i.e., $D_{CO_2} \approx 1.7\times10^{-7}\,\mathrm{m^2/s}$ at 100 bar [*Bird et al.*, 1960]. Therefore, we assert that the wettability of coal is important for ECBM applications. For this reason we have undertaken an experimental study to investigate the wetting properties of different coal types under ECBM conditions, measuring capillary pressure curves. The dissolution properties of CO_2 in water [*Wiebe and Gaddy*, 1940], the interfacial tension between water and CO_2 [*Chun and Wilkinson*, 1995] and the CO_2 sorption [*Siemons et al.*, 2003] play an important role in the interpretation of capillary pressure experiments. The CO_2 will sorb on the coal and will cause a swelling induced permeability decrease [*Mazumder et al.*, 2006]. The higher the pressure the more CO_2 can be sorbed and the more the coal swells [*Reucroft and Sethuraman*, 1987]. The largest amount of sorption induced swelling in intact coal is approximately 4%. It is found that the swelling for grounded coal is much higher than intact coal and has been reported to be in the order of 15-20%. The swelling causes a porosity reduction and hence the water saturation increases.

In Section 3.2 relevant literature about the wettability of coal and the capillary pressure is summarized. Section 3.3 describes the experimental set-up we have developed, to measure the capillary pressure as function of the CO_2 pressure. Furthermore, we describe the sample preparation and experimental procedure. In Section 3.4 the experimental results are presented and discussed. We end with the conclusions.

3.2 Wettability of coal

Several methods exist to measure the wettability of rocks. We mention contact angle measurements, imbibition and forced displacement (Amott-test), the USBM wettability method and capillary pressure curves [*Anderson*, 1986]. Investigations of the wettability of coal reported in the literature are predominantly based on contact angle measurements for the coal-air-water system at atmospheric pressures. In general, these measurements are performed by direct observations of drops attached to the solid, and viewed from one side [*Siemons et al.*, 2006].

Dry coal, like dry sand, is naturally hydrophobic and its hydrophobicity varies from one sample to the other resulting from the variation in coalification, genesis and composition of coal [*Gutierrez-Rodriguez et al.* 1984]. Previous studies [*Gutierrez-Rodriguez et al.* 1984; *Gutierrez-Rodriguez and Aplan*, 1984; *Orumwense*, 2001] were conducted to investigate the hydrophobicity of different coal types. A comparative study of contact angles of air bubbles, oils, flocculants and coagulant drops on flat polished coal surfaces immersed in water, was carried out by *Orumwense* [2001]. From these experiments a positive correlation between hydrophobicity and the coal rank of vitrinite rich coals was found. He also concluded that the hydrophobicity of coal decreased with decreasing fixed carbon and total carbon content. A series of experiments have been carried out by *Gutierrez-Rodriguez et al.* [1984] and *Gutierrez-Rodriguez and Aplan* [1984] with air and water for different coal types, varying from high to low rank. Qualitatively the same results were reported as found by *Orumwense* [2001]. *Murata* [1981] concluded that the contact angle depends on the hydrogen and oxygen content of the coal. *Chi et al.* [1988] observed an increasing contact angle between CO_2 and water on a coal surface with increasing pressures. Moreover, water-wet behavior was found when the ash content of the coal increased. Contact angle measurements for the coal-CO_2-water system, using the pendant drop cell, were carried out by *Siemons et al.* [2006a,b]. They concluded that wetting alteration from water-wet to CO_2-wet, for high rank coal already occurred at pressures above 2.7 bar. For medium rank coal the alteration was observed for pressures in the range of 80-85 bar.

3.3 Capillary pressure in porous media

We measure capillary pressure curves to investigate the wettability of the coal-CO_2-distilled water system at different CO_2 pressures in the range from 1 to 100 bar [*Plug et al.*, 2006]. In this study we use a medium rank coal (Warndt-Luisenthal, Germany) and a high rank coal (Selar-Cornish, England) [*Siemons et al.*, 2006b]. To facilitate the interpretation of these measurements we also obtain capillary pressure curves for unconsolidated sand samples. Conventional methodologies to determine capillary pressures are the porous plate technique [*Christoffersen and Whitson*, 1995], the micro-pore membrane technique [*Jennings et al.*, 1988; *Longeron et al.*, 1995], mercury drainage experiments [*Anderson*, 1987] and the centrifuge method [*Newsham et al.*, 2004]. Conventional capillary pressure studies measure at static conditions, e.g., the multi-step method, where an equilibrium water saturation (S_w) distribution is established [*Hassanizadeh et al.*, 2002]. Experimental data are also available in the literature for transient conditions, in which a continuous phase injection is applied [*Kokkedee*, 1994; *Wildenschild et al.*, 2001]. Static P_c measurements are time consuming; therefore we choose the quasi-static approach. This method has the advantage that static P_c curves can be obtained for small flow rates (0.01 to 0.1 PV/h).

Capillary pressure measurements at reservoir conditions are mainly reported for the oil/water and the oil/gas system [*Christoffersen and Whitson*, 1995], with the application to enhanced oil recovery. To our knowledge capillary pressure between CO_2 and water in coal has not been investigated. *Dabbous et al.* [1976] measured the drainage capillary pressure between air and water of a Pocahontas and Pittsburgh coal at various pressure conditions. They found positive valued capillary pressure curves for both samples. In this paper we define drainage as injection of the non-aqueous phase to displace the water and imbibition as the reverse process. These definitions are maintained regardless of the wetting conditions of the porous medium considered.

3.4 Experimental design

3.4.1 Experimental set-up

The equipment is an optimized version of the set-up presented in the work of *Mazumder et al.* [2003] and is based on the porous plate technique combined with the micropore membrane technique, extensively discussed by *Christoffersen and Whitson* [1995], *Jennings et al.* [1988], *Longeron et al.* [1995] and *Kokkedee* [1994]. A schematic diagram of the set-up is shown in Figure 3.1.

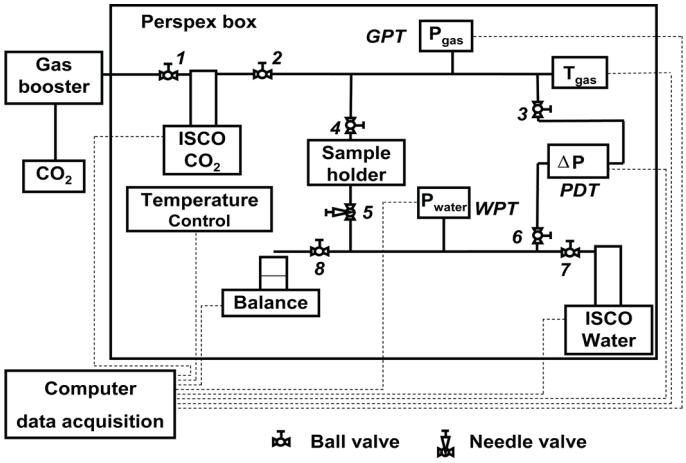

Figure 3.1 Schematic view of the set-up

Two syringe pumps (ISCO pump, 260D) are connected to the in- and outlet of the sample holder (Figure 3.2) and can be set to a constant injection rate (± 0.005 ml/h) or a constant pressure (± 0.1 bar). The gas phase is injected or produced at the top of the sample holder and the water is collected or injected at the bottom using the second syringe pump for pressures >1 bar. For primary drainage experiments at atmospheric conditions, valve 7 is closed and valve 8 is open and the water is produced in a beaker placed on a balance (± 0.005 g). A layer of paraffin on top of the water surface avoids evaporation. The gas pressure transducer (GPT) and the water pressure transducer (WPT) record the single-phase pressures (0-100 bar, ± 0.01 bar).

The differential pressure between the gas and the water phase is measured by the pressure difference transducer (PDT, 0-500 mbar, ± 0.1 mbar), which is positioned

at the same height as the middle of the sample, such that no correction for gravity effects is required.

To maintain a constant temperature we cover the entire set-up with a Perspex box, sealed by polystyrene. Inside the box two 60 W light-bulbs, those switch on and off, regulate the temperature in the range from 25 to $40 \pm 0.5\,°C$. We enable temperature equilibration for at least two days for gaseous and liquid CO_2/N_2 and at least three days when supercritical CO_2 is used.

3.4.2 The sample holder

The sample holder, see Figure 3.2, consists of a stainless steel ring that contains the unconsolidated sample. The grains are kept in place using a combination of pates at the top and bottom of the sample. At the bottom, two porous plates (SIPERM *R*, Cr-Steel basis) with a permeability of $2\times10^{-12}\,m^2$ and a porosity of 0.32, support the sample and protect the hydrophilic membrane. Two stainless steel plates, both with 32 perforations ($D_p = 5\,mm$), are used at the top directly above the sample in combination with a nylon filter.

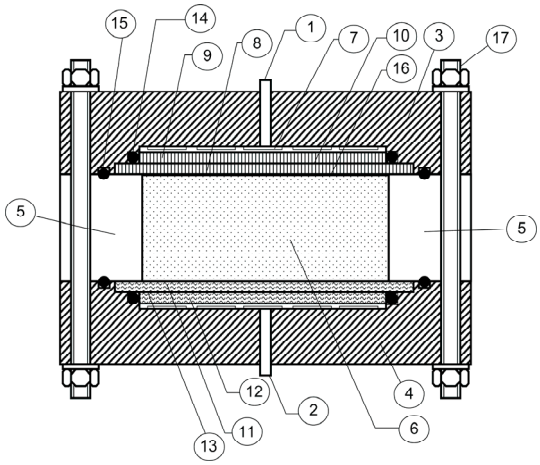

Figure 3.2 Cross section of the sample-holder: 1. gas-inlet; 2. water-inlet; 3. stainless steel end-piece 1; 4. stainless steel end-piece 2; 5. stainless steel ring (height $H = 25\,mm$); 6. porous medium (diameter, $D_{sample} = 84\,mm$); 7. concentric grooves; 8. perforated plate (diameter, $D_{ss,1} = 90\,mm$); 9. perforated plate (diameter, $D_{ss,2} = 84\,mm$); 10. hydrophobic filter (diameter, $D_w = 90\,mm$, pore size, 0.45 μm); 11. SIPERM filter (diameter, $D_{s,1} = 90\,mm$); 12. SIPERM filter (diameter, $D_{s,2} = 84\,mm$); 13. water-wet filter (diameter, $D_G = 90\,mm$, pore size, 0.1 μm); 14. O-rings (2.1 mm); 15. O-rings (4 mm); 16. nylon filter (pore size 210 μm); 17. stainless steel bolts.

Between the plates, a hydrophobic membrane is placed for the primary imbibition process, prohibiting water production (Figure 3.2). To avoid leakage of gas or water over the hydrophobic or hydrophilic membranes, we seal the outer perimeter with a Viton O-ring. Concentric flow grooves in the end-pieces redistribute the injected and produced phase over the total sample area to avoid preferential flow and fast breakthrough of the injected phase.

3.4.3 Sample description and preparation

Four types of unconsolidated rock material are used; a fine grained sand, a coarse grained sand, a medium rank coal and a high rank coal. The first series of experiments are conducted on unconsolidated quartz sand using CO_2 and N_2 as the non-wetting phase. The fine grained sand sample has an average grain size of $160 < D_{50} < 210\,\mu m$. Capillary pressure curves are obtained to investigate the reproducibility and accuracy of the experimental technique. For comparison of the behavior of the coal samples, capillary pressure curves for the coarse sand, $360 < D_{50} < 410\,\mu m$, are obtained with comparable grain diameters as the coal.

For the examination of the capillary pressure and wettability in coal we choose two coal samples as used in the work of *Siemons et al.* [2006a,b]. The medium rank Warndt-Luisenthal coal is high in volatile matter content and low in fixed carbon content compared to the high rank Selar-Cornish sample (see Table 3.1). The coal samples are collected from a coal matrix, of which 2 kg of coal has been crushed in different grain size fractions. For the coal experiments we use grain size fractions of $500 < D_{50} < 630\,\mu m$. The moisture and ash content are determined according to the ASTM3173 and ASTM3174 standard methods.
We use grounded coal samples for the experiments to expose the relevant surface area to water and CO_2. Volumetric physisorption of CO_2 at 0°C was done to determine the micro pore area and micro pore volume of the void space. These data alongside with the composition of the coal samples are reported in Table 3.1.

Sample	*Warndt-Luisenthal*	*Selar-Cornish*
Location	Saarbrücken, Germany	Selar, South Wales, UK
Stratigraphy	Westphalian C	Westphalian B
Proximate analysis		
rank	hvBb*	Semi-anthracite
moisture [%]	1.39	1.26
Volatile matter (w.f.) [%]	40.51	10.35
Ash (w.f.) [%]	2.77	3.94
Fixed Carbon (d.a.f.) [%]	58.36	89.27
Ultimate analysis		
Carbon [%]	81.3	85.68
Hydrogen [%]	5.58	3.36
Nitrogen [%]	1.88	1.56
Sulphur [%]	0.69	0.68
Oxygen (diff.) [%]	5.47	5.58
H/C	0.82	0.47
O/C	0.05	0.05
Coal Petrology		
V_{max} [%]	0.71	2.41
Vitrinite	74.4	73.6
Liptinite	15.6	0
Inertinite	9	24.6
Minerals	1	1.8
Internal properties		
Specific surface [m^2/g]	104	208
Micropore volume [cm^3/g]	0.03545	0.071

* high volatile Bituminous b

Table 3.1 Coal properties of the medium rank and high rank coal

3.4.4 Experimental procedure

Before the start of each experiment the set-up is cleaned and the porous plates are dried. The assembling of the sample holder is from the bottom upward (see Figure 3.2). For each experiment we use new Millipore filters and new Viton O-rings. When end-piece 2 inclusive the SIPERM filters and O-rings, and the stainless steel

ring are mounted together, we pour the unconsolidated sample in the sample holder. The sample is vibrated for 10 min to obtain a better packing. Finally we put end-piece 1, inclusive the perforated plates, the hydrophobic filter, the nylon filter and O-rings, on top of the stainless steel ring. Now, the sample holder is placed in between valve 4 and 5 (Figure 3.1) and the entire system is evacuated for 1 hour. The porosity, φ, is determined with helium. For the sand and coal samples we found a porosity of 0.36-0.38 and 0.42-0.45 respectively. Subsequently the total system is again evacuated for 1 hour and filled with either water or gas.
When an experiment starts with the primary drainage process, the hydrophobic filter is left out. This makes it easier to pressurize the system. Through the high pressure, small air bubbles carried along with the distilled water are dissolved. In the same way, the hydrophilic filter is removed for primary imbibition tests. In this work we consider 3 types of experiments:

Case 1: Primary drainage at atmospheric pressure, $P = P_{atm}$
The total sample holder is initially filled with water from valve 4 up to valve 5 (Figure 3.1). Subsequently the water pump is used to apply a pressure of 10 bar to remove all possible air and to obtain 100% water saturation and valve 7 is closed. The gas tubing and pump are flushed and filled with either N_2 or CO_2. Finally we set a constant temperature and let the system equilibrate. We open valve 8 and the water pressure decreases towards atmospheric pressure. The primary drainage experiment starts when a constant gas injection rate is applied and valve 4 is opened. Because of operational restrictions of the syringe pumps for pressures less than 1 bar, no secondary imbibition tests are performed for atmospheric conditions.

Case 2: Primary drainage and secondary imbibition at P>1 bar
For these experiments the sample holder is initially filled with water and the water pump is set to the pressure we apply during the drainage experiment. Valve 4 is closed and the gas tubing and pump are filled with either N_2 or CO_2. A gas booster, connected to valve 1 (see Figure 3.1) is used to bring up the gas pressure. We set a constant temperature and let the system equilibrate. Subsequently, when both the water and gas pressure are equal, a constant gas injection rate is applied, the water pump is set to a constant pressure and valve 4 is opened. After the primary drainage process, the secondary imbibition process starts when the water pump is

set to a constant injection rate and the gas pump is set to a constant production pressure.

Case 3: Primary imbibition and secondary drainage at high pressures, P>1bar
The total sample holder is initially filled with gas from valve 4 (open) up to valve 5 (see Figure 3.1) and the water pump and tubing are filled and flushed with water. The absolute pressure is kept constant by the gas pump and the water pressure in the tubing is increased using the water pump. We set a constant temperature and let the system equilibrate. The primary imbibition starts when a constant water injection rate is applied, the gas pump is set to a constant pressure and valve 5 is opened. After the primary imbibition process, the secondary drainage process starts when the water pump is set to a constant production pressure and the gas pump is set to a constant injection rate.

3.4.5 Data analysis

The water saturation is obtained by the mass of water produced for the atmospheric conditions and by the change in volume of the water pump for high pressure conditions ($P > 1$ bar). Moreover the integral mass balance is checked by weighing all the separate parts of the sample holder at the end of the experiment, from which an estimation of the final water saturation in the sample can be obtained.
For the high pressure drainage experiments the amount of water in the pump is measured to validate whether negligible amounts of free gas are produced only. For imbibition tests we apply essentially the same procedure to validate that there is only negligible water production. It turns out that the gas volume in the water pump never exceeds one percent of the volume [*Jennings et al.*, 1988]. The capillary pressure curves are obtained based on the following:

- The decrease (increase) in water saturation is computed from the mass produced (injected).
- The initial water (gas) saturation for primary drainage (imbibition) is 1.
- The viscous pressure drop over the sample holder is negligible (0.04 Pa).
- For the drainage experiments all the water from end-piece 1 and the perforated plates is drained before to the gas reaches the sample (Figure 3.2).
- During the drainage process all the water remains in pore space of the SIPERM plates, hydrophilic filter and the void of end-piece 2 (Figure 3.2).

- A sudden pressure drop marks the beginning of the primary imbibition process, independent of the water volume injected.
- Compressibility of water is neglected for all pressure conditions.
- The porosity for all samples used is assumed constant during the drainage and imbibition processes.

3.5 Results and discussion

We have tested the experimental method for both the fine and coarse grained unconsolidated sand samples applying different temperature and pressure conditions using either N_2 or CO_2. Moreover, a comprehensive analysis can be done by comparison of the coal measurements with the results obtained for the coarse sand sample.

3.5.1 Capillary pressure of the unconsolidated sand-CO_2-water system

Here we describe the precision of the experimental method and the influence of the applied flow rates on the $P_c - S_w$ curves. The precision is estimated from the reproducibility of 3 experiments conducted on three different fine sand samples at ambient conditions (see Figure 3.3). The highest precision ($\pm$1.5mbar) is found for the intermediate water saturation range ($0.4 < S_w < 0.8$). Near the end point saturations the precision of the measurements is ± 3 mbar. In experiment 4 (Figure 3.4) the gas injection rate is altered between 0 and 1 ml/h to investigate the influence of viscous forces and the possible dynamic behavior on P_c for the applied conditions. No significant effect in capillary pressure is observed for increasing or decreasing injection rates.

We measure drainage and imbibition curves on the coarse sand sample for elevated pressures and temperatures. A decrease in capillary pressure is measured for increasing CO_2 pressures (see Figure 3.4). This is a result of the pressure dependence of the interfacial tension [*Chun and Wilkinson*, 1995]. Hence, the capillary pressure curves can be scaled according to the interfacial tension. From Figure 3.4, it can be seen that the capillary pressure for liquid CO_2 (experiment 6) and supercritical CO_2 (experiment 7) have approximately the same values. The irregular behavior of the primary drainage experiment measured for experiment 7 (Figure 3.4) is ascribed to phase instabilities in the vicinity of the critical point.

Small system perturbations, like temperature variations and corresponding thermal expansion effects, will cause occasional water imbibition during continuous CO_2 injection. Moreover, for all cases the capillary pressure is positive.

In Figure 3.5 the secondary imbibition curves for experiment 5 and 7 are presented. For the supercritical conditions (experiment 7) we stop the imbibition process before the residual gas saturation has been reached. A post-mortem of experiment 5 and 7 shows that no water is produced. A decrease in imbibition capillary pressure is observed for increasing CO_2 pressures. For $S_w > 0.5$, the capillary pressure becomes negative for supercritical CO_2, indicating temporary CO_2-wet behavior. A tentative explanation for this behavior is that gas trapped in the crevices of the sand only slowly dissolves in the water. Therefore the water will 'see' a surface consisting of sand and gas patches. In contrast to the supercritical drainage curve, the corresponding secondary imbibition curve, shown in Figure 3.5, is smooth. This implies that for water flow controlled processes the alternately drainage and imbibition effects do not occur.

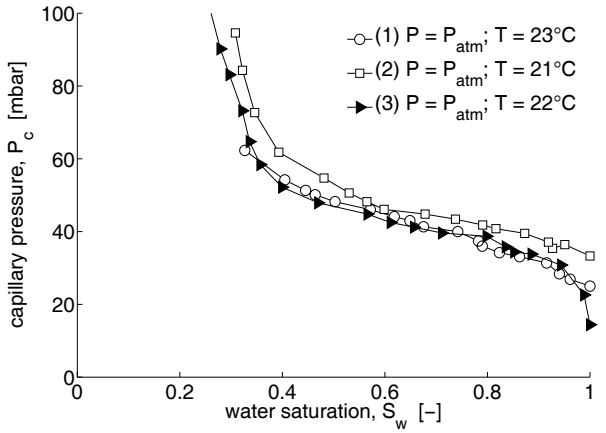

Figure 3.3 Primary drainage capillary pressure curves for CO_2 injection in fine sand ($160 < D_{50} < 210$ 1μm) for atmospheric conditions. In each case the CO_2 injection rate is 0.5 ml/h. The differences observed are an indication of the experimental precision.

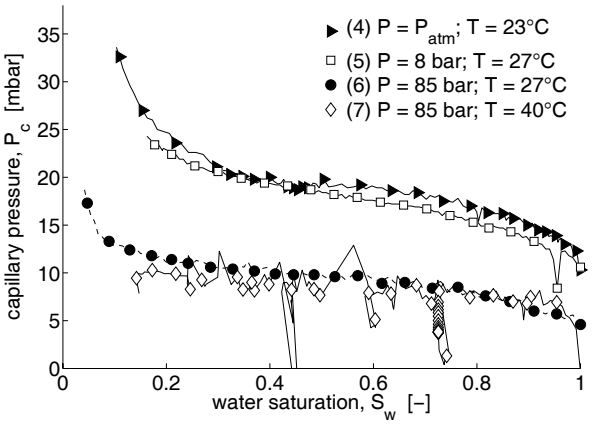

Figure 3.4 Primary drainage capillary pressure curves for CO_2 injection in coarse sand at various pressure and temperature conditions. The CO_2 injection rate is 0.5 ml/h for experiment 5, 6 and 7. Varying CO_2 injection rates are applied in experiment 4. The differences between the low and high-pressure experiments are ascribed to interfacial tension behavior.

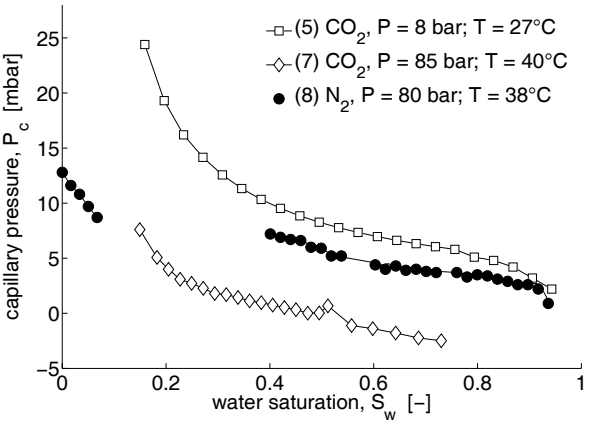

Figure 3.5 Secondary imbibition capillary pressure curves in coarse sand for the sand-CO_2-water system (experiment 5 and 7) and the primary imbibition curve for the sand-N_2-water system (experiment 8) at various pressure and temperature conditions. In each case the water injection rate is 0.5 ml/h. Note that for experiment 7 the capillary pressure becomes negative for $S_w > 0.5$.

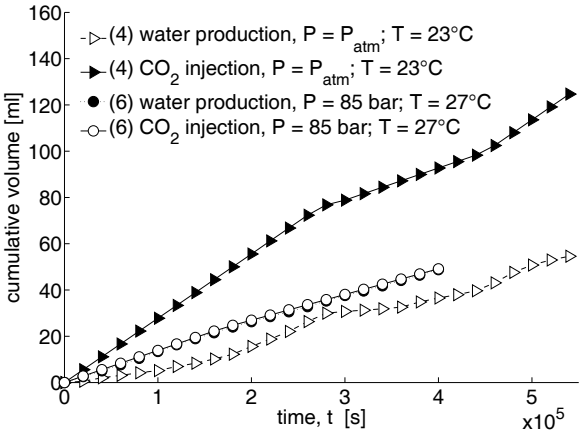

Figure 3.6 Cumulative water production and gas injection for drainage experiments in coarse sand with gaseous CO_2 (experiment 4, varying CO_2 injection rates 0.1-0.5 ml/h) and liquid CO_2 (experiment 6, CO_2 injection rate injection of 0.5 ml/h). Note that the water production and CO_2 injection curve for 85 bar coincide.

The injection and production behavior for primary drainage with CO_2 under both atmospheric pressure conditions and high pressure conditions (85 bar) is presented in Figure 3.6. The discrepancy between the injected and produced volumes for the atmospheric experiment 4 indicates the dissolution effects of CO_2 in water. However, when liquid CO_2 is injected (experiment 6) these effects are not observed and the cumulative gas volume injected is equal to the cumulative water volume produced.

We investigate the properties of the set-up during primary imbibition. Therefore, a primary imbibition experiment is conducted for the coarse sand-N_2-water system (Figure 3.5, experiment 8). Figure 3.7 plots the capillary pressure and the cumulative water injection versus time for the period before the imbibition process. Distinct events can be observed: the capillary pressure drops rapidly when the water reaches the porous plates (A) and subsequently rises towards a stable situation (B), where water is imbibing in the porous SIPERM plates until point (C). The pressure difference increases rapidly when the water starts to imbibe in the sample (D). From the water balance computation we determine that only 15% of the pore space of the porous plates is saturated. We obtain the water saturation after D, assuming that the total volume of water injected from this moment is present as pore water in the sample. The corresponding primary imbibition curve of

experiment 8 is presented in Figure 3.5. The imbibition capillary pressure curve is positive and the residual gas saturation is 0.16. Because the hydrophobic filter is used no water can be produced in the gas pump. For the water saturation range of $0.1 < S_w < 0.4$ the data acquisition system has failed.

3.5.2 Capillary pressure and wettability for the coal-CO_2-water system.

Figure 3.8 shows the reproducibility for drainage experiments for the Warndt-Luisenthal coal (medium rank) using liquid CO_2 (experiment 9, 10 and 11). The moment that the CO_2 enters the sample and the capillary entry pressure has been reached is comparable for all 3 cases. As a result of the water production history at the beginning of the experiments, small differences in starting times occur. As can be seen in Figure 3.9 smooth positive drainage curves are measured for both liquid CO_2 and gaseous CO_2 (experiment 12). The positive sign means that the medium rank coal is water-wet during the drainage process. Similar to the sand experiments (Figure 3.4), the differences in drainage capillary pressure are directly related to the interfacial tension.

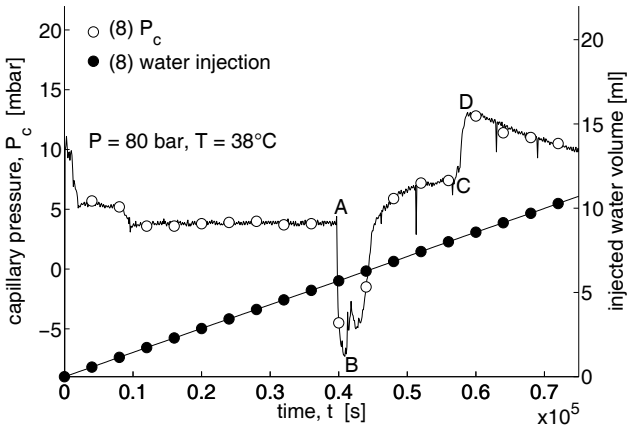

Figure 3.7 History of the capillary pressure and the cumulative water injection for the primary imbibition process with N_2 (experiment 8, water injection rate is 0.5 ml/h). This plot shows the typical behavior of a primary imbibition experiment.

More information is obtained when the CO_2 injection rate is set to zero (experiment 11, points A and B in Figure 3.9). During these equilibration steps at respectively $S_w = 0.82$ and $S_w = 0.38$, the capillary pressure decreases towards zero (see Figure 3.10).

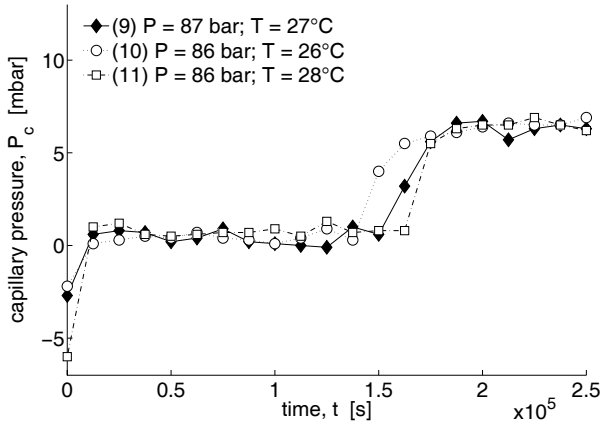

Figure 3.8 History of the capillary pressure for primary drainage in medium rank coal. In all cases the liquid CO_2 injection rate is 0.5 ml/h. These experiments show the reproducibility at high CO_2 pressures in coal.

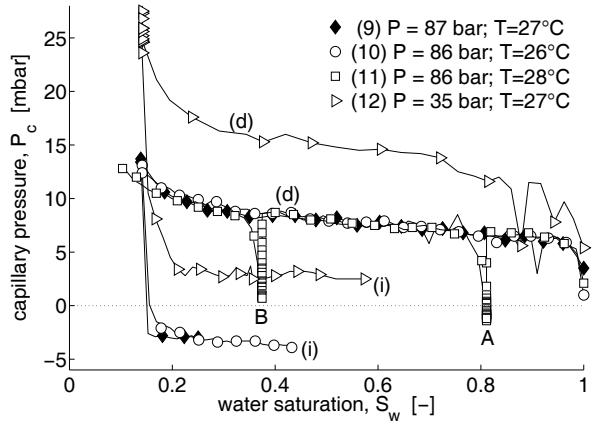

Figure 3.9 Primary drainage (denoted by 'd') and secondary imbibition curves (denoted by 'i') obtained for the medium rank coal. The CO_2 injection rate for experiment 9, 10 and 11 is 0.5 ml/h, and 1 ml/h for experiment 12. The water injection rate during secondary imbibition is 0.5 ml/h in all cases.

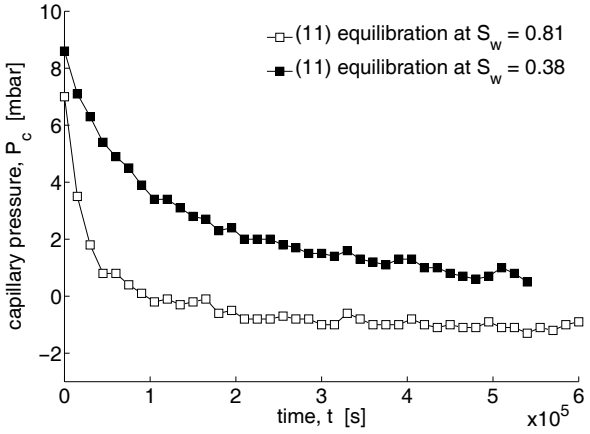

Figure 3.10 Equilibration of P_c during a primary drainage experiment with liquid CO_2 in Warndt-Luisenthal coal (experiment 11) at two different water saturations. Even if the medium rank coal is CO_2-wet, the negative P_c values are only observed after several days.

Because no dynamic or viscous behavior is observed for the capillary pressure during continuous CO_2 injection, the decrease in P_c must be ascribed to another process. A possible explanation for this behavior is that the surface wetting film is ruptured by the presence of the high pressure CO_2 [*Hirasaki*, 1991]. Because the rupture of wetting films can be a slow process, this CO_2-wet behavior will not be necessarily observed in the time frame of our experiments or even in field applications.

The results for the secondary imbibition process for the medium rank coal are shown in Figure 3.9. A decrease of the secondary imbibition capillary pressure from positive to negative values is observed for increasing pressures. Because negative interfacial tensions are excluded [*Chun and Wilkinson*, 1995], this change in sign is ascribed to the wettability alteration from water-wet ($P_c > 0$) to CO_2-wet ($P_c < 0$). The results are in agreement with the pressure dependent wettability of the medium rank coal discussed by *Siemons et al.* [2006b] He measured increasing contact angles for the medium rank coal-CO_2-water system where the cross-over from water-wet to CO_2-wet behavior occurs in the range of 80 to 85 bar.

Comparison of the secondary imbibition curves measured for the medium rank coal and coarse sand (experiment 7, Figure 3.5) shows that the capillary pressure in coal immediately drops to a negative value, indicating that no spontaneous imbibition takes place. This behavior is not observed for the water-wet sand (experiment 7), which shows a gradual decrease of the secondary imbibition capillary pressure.
The wetting alteration of the medium rank coal is also emphasized by the water production behavior. Early water breakthrough is observed for pressures $>$ 85 bar (experiment 9 and 10). No water was produced for the gaseous CO_2 experiment (12), where we abort the imbibition process before the residual gas saturation has been reached. As apposed to the corresponding experiments in coal (experiment 9 and 10), no water breakthrough is observed during the secondary imbibition experiment in the coarse sand (experiment 7, Figure 3.5).
The production and injection curves for the primary drainage in medium rank coal at 35 and 87 bar (experiment 12 and 9) are presented in Figure 3.11. The same conditions as for experiment 9 are applied for experiment 6 (primary drainage in coarse sand, Figure 3.6). Comparison between the water production versus gas injection for experiment 6 and 9, shows that the effect of CO_2 sorption in coal is negligible. Similar to the drainage experiment in coarse sand, the cumulative production and injection curves for coal run parallel.

The deviation in cumulative volumes at the end of the drainage process is $\Delta V = 0.36\,\text{ml}$ and $\Delta V = 1.45\,\text{ml}$ for the sand and the medium rank coal respectively. We also mention that the amount of sorbed CO_2 on the coal is hard to determine, owing to the sorption of CO_2 in the Viton O-rings.
Primary drainage curves for the high rank Selar-Cornish coal at pressures between 85 and 90 bar and temperatures varying from 24 to 36°C are shown in Figure 3.12. In all cases the high rank coal shows water-wet behavior because the $P_c - S_w$ curves are positive. In contrast to the high pressure drainage experiments conducted on the medium rank coal, (see Figure 3.9) the $P_c - S_w$ curves are very irregular, especially when the temperature approaches or becomes higher than the critical temperature of CO_2.

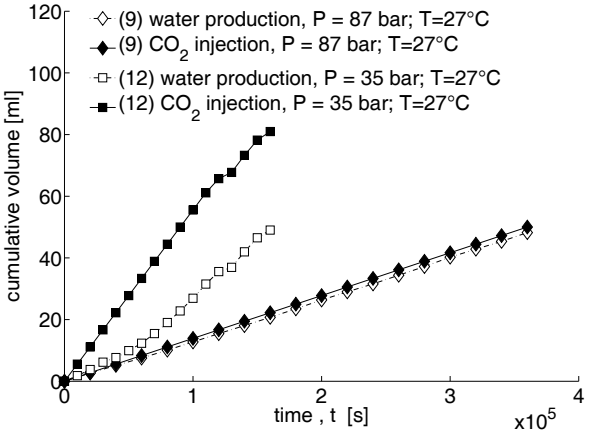

Figure 3.11 Cumulative water production and CO_2 injection for primary drainage experiments with liquid CO_2 in medium rank coal (experiment 9, CO_2 injection rate is 0.5 ml/h) and gaseous CO_2 in medium rank coal (experiment 12, CO_2 injection rate is 1 ml/h). Significant discrepancy between the water production and CO_2 injection is only observed for gaseous CO_2 conditions.

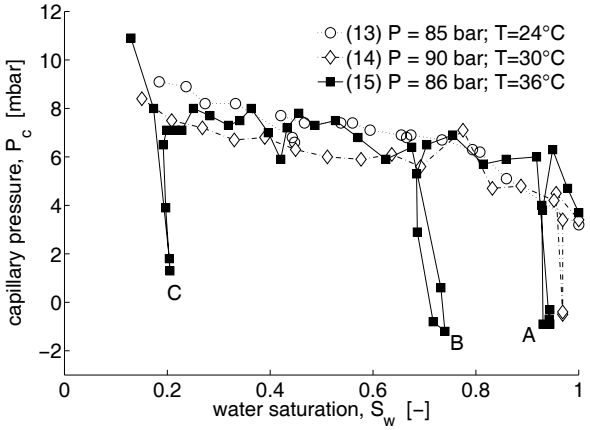

Figure 3.12 Primary drainage capillary pressure curves for CO_2 injection in high rank Selar-Cornish coal. The CO_2 injection rate is 0.5 ml/h in each case. Points A, B and C indicate sudden imbibition events during CO_2 injection.

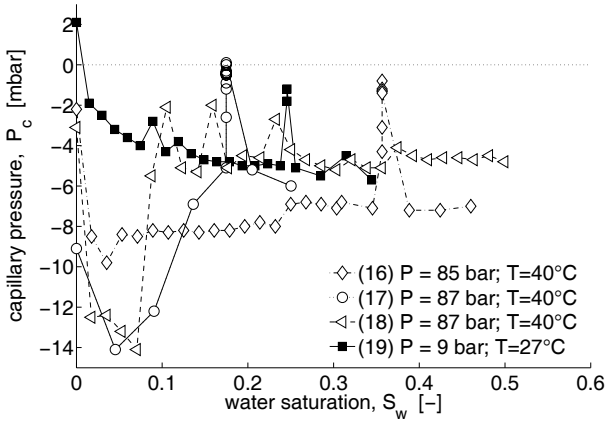

Figure 3.13 Primary imbibition capillary pressure curves in high rank Selar-Cornish coal for supercritical CO_2 (experiment 16,17 and 18) and gaseous CO_2 (experiment 19). The water injection rate is 0.5 ml/h in each case. The reasons for the capillary pressure behavior for $S_w < 0.1$ are not clear.

The imbibition events (denoted by A, B and C, Figure 3.12), occurring in experiment 15, are also observed during the primary drainage with supercritical CO_2 in sand (experiment 7, Figure 3.4).

We have also conducted a series of primary imbibition experiments on the high rank coal and the results are presented in Figure 3.13. Here, the primary imbibition measurement conducted for the sand-N_2-water system (experiment 8, Figure 3.5) is used as a reference to indicate the time when the imbibition process starts. Figure 3.13 plots the primary imbibition curves for the high rank coal. We measure negative capillary pressures for both gaseous CO_2 (9 bar and 27°C) and supercritical CO_2 (from 85 to 87 bar, 40°C). It is clear from Figure 3.13 that the capillary pressure behavior for supercritical CO_2 is also irregular under imbibition conditions, which is caused by sudden drainage events. The average magnitude of the imbibition P_c is approximately minus 8 mbar for experiment 16 and approximately minus 5 mbar for experiment 17, 18 and 19. The capillary pressure in the water saturation range of $0 > S_w < 0.1$ shows a distinct character for experiment 17 and 18. The reasons for this are not yet clear.

For all pressure conditions, the high rank coal shows CO_2-wet behavior during imbibition, which is again emphasized by the fast water breakthrough, occurring at $S_w < 0.5$. On the basis of on the imbibition results of experiment 12 (Figure 3.9) and experiment 19 (Figure 3.13) it is clear that the high rank coal compared to the medium rank coal is CO_2-wet for much lower CO_2 pressures. Our results are in agreement with the findings described by *Siemons et al.* [2006a]. For the high rank coal they found a wetting alteration for system pressures higher than 2.6 bar.
Although we have not measured secondary imbibition curves for the high rank coal, it can be expected that CO_2-wet behavior will also be observed. In general, the wetting behavior with respect to the carbon content and the rank of the coal (see Table 3.1) corresponds to the results obtained by *Gutierrez-Rodriguez et al.* [1984], *Gutierrez-Rodriguez and Aplan* [1984], and *Orumwense* [2001]. It appears that imbibition experiments provide good qualitative information regarding the wettability of coal. This implies that the water saturation history plays an important role for the wetting characteristics of coal.

3.6 Conclusions

- A capillary pressure set-up has been developed and validated that can be used to determine the wettability of the coal-CO_2-water system as a function of the system pressure.
- The interpretation is facilitated by comparison of the sand-CO_2-water and coal-CO_2-water experiments at a range of pressure and temperature conditions. Reproducibility of the experiments is considered good.
- Increasing CO_2 pressures result in decreasing primary drainage capillary pressures for all samples used. This can be explained by the decrease in interfacial tension.
- Both the medium and high rank coal is water-wet during the primary drainage process; this behavior is in contrast with contact angle experiments.
- With increasing system pressures the wettability of the medium rank coal alters from water-wet to CO_2-wet. High rank coal is CO_2-wet during primary imbibition experiments in the entire pressure range. The behavior during imbibition corresponds to contact angle measurement data.
- Fast water breakthrough during the imbibition process indicates CO_2-wet behavior.

- Imbibition tests provide relevant data to evaluate the wetting properties of coal.
- The difference between imbibition and drainage experiments can be explained by the stability of a water layer on the coal. Such a film must be ruptured before the coal becomes CO_2-wet.
- This film rupture may imply that the time scale in laboratory experiments is not [3]representative for field scale behavior.

Bibliography

Anderson, W. G. (1986), Wettability literature survey- Part 2: Wettability measurement, *JPT*, *38 (11)*, 1246-1262, SPE 13933.

Anderson, W. G. (1987), Wettability literature survey - Part 4: Effects of wettability on capillary pressure, *JPT*, 1283–1300, SPE 15271.

Bird, R. B., W. E. N. Steward, and E. Lightfoot (1960), *Transport Phenomena*, John Wiley and Sons, New York.

Chi, S. M. B. I. Morsi, G. E. Klinzing, and S.-H. Chiang (1988), Study of interfacial properties in the liquid CO_2-water-coal system, *Energy & Fuels*, *2*, 141-145.

Christoffersen, K. R., and C. H. Whitson (1995), Gas/oil capillary pressure of chalk at elevated pressures, *SPE Formation Eval.*, *10 (6)*, 153–159, SPE 26673-PA.

Chun, B. -S., and G. T. Wilkinson (1995), Interfacial tension in high-pressure carbon dioxide mixtures, *Ind. Eng. Chem. Res., 34*, 4371–4377.

Dabbous, M. K., A. A. Reznik, B. G. Mody, P. F. Fulton, and J. J. Taber (1976), Gas-water capillary pressure in coal at various overburden pressures,. *SPE Journal*, *16 (5)*, 261-268, SPE 5348.

Gutierrez-Rodriguez, J. A., R. J. Purcell Jr., and F. F. Aplan (1984), Estimating the hydrophobicity of coal, *Colloids. Surf.*, *12*, 1-25.

Gutierrez-Rodriguez, J. A., and F. F. Aplan (1984), The effect of oxygen on the hydrophobicity and floatability of Coal, *Colloids Surf.*, *12*, 27-71.

Hassanizadeh, S. M., M. Celia, and H. K. Dahle (2002), Dynamic effect in the capillary pressure - saturation relationship and its impacts on unsaturated flow, *Vadose Zone Journal*, *1*, 38–57.

Hirasaki, G. J. (1991), Wettability: Fundamentals and Surface Forces, *SPEFE*, *6 (3)*, 217-226, SPE 17367.

Jennings, J. W., D. S. McGregor, and R. A. Morse (1988), Simultaneous determination of capillary pressure and relative permeability by automatic history matching, *SPE Formation Eval.*, *3 (3)*, 322–328.

Keller, D. V. Jr. (1987), The contact angle of water on coal,. *Colloids Surf.*, *22*, 21-35.

[3] Private communication with M. Blunt, CMWR XVI, Copenhagen

Kokkedee, J. A. (1994), Simultaneous determination of capillary pressure and relative permeability of a displaced phase, paper presented at European Petroleum Conference, London, 25-27 October, 213–222.

Kumar, A., R. Ozah, M. Noh, G. A. Pope, S. Bryant, K. Sepehrnoori, and L. W. Lake (2005), Reservoir simulation of CO_2 storage in deep saline aquifers, *SPE J., 10 (3)*, 336–348, SPE 89343-PA.

Longeron, D., W. L. Hammervold, and S. M. Skjaeveland (1995), Water-oil capillary pressure and wettability measurements using micropore membrane technique, paper presented at International Meeting on Petroleum Engineering, Beijing, 14-17 November, pp. 543–553, SPE 30006.

Mavor, M. J., W. D. Gunter, and J. R. Robinson (2004), Alberta multiwell micro-pilot testing for CBM properties, Enhanced Methane Recovery and CO_2 storage potential, paper SPE 90256 presented at the 2004 SPE Annual Technical Conference and Exhibition, Houston, Texas, 26-29 September.

Mazumder, S., W.-J. Plug, and J. Bruining (2003), Capillary pressure and wettability behavior of coal-water-carbon dioxide system, paper presented at SPE Annual Technical Conference and Exhibition, Denver, Co., 5-8 October, SPE 84339.

Mazumder, S., A. Karnik, and K. H. Wolf (2006), Swelling of coal in response to CO_2 sequestration for ECBM and its effect on fracture permeability, *SPE Journal*, *11 (3)*, 390-398, SPE 97754.

Murata, T. (1981), Wettability of coal estimated from the contact angle, *Fuel*, *60*, 744-746.

Newsham, K. E., J. A. Rushing, P. M. Lasswell, J. C. Cox, and T. A. Blasingame (2004), Comparative study of laboratory techniques for measuring capillary pressures in tight gas sands, paper presented at SPE Annual Technical Conference and Exhibition, Houston, Texas, 26-29 September, SPE 89866.

Orr, F. M. Jr. (2004), Storage of carbon dioxide in geologic formations, *JPT*, *56 (9)*, 90-97, SPE 88842.

Orumwense, F. F. O. (2001), Wettability of coal - a comparative study, *Scandinavian J. of Metallurgy*, *30*, 204-211.

Pagnier, H. J. M., F. van Bergen, E. Kreft, L. G. H. van der Meer, and H. J. Simmelink (2005), Field experiment of ECBM-CO_2 in the upper silesian basin of poland (RECOPOL), paper SPE 94079 presented at the 2005 SPE Europec/EAGE Annual Conference, Madrid, Spain, 13-16 June.

Pawar, R. J., N. R. Warpinski, R. D. Benson, R. B. Grigg, J. L. Krumhansl, and B. A. Stubbs (2004), Geologic sequestration of CO_2 in a depleted oil reservoir: an overview of a field demonstration project, paper SPE 90936 presented at the 2004 SPE Annual Technical Conference and Exhibition, Houston, Texas, 26-29 September.

Plug, W.-J., S. Mazumder, J. Bruining, N. Siemons, and K. Wolf (2006), Capillary pressure and wettability behavior of the coal-water-carbon dioxide system at high pressures, paper presented at 2006 Int. CBM Symposium, Tuscaloosa, Al., 22-26 May.

Pruess, K., T. Xu, and J. Garcia (2003), Numerical modeling of aquifer disposal of CO_2, *SPE Journal, 8 (1)*, 49-60, SPE 83695.

Pruess, K. (2004), Numerical simulation of CO_2 leakage from a geologic disposal reservoir, including transitions from super- to subcritical conditions, and Boiling of Liquid CO_2, *SPE Journal, 9 (2)*, 237-248, SPE 86098

Reeves, S. R. (2001), Geological sequestration of CO_2 in deep, unmineable coalbeds: An integrated research and commercial-scale field demonstration project, paper SPE 71749 presented at the 2001 SPE Annual Technical Conference and Exhibition, New Orleans, Louisiana, 30 September-3 October.

Reucroft, P. J. and A. R. Sethuraman (1987), Effect of pressure on carbon dioxide induced coal swelling, *Energy and Fuels*, *1*, 72-75.

Siemons N., A. Busch, J. Bruining, B. Krooss, and Y. Gensterblum (2003), Assessing the kinetics and capacity of gas adsorption in coals by a combined adsorption/diffusion method, paper SPE 84340 presented at the 2003 SPE Annual Technical Conference and Exhibition, Denver, Colorado, 5-8 October.

Siemons, N., J. Bruining, H. Castelijns, and K. Wolf (2006a), Pressure dependence of the contact angle in a CO_2-H_2O-coal system, *J. Colloid. Sci., 297 (2)*, 755–761.

Siemons, N., J. Bruining, K. Wolf, and W. J. Plug (2006b), Pressure dependence of the CO_2 contact angle on bituminous coal and semi-anthracite in water, paper presented at 2006 Int. CBM Symposium, Tuscaloosa, Al., 22-26 May.

Shtepani, E. (2006), CO_2 Sequestration in Depleted Gas/Condensate Reservoirs, paper SPE 102284 presented at the 2006 SPE Annual Technical Conference and Exhibition, San Antonio, Texas, USA, 24-27 September.

Wiebe, R., and V. L. Gaddy (1940), The solubility of carbon dioxide in water at various temperatures from 12 to 400°C and at pressures to 500 atmospheres. Critical phenomena, *J. Am. Chem. Soc., 62*, 815–817.

Wildenschild, D., J. W. Hopmans, and J. Simunek (2001), Flow rate dependence of soil hydraulic characteristics, *Soil Sci. Soc. Am. J.*, *65*, 35–48.

Chapter 4 Simultaneous measurement of hysteresis in capillary pressure and electric permittivity[4]

4.1 Introduction

Capillary pressure, P_c, versus water saturation, S_w, relationships are used in subsurface flow engineering applications such as hydrocarbon production [*Delshad et al.*, 2003], soil remediation [*Dane et al.*, 1998] and carbon dioxide (CO_2) sequestration [*Plug et al.*, 2006]. Hysteresis between the drainage (decreasing S_w) and imbibition (increasing S_w) of capillary pressure is widely observed and extensively investigated [*Morrow*, 1970; *Hassanizadeh and Gray*, 1993; *Reeves and Celia*, 1996]. This saturation history dependence of P_c is related to contact angle hysteresis [*Anderson*, 1986], irreversible pore-scale fluid redistributions [*Morrow*, 1970], and the interfacial area [*Reeves and Celia*, 1996; *Cheng et al.*, 2004]. As P_c is an interfacial property and strongly relates to the pressure and saturation induced movement and distribution of the phases, the interfacial area per unit volume can be used as an indicator of the thermodynamic energy state [*Cheng et al.*, 2004]. This results in a uniquely defined relationship for P_c as a function of S_w and interfacial area. Furthermore, the initial state of a flow process is involved [*van Kats and Van Duijn*, 2001]. Because all these phenomena also contribute to the complex permittivity of porous fluid-bearing rocks, simultaneous measurements of capillary pressure and permittivity may reveal the fundamental physical behavior of capillary pressure hysteresis.

It is known that the complex permittivity may be a function of the frequency, f. *Chelidze and Gueguen* [1999] distinguished two polarization mechanisms. At frequencies below 10 MHz relaxation processes are exhibited as a result of clustering of components and induced polarization, occurring at the solid-fluid interface [*Chelidze and Gueguen*, 1999] and the interface between the wetting and non-wetting phase [*Knight*, 1991].

---

[4] This chapter is published in Geophysics Letters, Vol. 72, Issue 3, pp. A41-A45; doi: 10.1190/1.2714684

The effects of the pore scale fluid distribution on the electrical behavior during imbibition and drainage results in hysteresis [*Chelidze et al.*, 1999]. Pronounced hysteresis in resistivity is observed by *Fleury and Longeron* [1998], *Knight* [1991], *Elashahab et al.* [1995], and *Moss et al.* [1999] and can be explained by the percolation theory [*Chelidze et al.*, 1999]. *Nguyen et al.* [1999a] reported on hysteresis of the real part of the permittivity. The change in electrical response as function of the rock's wettability has been investigated and described by *Knight and Abad* [1995], *Elashahab et al.* [1995], *Moss et al.* [1999], and *Nguyen et al.* [1999b].
We conclude that different mechanisms are responsible for both the capillary pressure and the complex permittivity behavior. Different studies on combined capillary pressure and electrical resistivity measurements are reported [*Elashahab et al.*, 1995; *Fleury and Longeron*, 1998; *Moss et al.*, 1999]. The real part of the permittivity and capillary pressures were measured simultaneously at frequencies above 100 MHz by *Nguyen et al.* [1999a].

In this study we investigate the capillary pressure and electric behavior for the unconsolidated sand - distilled water - gas system during main drainage and main imbibition. The experiments are conducted at 8 bar pressure and a temperature between 27°C and 28°C. We have performed these experiments in the framework of the investigation of capillary pressure behavior during CO_2 sequestration applications. The capillary pressure is measured under quasi-static conditions using the setup discussed by *Plug et al.* [2006]. The sample holder is designed as a parallel plate capacitor [*Knight and Nur*, 1987; *Shen et al.*, 1987], where two stainless steel end-pieces act as electrodes, and different frequencies can be applied (1 kHz - 3 MHz). The advantage of this technique over (coaxial) transmission line methods is that the sample remains intact during the measurements, which is also the case for the coaxial waveguide method [*Taherian et al.*, 1991]. Calibration of the impedance tool is done using substances with known complex permittivity values [*Shen et al.*, 1987; *Nguyen et al.*, 1999c] and shows a maximum error of 4.5% in the real part. Furthermore the experimental technique is validated with reproducible data and a precision of 93.5% is found. Hysteresis in capillary pressure and electric permittivity is observed between drainage and imbibition at $f = 3$ MHz, and becomes more pronounced at higher water saturations.

Comparison of the data with the Complex Refractive Index model shows the reasonable prediction for the water saturation. Finally, we suggest that a better description of the capillary pressure hysteresis can be obtained from accurate permittivity data than from water saturation alone.

4.2 Experimental method and materials

The experimental setup is based on the porous plate technique [*Plug et al.*, 2006]. We apply quasi-static conditions [*Wildenschild et al.*, 2001], i.e. small injection rates, so that viscous forces can be neglected. A schematic overview of the experimental setup is shown in Figure 4.1 (see Appendix D for photos of the set-up). Two syringe pumps are used and can be set to a constant injection rate or a constant pressure. The gas and the water phases are injected or produced at the top and the bottom of the sample holder respectively. The pressure difference between the gas and the water phases is measured by a pressure difference transducer (PDT, accuracy ± 0.05 mbar), which is located at the same height as the middle of the sample. A temperature control system is used to maintain a constant temperature.

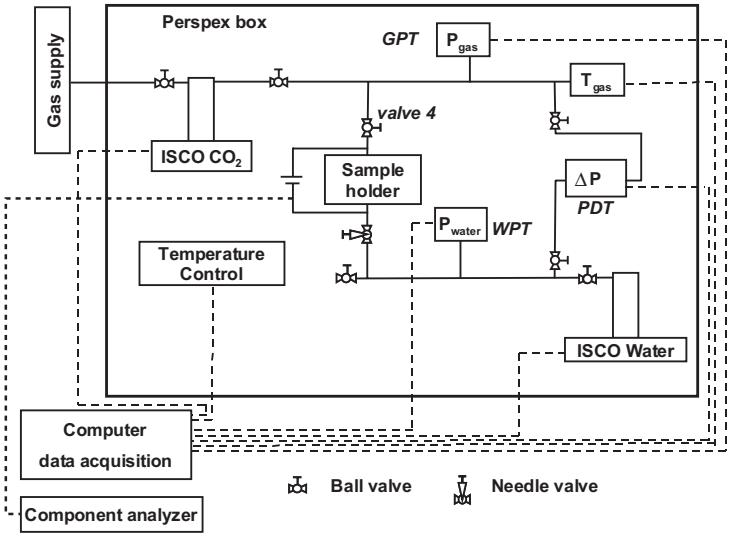

Figure 4.1 Schematic layout of the experimental set up. PDT: pressure difference transducer; GPT: gas pressure transducer; WPT: water pressure transducer.

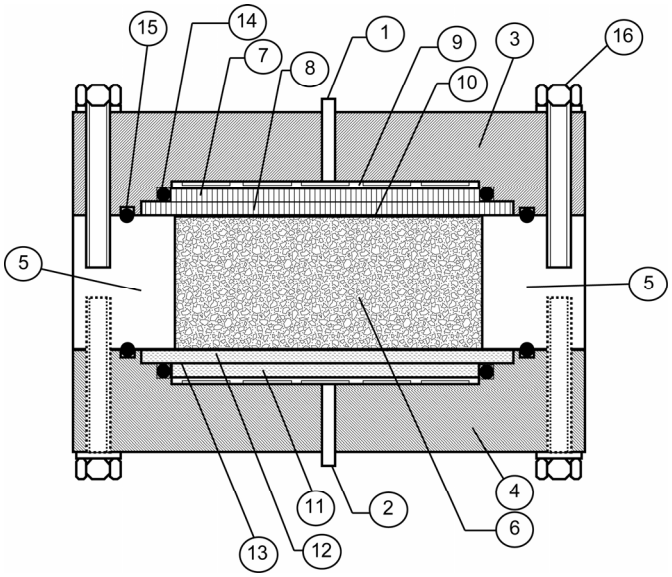

Figure 4.2 The sample-holder: 1. Gas-inlet; 2. Water-inlet; 3. Stainless steel end piece 1; 4. Stainless steel end piece 2; 5. PEEK ring; 6. Porous medium (diameter is 84 mm, height is 27 mm); 7. Perforated plate (diameter is 84 mm); 8. Perforated plate (diameter is 90 mm); 9. Concentric grooves; 10. Nylon filter (pore size 210 μm); 11. SIPERM plate (diameter is 84 mm); 12. SIPERM plate (diameter is 90 mm); 13. Water-wet filter (pore size 0.1 μm); 14. O-rings (2.1 mm); 15. O-rings (4 mm); 16. Stainless steel bolts.

The sample holder, (see Figures 4.2 and 4.3), consists of 3 parts: a PEEK (Polyetheretherketone) ring, which contains the sand sample, and two stainless steel end-pieces. Two porous plates (SIPERM *R*, Cr-Steel basis), with a permeability of $2\times10^{-12}\,\mathrm{m}^2$ and a porosity of 0.32, support the sample and protect the hydrophilic membrane. Two stainless steel plates, both with 32 perforations ($D_p = 5$ mm), are used at the top directly above the sample in combination with a nylon filter. Concentric flow grooves in the end-pieces redistribute the phases over the sample area to avoid preferential flow. The different parts of the sample holder are mounted together with 4 stainless steel bolts at both the top and bottom.

To obtain the permittivity of the sample inside the PEEK ring, a precision component analyzer (Wayne-Kerr, 6640A) is connected to the sample holder

(Figure 4.1). The electrodes are the two end pieces of the sample holder, including the support plates. The PEEK material is non-conductive and hence the sample holder acts as a parallel plate capacitor. The impedance amplitude, $|Z|$ [Ω], and the phase angle, θ [rad], are measured as a function of the frequency and are directly related to the effective complex permittivity (ε_s^*) of the sample, defined by $\varepsilon_s^* = \varepsilon'_s - i\varepsilon''_s$. Here ε'_s and ε''_s represent the real and imaginary part of the permittivity respectively. In this study we are interested in ε'_s and the results are presented as a function of S_w.

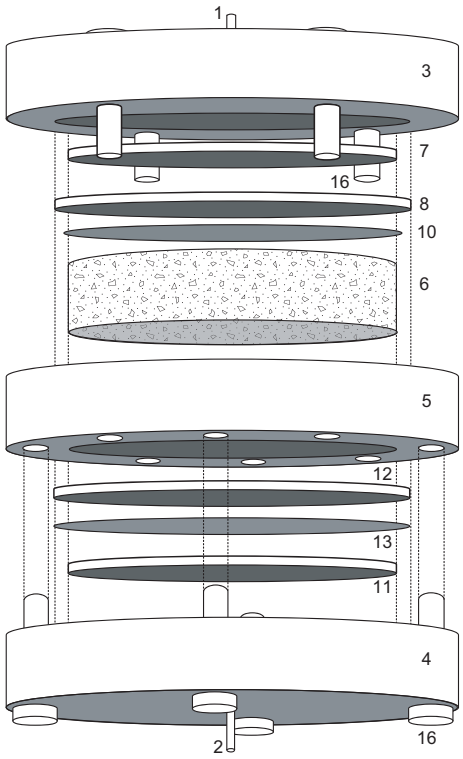

Figure 4.3 Three dimensional representation of the sample holder (not in scale). The numbers correspond to the legend of Figure 4.2. For visualization reasons, the rubber O-rings and the concentric grooves are not shown.

4.3 Data analysis

We define the capillary pressure as the difference in gas and water bulk phase pressures. From the produced water volume we obtain the water saturation. The complex capacitance, C^* [F], is inversely proportional to the complex impedance Z^* [Ω] by $C^* = (i\omega Z^*)^{-1}$, where ω is the angular frequency, defined by $\omega = 2\pi f$ and $Z^* = |Z|\exp(i\theta)$. The derivation of these expressions is given in Appendix C. The capacitor configuration results in a parallel circuit for which C^* is considered as the sum of the capacitance of the sample (C_s^*), the PEEK ring (C_{PEEK}^*), the cables (C_{cables}^*), the electrodes design ($C_{electrodes}^*$) and the background noise (C_{noise}^*). Under the assumption that only C_s^* is changing for different samples, C^* can be written as

$$C^* = C_s^* + C_{residual}^* = \frac{\varepsilon_0 \varepsilon_s^* A_s}{H} + C_{residual}^* \tag{4.1}$$

Here ε_0 is the permittivity of free space, ε_s^* is the permittivity of the sample, $C_{residual}^*$ [F] is the capacitance of the residual contributions and H [m] and A_s [m^2] are respectively the height and the cross-sectional area of the sample. We use the Complex Refractive Index (CRI) model [*Roth et al.*, 1990; *Seleznev et al.*, 2004] to evaluate the effective permittivity of the grain-water-gas mixture, given by

$$\varepsilon'_s = \left[\varphi S_w \sqrt{\varepsilon'_w} + \varphi(1 - S_w)\sqrt{\varepsilon'_{gas}} + (1-\varphi)\sqrt{\varepsilon'_{grain}}\right]^2 \tag{4.2}$$

where φ is the porosity and ε'_w, ε'_{gas} and ε'_{grain} are the water, gas and porous medium permittivity respectively (see also Appendix C). Furthermore, the Hashin-Shtrikman bounds [*Hashin and Shtrikman*, 1962] are used to investigate the validity of the results. The Hashin-Shtrikman bounds put limits on the effective electric permittivity of locally non-interacting and macroscopically homogeneous, isotropic mixtures. Our sand samples satisfy these conditions.

4.4 Calibration and system accuracy

To obtain the most accurate data for the permittivity and the capillary pressure, different configurations of the sample holder are investigated. It appears that the type and combination of the support plates, and the presence and number of the stainless steel bolts do not influence the impedance measurements.

The value for $C^*_{residual}$ (Eq. 4.1) is obtained from air measurements, using $\varepsilon'_s = 1$. The capacitance C^*, of the air-filled sample holder is measured in the range of $20 - 21 \pm 0.05$ pF for the frequency range of 1 kHz to 3 MHz. A statistical analysis on 50 measurements [*Gorriti and Slob*, 2005], for air and 6 different calibration materials, (see Table 4.1), is performed to determine the maximum measurement accuracy. It appears that the measurements are very stable. The mean and the relative error for both $|Z|$ and θ of ten groups of two air measurements are of the order of 0.1% (see Figure 4.4). A more detailed description for this analysis is given in Appendix C.

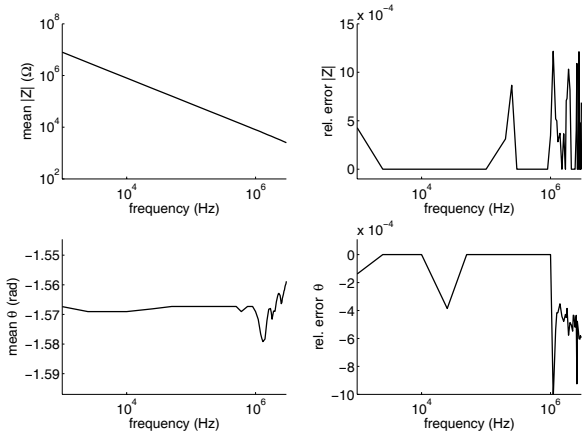

Figure 4.4 The mean and relative error for 10 groups of 2 air measurements for the impedance amplitude $|Z|$ and the phase angle θ [rad]. The straight line and the average phase angle of approximately $\theta = -\pi / 2$ indicate that no loss terms are measured.

The impedance tool is calibrated for $f = 3$ MHz using materials with known permittivity behavior within the range of $2 - 25$ [-]. In Table 4.1 we present the theoretical permittivity, $\varepsilon'_{s,theory}$, the measured permittivity and the absolute errors,

$\Delta\varepsilon'_s$, obtained from an error analysis, and the accuracy of the 50 measurements for each calibration sample. High accuracy and good agreement is found for a wide range of permittivity values.

4.5 Sample preparation and experimental procedure

We investigate the capillary pressure and complex permittivity behavior of the unconsolidated sand-water-gas (CO_2/N_2) system. For each experiment a new sand pack is used. The average grain size fraction is $360-410$ μm and the porosity is obtained with helium at room temperature. For all samples, the porosity varies from $0.37-0.38\pm0.005$.

After the porosity measurements, the total system is evacuated for 1 hour. Subsequently, the sample holder is filled with distilled water (no salinity) at a pressure of approximately 8 bar to dissolve small air bubbles. Valve 4 (see Figure 4.1) is closed and the gas tubing and pump are filled with gas. The gas booster is used to bring up the gas pressure. We set a constant temperature and let the system equilibrate for two days. When the water and gas pressures are equal, a constant water refill rate is applied, the gas pump is set to a constant pressure and valve 4 is opened. After the main drainage process, the main imbibition process starts when the water pump is set to a constant injection rate.

Sample	$\varepsilon'_{s,theory}$	$\varepsilon'_s \pm \Delta\varepsilon'_s$	Accuracy of ε'_s
Teflon	2. (1 MHz)	2.06 ± 0.03	99.5%
Perspex	2.76 (1 MHz)	2.84 ± 0.04	98.9%
PVC	3.3 (1 MHz)	3.32 ± 0.04	99.3%
1-Decanol (99%)	8.1 (static)	8.49 ± 0.05	99.8%
1-Butanol	17.8 (static)	18.32 ± 0.06	99.9
Ethanol (100%)	24.3 (static)	24.64 ± 0.07	99.8

Table 4.1 Theoretical and measured permittivity values and their corresponding error and accuracy for the calibration samples at $f=3$ MHz and 25°C. The theoretical values are obtained from *Weast and Astle* [1981].

4.6 Results and discussion

Figure 4.5 shows the capillary pressure as a function of the water saturation for the CO_2-water-sand and the N_2-water-sand systems. Both of the CO_2 experiments are performed at 8 bar and 28°C and show good reproducibility.

The relative error for the water saturation calculation is $\pm 12\,\%$ for $S_w = 0.1$ and decreases towards zero for $S_w = 1$. For visualization reasons, the error bars for S_w are not shown in Figure 4.5. High precision in capillary pressure is obtained for the saturation range between 0.15 and 0.72. As a result of a power failure at A (Figure 4.5), the primary drainage data are missing near $S_w = 0.9$ for experiment 2.

The nonmonotonic behavior of the imbibition curve, observed at point B (experiment 1), is attributed to summer temperatures in the laboratory that exceeded the upper limit of the temperature control system. Capillary pressure hysteresis is measured and is similar for both experiments. The experiment with nitrogen (N_2) is conducted at 8 bar and a temperature of 27°C is applied. Both the drainage and imbibition curves are slightly higher than those for CO_2 for $S_w < 0.6$ and a higher residual gas saturation ($S_{gr} = 0.21$) is obtained. The difference in residual gas saturation is explained by higher dissolution of CO_2 in water.

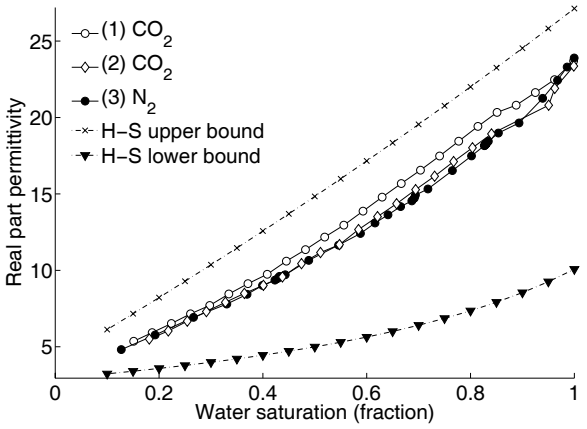

Figure 4.5 Main drainage and imbibition capillary pressure curves for CO_2 and N_2 for a flow rate of 0.5 ml/h. The curves for CO_2 coincide, which clarifies the reproducibility of the method. All experiments are conducted for pressures of 8 bar and a temperature of 27°C and 28°C for respectively CO_2 and N_2. The corresponding permittivity as function of the water saturation is shown in Figures 4.6 and 4.7.

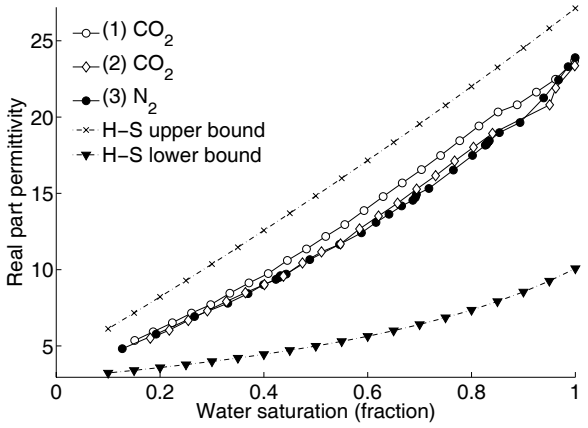

Figure 4.6 The corresponding real part of the permittivity, ε'_s, as function of S_w for the main drainage experiments are shown in as well as the Hashin-Shtrikman upper and lower bounds. All experiments are conducted for pressures of 8 bar and a temperature of 27°C and 28°C for respectively CO_2 and N_2.

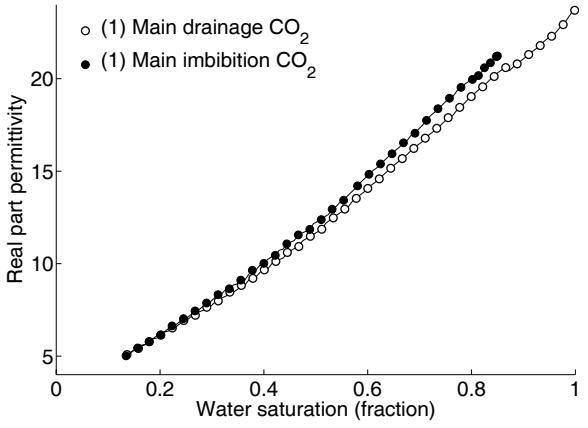

Figure 4.7 The real part of the permittivity for experiment 1 (CO_2-distilled water-sand), for both the main drainage and imbibition process. The hysteresis in permittivity is visible.

In Figure 4.6, ε'_s as function of S_w for the main drainage processes is shown for $f = 3$ MHz. The measurement data can be fitted with the CRI model (Eq. 4.2) using $\varepsilon'_w = 80$, $\varepsilon'_{grain} = 6$, and $\varepsilon'_{gas} = 1$ for water, grains and CO_2/N_2 respectively. This indicates that S_w is predicted reasonably from the measurements. Because the sample porosities are between 0.37 and 0.38, the porosity used in CRI is $\varphi = 0.375$. From Figure 4.6 it is clear that the measured effective permittivity satisfy the Hashin-Shtrikman bounds. This implies that for $f = 3$ MHz the system can be considered to be a macroscopically homogeneous and isotropic mixture.

From the drainage data of the two CO_2 experiments (Figure 4.6) we obtain the reproducibility of the permittivity measurements. A precision of 93.5% is determined for the water saturation range of $0.15 < S_w < 0.72$, which is lower than the precision for the P_c curves. This is caused by difference in sand packs.
Figure 4.7 plots ε'_s for the main drainage and imbibition processes for the first CO_2 experiment. The same input parameters for the CRI model used for the drainage process, result in good agreement for imbibition. It is clear that the Hashin-Shtrikman bounds are still satisfied for imbibition. Comparison between the curves in Figure 4.7 shows that ε'_s for imbibition is higher than for drainage. Similar to the capillary pressure hysteresis, the permittivity hysteresis increases for increasing water saturation.
Near $S_w = 0.85$ the slope of ε'_s in each drainage experiment shows an abrupt change (Figure 4.6). As a result of spontaneous redistribution of the phases, and percolation mechanisms, the system undergoes a transition from trapped gas to trapped water [*Knight*, 1991; *Chelidze et al.*, 1999]. The clear dip in drainage P_c at $S_w = 0.85$ for experiment 3 supports this explanation. Similar permittivity behavior is also observed for the imbibition process near $S_w = 0.8$ (see Figure 4.7).
Reasons for the permittivity hysteresis can be found in the distribution of the water and gas phase [*Chelidze et al.*, 1999] as well as the change in interfacial area during drainage and imbibition. The first effect mentioned is observed in this study, the latter effect is expected to be more pronounced for lower frequencies. Different mechanisms, such as dipole polarization, polarization in the electrical double layer [*Chelidze et al.*, 1999] and conduction on the water-gas interface [*Knight*, 1991], are therefore considered to be the key to improve the current

knowledge of capillary hysteresis as function of the interfacial area, especially when pronounced permittivity hysteresis is observed at high water contents. The low frequency results will be discussed in Chapter 5.

4.7 Conclusions

The measurements presented in this work show that it is possible to measure the capillary pressure and the permittivity properties simultaneously with a non-destructive technique. The tool is widely applicable and can be used for fluid-bearing rocks and soils, and the results are, therefore, relevant for applications in near-surface, as well as exploration and production geophysics. Moreover, the experimentally observed hysteresis in the real part of the complex electric permittivity, provides evidence that a better description of the capillary pressure hysteresis can be obtained than that from water saturation alone. Because the presence of water plays a dominant role in the permittivity behavior, low frequency measurements are necessary to assist in the interpretation of the permittivity hysteresis in terms of interfacial activities.

Bibliography

Anderson, W. G. (1986), Wettability literature survey- part 2: Wettability measurement, *Journal of Petroleum Technology*, 1246-1262.

Chelidze, T. L., and Y. Gueguen (1999), Electrical spectroscopy of porous rocks: a review –I. Theoretical model, *Geophysical Journal International*, *137*, 1-15.

Chelidze, T. L., Y. Gueguen, and C. Ruffet (1999), Electrical spectroscopy of porous rocks: a review –II. Experimental results and interpretation, *Geophysical Journal International*, *137*, 16-34.

Cheng, J.-T., L. J. Pyrak-Nolte, D. D. Nolte, and N. J. Giordano (2004), Linking pressure and saturation through interfacial areas in porous media, *Geophysical Research Letters*, *31,* L08502, doi:10.1029/2003GL019282.

Dane, J. H., C. Hofstee, and A. T. Corey (1998), Simultaneous measurement of capillary pressure, saturation, and effective permeability of immiscible liquids in porous media, *Water Resources Research*, *34*, 3687-3692.

Delshad, M., R. J. Lenhard, M. Oostrom, and G. A. Pope (2003), A mixed-wet hysteretic relative permeability and capillary pressure model for reservoir simulations, *SPE Reservoir Evaluation and Engineering*, *6*, 328-334.

Elashahab, B. M., X. D. Jing, and J. S. Archer (1995), Resistivity index and capillary pressure hysteresis for rock samples of different wettability characteristics, SPE Middle East Oil Show, paper no. 29888.

Fleury, M., and D. Longeron (1998), Combined resistivity and capillary pressure measurements using micropore membrane technique, *Journal of Petroleum Science and Engineering*, *19*, 73-79.

Gorriti, A. G. and E. C. Slob (2005), A new tool for accurate S-parameters measurements and permittivity reconstruction, *IEEE Transactions on Geoscience and Remote Sensing*, *43*, 1727-1735.

Hashin, Z, and S. Shtrikman (1962), A variational approach to the theory of the effective magnetic permeability of multiphase materials, *Journal of Applied Physics*, *33*, 3125-3131.

Hassanizadeh, S. M., and W. G. Gray (1993), Thermodynamic basis of capillary pressure in porous media, *Water Resources Research*, *29*, 3389-3405.

van Kats, F. M., and C. J. van Duijn (2001), A mathematical model for hysteretic two-phase flow in porous media, *Transport in Porous Media*, *43*, 239-263.

Knight, R. J., and A. Nur (1987), The dielectric constant of sandstones, 60 kHz to 4 MHz, *Geophysics*, *52*, 644-654.

Knight, R. (1991), Hysteresis in the electrical resistivity of partially saturated sandstones, *Geophysics*, *56*, 2139-2147.

Knight, R., and A. Abad (1995), Rock/water interaction in dielectric properties: Experiments with hydrophobic sandstones, *Geophysics*, *60*, 431-436.

Morrow, N. (1970), Physics ad thermodynamics of capillary action in porous media, *Industrial and Engineering Chemistry*, *62*, 32-56.

Moss, A. K., X. D. Jing, and J. S. Archer (1999), Laboratory investigation of wettability and hysteresis effects on resistivity index and capillary pressure characteristics, *Journal of Petroleum Science and Engineering*, *24*, 231-242.

Ngyuen, B.- L., J. Bruining, and E. C. Slob (1999a), Hysteresis in dielectric properties of fluid-saturated porous media, SPE Asia Pacific Improved Oil Recovery Conference, paper no. 57305.

Ngyuen, B.- L., J. Bruining, and E. C. Slob (1999b), Effects of wettability on dielectric properties of porous media, SPE Annual Technical Conference and Exhibition, paper no. 56507.

Nguyen, B.- L, A. M. Geels, J. Bruining, and E. C. Slob (1999c), Calibration measurements of dielectric properties of porous media, *SPE Journal*, *4*, 353-359.

Plug, W.J., S. Mazumder, J. Bruining, K.H.A.A. Wolf, and N. Siemons (2006), Capillary pressure and wettability behavior of the coal - water - carbon dioxide system at high pressures, International CBM Symposium, paper no. 606.

Reeves, P. C., and M. A. Celia (1996), A functional relationship between capillary pressure, saturation and interfacial area as revealed by a pore-scale network model, *Water Resources Research*, *32*, 2345–2358.

Roth, K., R. Schulin, H. Flühler, and W. Attinger (1990), Calibration of time domain reflectometry for water content measurement using a composite dielectric approach, *Water Resources Research*, *26*, 2267-2273.

Seleznev, N., A. Boyd, T. Habashy, and S. Luthi (2004), Dielectric mixing laws for fully and partially saturated carbonate rocks, Proceedings of the SPWLA 45th Annual Symposium, paper CCC.

Shen, L. C., H. Marouni, Y. Zhang, and X. Shi (1987), Analysis of the parallel-disk sample holder for dielectric permittivity measurement, *IEEE Transactions on Geoscience and Remote Sensing*, *25*, 534-539.

Taherian, M. R., D. J. Yuen, T. L. Habashy, and J. A. Kong (1991), A coaxial-circular waveguide for dielectric measurement, *IEEE Transactions on Geoscience and Remote Sensing*, *29*, 321-329.

Wildenschild, D., J. Hopmans, and J. Simunek (2001), Flow rate dependence of soil hydraulic characteristics, *Soil Science Society of America Journal*, *65*, 35-48.

Weast, R. C., and M. J. Astle (1981), *CRC Handbook of Chemistry and Physics,* 62nd ed., CRC Press., Boca Raton, Florida.

Chapter 5 Capillary pressure as a unique function of electric permittivity and water saturation[5]

5.1 Introduction

Capillary pressure (P_c) plays an important role in geosciences, e.g., hydrocarbon recovery, vadose zone hydrology, carbon dioxide sequestration, and soil remediation techniques. However, one may also think on porous tissue applications of biology and bioengineering. One of the key issues concerning capillary pressure is the non-uniqueness between the drainage (decreasing water saturation) and imbibition (increasing water saturation) processes on a continuum scale, the so-called capillary hysteresis. This non-uniqueness makes it difficult to predict the distributions of multiple fluids in a porous medium and the state of the system. Therefore, capillary pressure hysteresis is important in production environments using alternating water/gas injection processes known as WAG (Water Alternating Gas). Also the movement of oil in a heterogeneous reservoir and the success of soil remediation will be characterized by a sequence of drainage and imbibition events. From thermodynamic considerations it can be shown that P_c is the surface free-energy change that occurs when a unit of non-wetting fluid phase is injected or produced [*Morrow*, 1970; *Gray and Hassanizadeh*, 1993]. This macro-scale P_c is defined as the exterior pressure difference between the two phases, which depends on the interior water saturation (S_w). To get a better understanding of the capillary pressure behavior, we have investigated the capillary pressure and its relation to both S_w and the complex permittivity, ε_s^*.

It has been suggested that P_c can be defined uniquely by S_w and the interfacial area [*Reeves and Celia*, 1996; *Held and Celia*, 2001; *Cheng et al.*, 2004]. In general a distinction is made between the capillary dominated interface between the wetting and non-wetting phase, a_{wn} , and the interface between the wetting and solid phase, a_{ws} [*Cheng et al.*, 2004]. In principle a_{wn} can be measured with interfacial tracers [*Dalla et al.*, 2002] and with micro-models [*Cheng et al.*, 2004]. However, these experiments are complicated and time-consuming. Theoretical and computational

[5] This chapter is published in Geophys. Res. Lett., 34, L13306, doi:10.1029/2007GL029674.

approaches, e.g. pore-scale network models, are also used to estimate a_{wn} [*Reeves and Celia*, 1996; *Held and Celia*, 2001]. In general, the functional relation between P_c, a_{wn} and S_w follows a general trend, is smooth and has a convex non-monotonic shape [*Gray and Hassanizadeh*, 1993; *Held and Celia*, 2001].

We propose that the electric permittivity provides new insight in the understanding of the fundamentals and physical behavior of capillary pressure as function of the interfacial area. Examples of permittivity behavior in porous media can be found in the work of *Knight and Nur* [1987], *Ruffet et al.* [1991], *Knight* [1991], *Knight and Abad* [1995], *Robert and Lin*, [1997], *Chelidze and Gueguen* [1999], *Chelidze et al.* [1999], *Seleznev et al.* [2004] and *Plug et al.* [2007]. All these authors reported on the permittivity response in the frequency range, from 1 to 14 MHz. In a previous paper [*Plug et al.*, 2007] we presented a novel set-up with which we can measure P_c and ε_s^* simultaneously as function of S_w for gas-water systems. We showed that a small hysteresis in the real part of the electric permittivity was observed for 3 MHz. As interfacial contributions of thin water layers play a minor role at these frequencies we have attributed the hysteresis to a different distribution of the phases in the porous medium. It has been suggested in the literature that at lower frequencies, below 1 MHz, other mechanisms also contribute, such as ionic transport, polarization of the electrical double layer [*Chelidze et al.*, 1999; *Ulrich and Slater*, 2004] and conduction by surfactants adsorbed at the water-gas interface [*Knight*, 1991]. These mechanisms have in common that their contribution to the electric permittivity is caused by *interfacial* phenomena. Therefore, if it is possible to show experimentally that the capillary pressure is a unique function of water saturation and electric permittivity this would support the idea that the capillary pressure is a unique function of water saturation and interfacial area.

For this reason we present the experimental results from combined measurements of capillary pressure and the complex permittivity at 100 kHz as a function of S_w, using the set-up discussed by *Plug et al.* [2007]. The experiments were conducted for the sand-distilled water-gas (CO_2/N_2) systems at various fluid pressures (1-13 bar). We measured primary drainage and secondary imbibition curves and corresponding scanning curves for the intermediate water saturations.

5.2 Experimental technique

We used unconsolidated quartz sand samples with an average grain size fraction of $360 < D_{50} < 410$ micron. The sample holder consists of 3 parts: two stainless steel end-pieces and a non-conductive PEEK (Polyetheretherketone) ring. The untreated sample, with a diameter of 84 mm and a height of 27 mm, was placed in the sample holder and vibrated for 10 minutes. In order to support the sample, two types of metallic filters are used, which are placed inside the end-pieces.

To measure the permittivity, a component analyzer (Wayne-Kerr, 6640A) is connected to the sample holder, whereby the two stainless steel end-pieces, the support filters included, act as electrodes. Our set-up contains two pressure transducers to monitor the water and gas pressure, a pressure difference transducer that records the capillary pressure and two syringe pumps, which can be set to a constant injection/production rate or to a constant pressure. A detailed description of the experimental set-up and sample holder is presented in *Plug et al.* [2007]. In the experiments we used distilled water as the wetting phase and N_2 or CO_2 as the non-wetting phase. We define P_c as the difference in bulk water and gas phase pressure, measured by the pressure difference transducer. The water saturation is determined from the produced or injected water volume. In this study different pressure conditions were investigated and the experiments were conducted at a constant temperature (temperature stability ≤ 0.5 °C).

To perform a capillary cycle, we saturated the evacuated sample with water. We started with a dewatering stage (primary drainage) and before the connate water saturation was reached the flow direction was changed and the secondary imbibition was conducted. Different drainage and imbibition scanning curves were obtained after the first cycle had been measured. Injection and production flow rates were less than 0.5 ml/hr in all cycles.

During the displacement processes the impedance amplitude, $|Z|$ [Ω], and phase angle, θ [rad], were measured as a function of the frequency (f) and are related to the complex permittivity (ε_s^*) of the sample, defined by $\varepsilon_s^* = \varepsilon'_s - i\varepsilon''_s$. Here ε'_s and ε''_s represent the real and the imaginary part of the permittivity respectively. We used air measurements [*Plug et al.*, 2007] to correct for additional impedance effects and parasite capacitances, caused by background noise, the sample holder configuration, the influence of the connecting cables and possible electrode

polarization [*Chelidze et al.*, 1999; *Roberts and Lin*, 1997]. We calibrated the tool for materials with known permittivity in the range from 2 to 25 [-]. The measurements were compared with theoretical values and high precision and good agreement was found [*Plug et al.*, 2007].

5.3 Experimental results

Data for P_c and ε'_s were obtained on four different samples (S1-S4) for the N_2-water-sand and CO_2-water-sand systems in the fluid pressure range from atmospheric pressure to 13 bar and temperatures between 27 and 28°C. Figure 5.1 shows the $P_c - S_w$ curves for two N_2 experiments conducted at atmospheric pressures (S1) and 8 bar (S2a,b). In Figure 5.2 we show the capillary pressure curves for the drainage and imbibition cycles with CO_2 at pressures of 8 bar (S3a,b) and 13 bar (S4a-f). Different $P_c - S_w$ scans (S4c-f) at 13 bar CO_2 were conducted in the intermediate water saturation range of $0.41 < S_w < 0.78$. Comparison of the primary drainage and secondary imbibition $P_c - S_w$ curves for both the N_2 and CO_2 experiments show similar values for the drainage capillary pressure and agree within the experimental error, except at low water saturations.

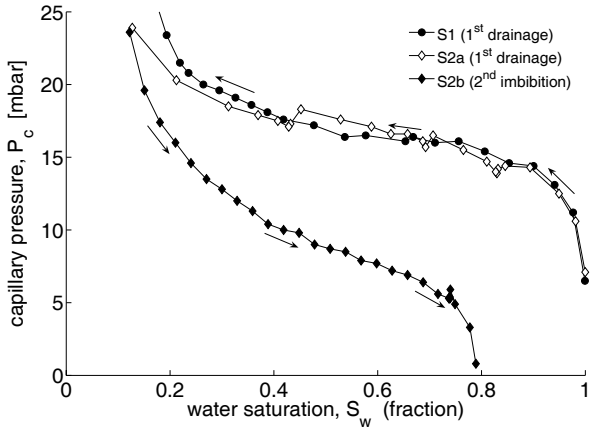

Figure 5.1 Capillary pressure curves for the N_2–sand–water system at atmospheric pressure (S1) and 8 bar (S2a, b). Hysteresis between the primary drainage (S2a) and the secondary imbibition (S2b) for the 8 bar N_2 experiments is clearly visible.

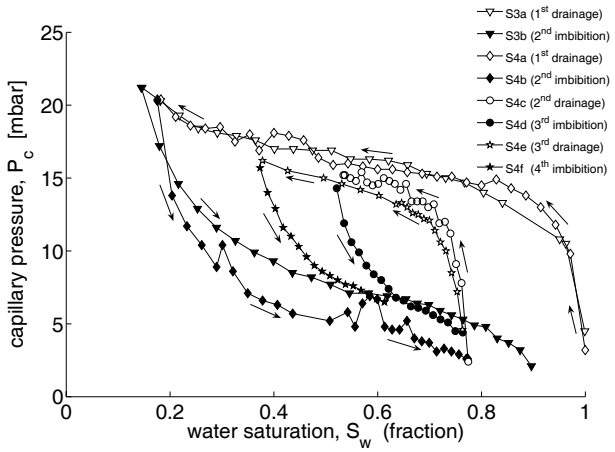

Figure 5.2 Capillary pressure curves for the CO_2-sand-water system at 8 bar (S3a, b) and 13 bar (S4a-f). The primary drainage curves (S3a and S4a) for both pressure conditions coincide. For the secondary imbibition (S3b and S4b) a shift in capillary pressure is observed. The capillary pressure hysteresis for water-wet porous media is observed, where the drainage curves lie above the imbibition curves. For the 13 bar CO_2 experiment, drainage (S4c, S4e) and imbibition (S4d, S4f) scans are conducted and are in between the primary drainage and secondary imbibition curve.

For both N_2 and CO_2 the drainage and imbibition capillary cycles show the conventional hysteresis for a water-wet porous medium, with the primary drainage curve showing higher values than the secondary imbibition curve. For the scanning curves measured at 13 bar (see Figure 5.2, S4c-S4f) the expected behavior was observed, because each curve lies between the primary drainage and secondary imbibition curve.

In the Figures 5.3 and 5.4 we show ε'_s as function of S_w for the N_2 and CO_2 experiments at $f = 100\,\text{kHz}$ and $f = 3\,\text{MHz}$, respectively. In the 3 MHz case, ε'_s shows a small hysteresis and all the curves follow a monotonic behavior. Furthermore, the permittivity scanning curves (Figure 5.4, S4c-f) coincide with the secondary imbibition curve (S4b). At a frequency of 100 kHz and at $S_w < 1$, ε'_s clearly shows hysteresis between the primary drainage curves (S2a, S3a and S4a) and the corresponding secondary imbibition curves (S2b, S3b and S4b). In all cases ε'_s during secondary imbibition was higher than during primary drainage, except near the residual gas saturation. Here the imbibition curves decline steeply (see S2b in Figure 5.3 and S3b in Figure 5.4). The non-monotonic behavior in ε'_s (100

kHz), observed for the main capillary cycle, was reproduced in all experiments (see Figures 5.3 and 5.4). It shows a maximum at $S_w = S_{w,m}$, and has a smooth appearance. The 100 kHz measurements can attain values that are twice as high as for the high frequency case. However, at $S_w = 1$, the low frequency ε'_s coincides with the values measured at high frequency (3 MHz) for all experiments and it is most likely that the values would coincide in the same way for $S_w = 0$. It is clear that the small gas solubility does not affect the low frequency permittivity, because a similar behavior was obtained for both the almost insoluble N_2 and the slightly soluble CO_2.

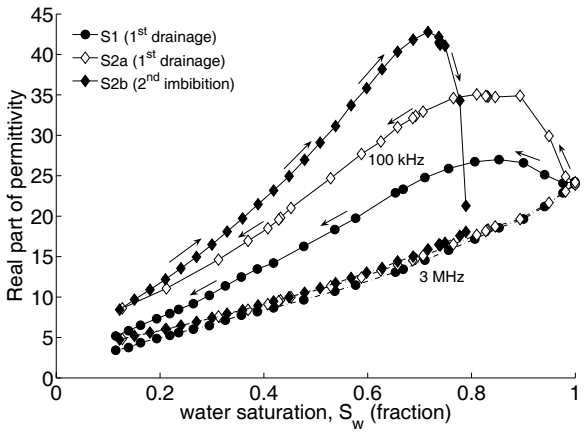

Figure 5.3 ε'_s (real part of the complex permittivity ε_s^*) as function of S_w for the N_2-sand-water system. S1 and S2a represent the primary drainage curves at atmospheric pressure and 8 bar, respectively. S2b is the secondary imbibition curve for the 8 bar case. The solid lines represent ε'_s for the 100 kHz and the dashed lines the 3 MHz. The permittivity for the 3 MHz shows small hysteresis between the drainage (S2a) and the imbibition (S2b). The permittivity obtained for 100 kHz show non-monotonic behavior and hysteresis where the imbibition curve (S2b) lie above the drainage curve (S2a).

For the N_2 experiments as presented in Figure 5.3, ε'_s during primary drainage at 8 bar (S2b) was higher than ε'_s measured for atmospheric conditions (S1). We were not able to check the reproducibility of this result. However, the behavior for

both pressure conditions was similar and for both cases the maximum value of ε'_s was found at $S_{w,m} \approx 0.85$.

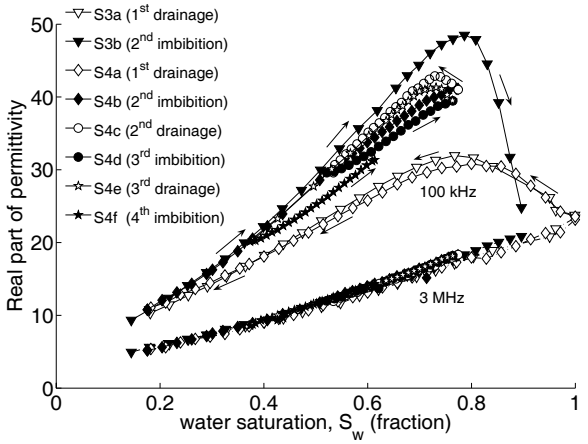

Figure 5.4 ε'_s as function of S_w for the CO_2-sand-water system. S3a and S4a represent the primary drainage curves at 8 bar and 13 bar, respectively and S3b and S4b are the secondary imbibition curves. The solid lines represent ε'_s for the 100 kHz case and the dashed lines the 3 MHz case. The low frequency curves clearly demonstrate hysteresis and non-monotonic behavior is observed where the secondary imbibition curves (S3b and S4b) are above the primary drainage curves (S3a and S4a). The 3 MHz, scanning curves (S4c-f), conducted for the 13 bar CO_2 case, coincide with the secondary imbibition curve. At 100 kHz, the drainage scanning curves (S4c, e) lie above the imbibition curves (S4d, f) and approximate the secondary imbibition curve.

During secondary imbibition (S2b), $S_{w,m}$ decreased towards 0.72. From Figure 5.4, it is clear that the difference in $S_{w,m}$ between the primary drainage and the secondary imbibition process for the CO_2 experiments was much smaller. In both cases $S_{w,m} \approx 0.8$ and $S_{w,m}$ for drainage was only slightly higher than for imbibition. Remarkable is that the primary drainage curves at 100 kHz for the CO_2 experiments coincide, whereas the secondary imbibition curve measured at 8 bar (S3b) lies above the 13 bar imbibition curve (S4b).

Surprisingly, the permittivity scanning curves at 100 kHz as presented in Figure 5.4, show that the drainage curves (S4c and S4e) lie above the imbibition curves (S4d and S4f). This is contrary to the main capillary cycle, where ε'_s is higher for

secondary imbibition than for primary drainage. Moreover, the permittivity scanning curves approximate the secondary imbibition curve (S4b), where the drainage curves (S4c and S4e) are higher and the imbibition curves (S4d and S4f) are lower than the secondary imbibition curve.

Figure 5.5 shows the curves that are obtained by subtracting the high frequency (3 MHz), permittivity data from the low frequency (100 kHz) data, for both the N_2 and CO_2 experiments. Consequently, these curves are zero for $S_w = 1$ and possibly also for $S_w = 0$. Different results were obtained for the low (E1a) and high (E2a) pressure primary drainage curves measured for N_2. The primary drainage curves for CO_2 appear to be more or less the same for the 8 bar (E3a) and 13 bar (E4a) experiments. The imbibition curves for N_2 and CO_2 coincide at low water saturations, but start to diverge at higher water saturations. It appears that the E2b and E3b secondary imbibition curves would approach zero if slightly higher water saturations could have been applied.

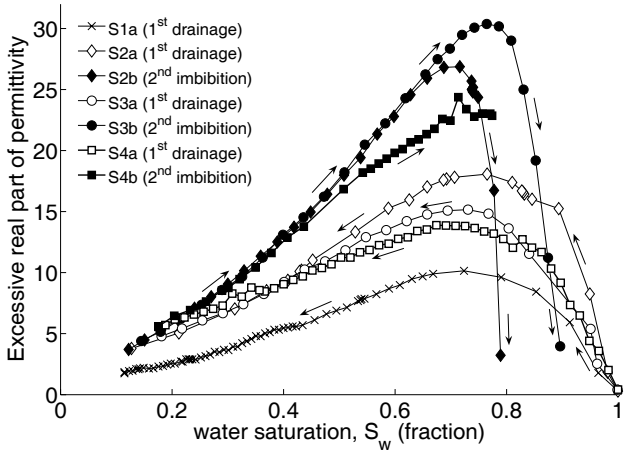

Figure 5.5 The anomalous permittivity as function of the water saturation for atmospheric N_2 (S1a), 8 bar N_2 (S2a, b), 8 bar CO_2 (S3a,b) and 13 bar CO_2 (S3a,b). The excessive ε'_s is obtained by subtracting the 3 MHz data from the 100 kHz data. We consider these curves, representing polarization effects, as a qualitative measure for the interfacial area.

5.4 Discussion

The high frequency permittivity data (3 MHz) followed the typical behavior of one of the mixing rules and are monotonic [see *Plug et al.*, 2007]. Hence, for increasing water saturations, increases steadily. However, the 100 kHz data (Figures 5.3 and 5.4) show no steady rise for increasing S_w, but a non-monotonic behavior of ε'_s as function of the water saturation. We attribute this behavior to polarization effects, occurring at the solid-water and the water-gas interfaces of water layers. Additionally, ionic transport in the water layers will cause the build-up of dipolar layers and contributes to the permittivity measured at 100 kHz.

The trajectory of the low frequency permittivity as function of the water saturation is interpreted using percolation theory and strongly depends on the presence of the gas phase. During (primary) drainage the gas phase, will first penetrate the larger pores, resulting in an increase in electric permittivity. This is the case during the first stage of the primary drainage curves, where already for small amounts of gas, ε'_s increases rapidly to a maximum. This may be explained by increasing water-gas interfaces. The sand sample is completely water-wet ($P_c > 0$) meaning that all the grains are coated with a thin water layer. These water layers can become extremely thin on the convex side of the grains for which the nearby pores are filled with gas that protrudes the water-filled pores. Percolation theory suggests that P_c must be high enough for the gas to invade these pores. This is the case when the number of allowed pores, which are big enough for the gas to invade, exceeds the percolation threshold. This percolation threshold, where the gas phase forms a continuous path, is reached at the point where ε'_s shows a maximum at $S_w = S_{w,m}$. As the gas pressure increases further, and thus P_c still increases, ε'_s decreases. We understand this as gas saturation increases, and a large part of the water in the thin layers is 'bound' to the grains (not free), rotation of the dipole orientations of the water molecules in these thin films becomes difficult under the presence of an electric field. This results in relatively weak polarization effects. The hysteresis in ε'_s as observed between the primary drainage (e.g., S4a in Figure 5.4) and secondary imbibition process (e.g., S4b in Figure 5.4) can be explained by different phase geometries and surface water distributions (clusters).

Combining the capillary pressure curves (Figures 5.1 and 5.2) with the corresponding permittivity curves (Figures 5.3 and 5.4) results in a unique relation between P_c, S_w and ε'_s. The permittivity behavior as shown in Figures 5.3 and 5.4 looks qualitatively similar to the interfacial area data obtained from network models and micro-pore models, which show the typical smooth and non-monotonic shape [*Reeves and Celia*, 1996; *Held and Celia*, 2001; *Cheng et al.*, 2004]. For our experiments, the primary drainage and secondary imbibition curves lie on a simple plane, establishing the unique relation of capillary pressure as a function of water saturation and electric permittivity. Unfortunately, a 3-dimensional view, as presented in the work of *Reeves and Celia*, [1996] and *Cheng et al.* [2004], does not graphically clarify this uniqueness. Since the low frequency ε'_s relates to polarization effects on the gas-water and water-solid interfaces, and the distribution of these interfaces contributes to the permittivity hysteresis, the electric permittivity can be seen as a measure for the interfacial area. Investigation of the exact relation between ε'_s and interfacial area is beyond the scope of this study and is therefore subject for future work.

Comparing different studies on water-wet samples, it can be concluded that there is no general consensus on whether the interfacial area as function of S_w is higher for imbibition than for drainage. The same applies to the scanning curves (see Figure 5.4, S4c-f). The differences between our $\varepsilon'_s - S_w$ and $a_{wn} - S_w$ relationships, as presented in earlier work, can be explained by the definition of the interfacial area. *Reeves and Celia* [1996] estimated in their theoretical study the interfacial area between the water and gas phase, but they ignored the wetting films. *Cheng et al.* [2004] only described the capillary pressure dominated interface for their network model, whereas *Dalla et al.* [2002] assumed the wetting-non-wetting interface to be a function of all specific interfacial areas.
Based on our findings, we propose that both the gas/liquid and the fluid/solid interfaces are necessary to provide unique relationships between capillary pressure, electric permittivity and water saturation.

5.5 Conclusions

We have found that the low frequency ε_s' behavior can primarily be ascribed to the polarization of both the gas-water and water-solid interfaces, to different bulk phase geometries and distributions and on saturation history, which occur during drainage and imbibition. Our experimental data show that capillary pressure is a unique function of the permittivity and the water saturation. Hence, our results provide the experimental evidence that the low frequency electric permittivity is a measure to describe the interfacial area. This leads to new and important insights into the description of multiphase fluid flow in porous media and understanding of pore-scale mechanisms.

Bibliography

Chelidze, T. L., and Y. Gueguen (1999), Electrical spectroscopy of porous rocks: a review –I. Theoretical model, *Geophys. J. Int.*, *137*, 1-15.

Chelidze, T. L., Y. Gueguen, and C. Ruffet (1999), Electrical spectroscopy of porous rocks: a review –II. Experimental results and interpretation, *Geophys. J. Int.*, *137*, 16-34.

Cheng, J.-T., L. J. Pyrak-Nolte, D. D. Nolte, and N. J. Giordano (2004), Linking pressure and saturation through interfacial areas in porous media, *Geophys. Res. Lett.*, *31,* L08502, doi:10.1029/2003GL019282.

Dalla, E., M. Hilpert, and C. T. Miller (2002), Computation of the interfacial area for two-fluid porous medium systems, *J. Cont. Hydrology*, *56*, 25-48.

Hassanizadeh, S.M., and W. G. Gray (1993), Thermodynamic basis of capillary pressure in porous media, *Water Resour. Res.*, *29*, 3389–3405.

Held, R. J., and M. A. Celia (2001), Pore-scale modelling extension of constitutive relationships in the range of residual saturations, *Water. Resour. Res.*, *37*, 165-170.

Knight, R. J., and A. Nur (1987), The dielectric constant of sandstones, 60 kHz to 4 MHz, *Geophys.*, *52*, 644-654.

Knight, R. (1991), Hysteresis in the electrical resistivity of partially saturated sandstones, *Geophys.*, *56*, 2139-2147.

Knight, R., and A. Abad (1995), Rock /water interaction in dielectric properties: Experiments with hydrophobic sandstones, *Geophys.*, *60*, 431-436.

Morrow, N. (1970), Physics ad thermodynamics of capillary action in porous media, *Ind. Eng. Chem.*, *62*, 32-56.

Plug, W. J., E. C. Slob, J. Bruining, and L. M. Moreno Tirado (2007), Simultaneous measurement of hysteresis in capillary pressure and electric permittivity for multi-phase flow through porous media, *Geophys. Letters*, doi: 10.1190/1.2714684.

Reeves, P. C., and M. A. Celia (1996), A functional relationship between capillary pressure, saturation and interfacial area as revealed by a pore-scale network model, *Water Resour. Res.*, *32*, 2345–2358.

Roberts, J. J., and W. Lin (1997), Electrical properties of partially saturated Topopah Spring Tuff: water distribution as function of saturation, *Water Resour. Res.*, *33*, 577-587.

Ruffet, C., Y. Gueguen, and M. Darot (1991), Complex conductivity measurements and fractal nature of porosity, *Geophys.*, *56*, 758-768.

Seleznev, N., A. Boyd, T. Habashy and S. Luthi (2004), Dielectric mixing laws for fully and partially saturated carbonate rocks, Proceedings of the SPWLA 45th Annual Symposium, paper CCC.

Ulrich, C., and L. D. Slater (2004), Induced polarization measurements on unsaturated, unconsolidated sands, *Geophys.*, *69*, 762-771.

Chapter 6 Conclusions

This chapter is divided in two parts. The first part summarizes the most general conclusions from this work and in the second part we list the conclusions of the four individual papers as presented in Chapters 2-5.

6.1 General conclusions

- A unique tool based on the porous plate technique, is designed and successfully used. The tool can measure the (drainage / imbibition) capillary pressure and dielectric coefficient (<20 bar) for pressures up to supercritical conditions, i.e., up to 100 bar and 45°C.
- The capillary pressures in the CO_2-sand-water system decrease with increasing pressures corresponding to the pressure dependence of the interfacial tension.
- Dissolution rate effects for CO_2 are only observed at low pressures, whereas at higher pressures instantaneous equilibrium can be assumed.
- No flow rate dependency is observed for the CO_2/N_2-sand-water systems, indicating static conditions on the macro-scale.
- During primary drainage the coal behaves water-wet, whereas during imbibition CO_2-wet behavior is observed.
- If CO_2 injection is stopped the capillary pressure decreases significantly. Vice versa the imbibition capillary pressure increases when water injection is stopped. Similar effects are absent or much smaller in the sand-CO_2-water experiments.
- Water film and gas film rupture effects can explain the rate behavior.
- It can be concluded that the wetting behavior of coal is most conveniently obtained from the imbibition behavior.
- The applied injection rates are too small to observe macroscopic dynamic effects caused by viscous forces but too long to see microscopic dynamic effects related to film rupture.
- Combined non-destructive measurement of capillary pressure and dielectric coefficient is possible.
- The results for low frequencies show a typical behavior that is also observed in measurements and computations of interfacial area.

6.2 Conclusions per chapter

Chapter 2: Capillary pressure of the sand-CO_2-water system

- A capillary pressure set-up has been developed and validated that can be used to measure the capillary pressure behavior for CO_2 sequestration applications.
- For the small injection rates applied, the viscous forces are negligible and the capillary pressure curves are considered as static.
- The numerical results show that the SIPERM filters do not influence the measured $P_c - S_w$ curves for the applied flow conditions.
- Increasing CO_2 pressures result in decreasing primary drainage capillary pressures for all samples used. This can be explained by the decrease in interfacial tension.
- From the comparison between the N_2 and CO_2 experiments, we conclude that the capillary pressure is not influenced by the dissolution of CO_2 in water.
- Measurements close to the critical point of CO_2 show alternate drainage and imbibition events during CO_2 injection. This is a result of small perturbations that change the density and viscosity of CO_2 and temporary CO_2 wet behavior.
- The wettability of the quartz sand is altered to intermediate wet in the presence of CO_2 under supercritical conditions. This is a result of improving solvent properties of CO_2 and the decreasing pH of water.
- Good agreement is found between the experimental results and the model prediction for both the CO_2 and N_2 injection drainage experiments.
- The model shows that the water production and gas injection behavior depends largely on mass transfer rate and diffusion of CO_2 in water. These effects become negligible for the injection of liquid CO_2.
- The capillary pressure behavior must be considered in CO_2 sequestration application, e.g., the caprock integrity and drainage and imbibition events in heterogeneous rocks. Our measurements show that wetting alteration and the abrupt phase changes and accompanying density and viscosity changes may affect the success of CO_2 sequestration.

Chapter 3: Capillary pressure and wettability behavior of the coal-CO_2-water system at high pressures

- A capillary pressure set-up has been developed and validated that can be used to determine the wettability of the coal-CO_2-water system as a function of the system pressure. The interpretation is facilitated by comparison of the sand-CO_2-water and coal-CO_2-water experiments at a range of pressure and temperature conditions. Reproducibility of the experiments is considered good.
- Increasing CO_2 pressures result in decreasing primary drainage capillary pressures for all samples used. This can be explained by the decrease in interfacial tension.
- Both the medium and high rank coal is water-wet during the primary drainage process; this behavior is in contrast with contact angle experiments.
- With increasing system pressures the wettability of the medium rank coal alters from water-wet to CO_2-wet. High rank coal is CO_2-wet during primary imbibition experiments in the entire pressure range. The behavior during imbibition corresponds to contact angle measurement data.
- Fast water breakthrough during the imbibition process indicates CO_2-wet behavior.
- Imbibition tests provide relevant data to evaluate the wetting properties of coal.
- The difference between imbibition and drainage experiments can be explained by the stability of a water layer on the coal. Such a film must be ruptured before the coal becomes CO_2-wet.
- This film rupture may imply that the time scale in laboratory experiments is not representative for field scale behavior.

Chapter 4: Simultaneous measurement of hysteresis in capillary pressure and electric permittivity for multi-phase flow through porous media

The measurements presented in this work show that it is possible to measure the capillary pressure and the permittivity properties simultaneously with a non-destructive technique. The tool is calibrated for $f = 3$ MHz using materials with known permittivity behavior within the range of $2 - 25$ [-] and can be used for fluid pressures up to 20 bar. The impedance tool is widely applicable and can be

used for fluid-bearing rocks and soils, and the results are, therefore, relevant for applications in near surface, as well as exploration and production geophysics. Good agreement of the measured electric permittivity with the Complex Refractive Index model indicates that induced polarization is not observed for 3 MHz and the water saturation is reasonably predicted. Moreover, the experimentally observed hysteresis in the real part of the complex electric permittivity provides evidence that a better description of the capillary pressure hysteresis can be obtained than that from water saturation alone. Because the presence of water plays a dominant role in the permittivity behavior, low frequency measurements are necessary to assist in the interpretation of the permittivity hysteresis in terms of interfacial activities.

Chapter 5: Capillary pressure as a unique function of electric permittivity and water saturation

We have found that the low frequency ε_s' behavior can primarily be ascribed to the polarization of both the gas-water and water-solid interfaces, to different bulk phase geometries and distributions and on saturation history, which occur during drainage and imbibition. Our experimental data show that capillary pressure is a unique function of the permittivity and the water saturation. Hence, our results provide the experimental evidence that the low frequency electric permittivity is a measure to describe the interfacial area. This leads to new and important insights into the description of multiphase fluid flow in porous media and understanding of pore-scale mechanisms.

Summary

Measurements of capillary pressure and electric permittivity of gas–water systems in porous media at elevated pressures

Application to geological storage of CO_2 in aquifers and wetting behavior in coal

The main challenge of using fossil fuel appears to be the reduction of greenhouse gas emissions, which are considered to cause the current global heating. The most promising technique to reduce the emissions is storage of CO_2 in geological formations. The main candidates are depleted gas and oil reservoirs, salt caverns, deep (saline) aquifers and unmineable coal layers. A variety of reservoir properties determine the efficiency, capacity and safety of the sequestration process. Heterogeneity of the formation, gas trapping, phase behavior, adsorption capacity of the rock (or coal) and the sealing integrity are considered as the most important parameters. However, two important properties, which have not been given the sufficient interest in literature, are capillary pressure and wetting behavior. Depending on the heterogeneity structure, capillary effects can have a positive or negative effect on the CO_2 sequestration efficiency. Moreover the sealing capacity of the caprock depends on the capillary behavior. In coal layers the storage capacity and diffusion rates of CO_2 are related to the wetting behavior of the coal-CO_2-water system. In a water-wet system, the water accumulates in the micro cleats, where the CO_2 diffusion is slow. In a CO_2-wet system the micro-cleat system will be filled with gas with much higher diffusion rates. It is also expected that CO_2 sorption will be stronger in a CO_2-wet coal.

In all heterogeneous media fluid displacement will be characterized by a sequence of drainage and imbibition events. Here and below drainage is defined as the removal of water and imbibition as the reverse process. Between the drainage and imbibition, de capillary pressure shows a non-uniqueness, the so-called capillary hysteresis. It has been suggested that capillary hysteresis can be uniquely defined in terms of the water saturation and the interfacial area. In principle interfacial area can be measured with interfacial tracers and in micro-models, which are respectively complicated and less realistic. In this work we have used the simultaneous measurement of capillary pressure and electric permittivity, which can be interpreted in terms of interfacial effects. The measurement of capillary

pressure, wetting and the fundamental aspects of capillary hysteresis are the themes of this thesis. To conduct these measurements a unique tool based on the porous plate technique, is designed and used. The tool uses a constant, but small, injection rate of CO_2 or water and monitors continuously the capillary pressure. It can measure the drainage and imbibition capillary pressure and electric permittivity. The maximum pressure during the simultaneous measurements is 20 bar. During the measurements of the capillary pressure only, the maximum pressure is 100 bar and temperatures up to 45°C can be applied to establish supercritical conditions for the CO_2 phase.

Chapter 2 deals with the capillary pressure behavior of the gas (CO_2 or N_2)-water-sand system. The comparison between the results obtained for the two gases can be used to observe dissolution effects. Dissolution rate effects are only observed at low CO_2 pressures, whereas at higher CO_2 pressures instantaneous equilibrium can be assumed. The capillary pressure decrease with increasing CO_2 pressures and corresponds to the pressure dependence of the interfacial tension. In chapter 3, the capillary pressure and the derived wetting behavior in coal is discussed. To facilitate the interpretation of the coal experiments the results are compared to the results discussed in chapter 2. During primary drainage the coal behaves water-wet, whereas during imbibition CO_2-wet behavior is observed. No rate effects are observed if we reduce the CO_2 injection rate by a factor of three. However, if CO_2 injection is stopped the capillary pressure decreases significantly. Vice versa the imbibition capillary pressure increases when water injection is stopped. Similar effects are absent or much smaller in the sand-CO_2-water experiments. This behavior can be explained by water film and gas film rupture effects. It can be concluded that the wetting behavior of coal is most conveniently obtained from the imbibition behavior. It is asserted that the applied injection rates are too small to observe macroscopic dynamic effects caused by viscous forces but too long to see microscopic dynamic effects related to film rupture. In chapter 4 and 5, the combined measurements of capillary pressure and electric permittivity are described. Chapter 4 deals with the calibration, precision and validity of the impedance tool. Chapter 5 shows data of the electric permittivity as a function of saturation for frequencies of 100 kHz and 3 MHz. The results for low frequencies show a typical behavior that can be related to interfacial area.

The thesis is based on four papers, respectively included in chapters 2-5. For convenience the abstracts of the individual papers are listed below.

Chapter 2: Capillary pressure of the sand-CO_2-water system

Accurate modeling of storage of carbon dioxide (CO_2) in heterogeneous aquifers requires experiments of the capillary pressure as function of temperature and pressure. We present a method with which static drainage and imbibition capillary pressures can be measured continuously as a function of saturation at various temperature (T) and pressure (P) conditions. The measurements are carried out at (T, P) conditions of practical interest. Static conditions can be assumed as small injection rates are applied. The capillary pressure curves are obtained for the unconsolidated sand-distilled-water-CO_2 system. The experimental results show a decrease of drainage and imbibition capillary pressure for increasing CO_2 pressures and pronounced dissolution rate effects for gaseous CO_2. Significant capillary pressure fluctuations and negative values during imbibition are observed at near critical conditions. The measurement procedure is validated by a numerical model that simulates the experiments.

Chapter 3: Capillary pressure and wettability behavior of the coal-CO_2-water system at high pressures

Enhanced Coal Bed Methane (ECBM) combines recovery of CH_4 from coal seams with storage of CO_2. The efficiency of ECBM depends on the CO_2 transfer rate between the macro-cleats, via the micro cleats to the coal matrix. Diffusive transport of CO_2 in the small cleats is enhanced when the coal is CO_2-wet. Indeed for water-wet conditions the small fracture system is filled with water and the rate of CO_2 sorption and CH_4 desorption is affected by slow diffusion of CO_2. This work investigates the wetting behavior of coal using capillary pressures measured continuously as a function of saturation at in situ conditions. To facilitate the interpretation of the coal measurements we also obtain capillary pressure curves for unconsolidated sand samples. For medium and high rank coal the primary drainage capillary pressure curves show a water-wet behavior. Secondary imbibition experiments show that the medium rank coal becomes CO_2-wet as the CO_2 pressure increases. High rank coal is CO_2-wet during primary imbibition. The imbibition behavior is in agreement with contact angle measurements. Hence we conclude that imbibition tests provide the practically relevant data to evaluate the wetting properties of coal.

Chapter 4: Simultaneous measurement of hysteresis in capillary pressure and electric permittivity for multi-phase flow through porous media

A tool has been presented that simultaneously measures the complex permittivity and the capillary pressure characteristics for multiphase flow. The sample holder is a parallel plate capacitor and a precision component analyzer is used to measure the impedance amplitude and phase angle as a function of frequency (1 kHz to 3 MHz). The complex impedance of the (partially) saturated sample is directly related to the effective complex permittivity. We have conducted main drainage and main imbibition cycles for unconsolidated sand-water-gas (CO_2/N_2) systems at 8-bar pressure and at temperatures between 27°C and 28°C. Hysteresis in capillary pressure and electric permittivity, as a result of phase distribution, is found between drainage and imbibition for $f = 3\,\mathrm{MHz}$ and becomes more pronounced at higher water saturations. Good agreement of the measured electric permittivity with the complex refractive index model (CRIM) indicates that induced polarization is not observed for 3 MHz and the water saturation is reasonably predicted. The experiments have been performed to study the capillary pressure behavior during CO_2 sequestration.

Chapter 5: Capillary pressure as a unique function of electric permittivity and water saturation

The relation between capillary pressure (P_c) and interfacial area has been investigated by measuring P_c and the electric permittivity (ε^*) at 100 kHz simultaneously as function of the water saturation, (S_w). Drainage and imbibition experiments have been conducted for sand-distilled water-gas (CO_2/N_2) systems. The main capillary cycles and the scanning curves show hysteresis with the drainage curves showing higher values than the imbibition curves. The 100 kHz permittivity data also show hysteresis between drainage and imbibition. Furthermore non-monotonic behavior is observed, which is analogous to the interfacial area characteristics obtained from network and micro-pore models. The permittivity behavior is attributed to polarization of the gas-water and water-solid interfaces. The permittivity hysteresis is provoked by the different phase distributions and geometries. Our results show that P_c is a unique function of the permittivity and S_w, and therefore this work provides clear evidence that the permittivity is a measure for the interfacial area.

Samenvatting

Metingen van capillaire druk en elektrische permittiviteit van gas-water systemen in poreuze media bij hoge druk

Toepassing voor geologische opslag van CO_2 in aquifers en het bevochtigingsgedrag van steenkool

Bij het gebruik van fossiele brandstoffen ligt de belangrijkste uitdaging in het reduceren van de uitstoot van broeikasgassen, die de oorzaak vormen voor de opwarming van de aarde. De meest veelbelovende oplossing voor de beperking in uitstoot is opslag van CO_2 in geologische formaties. Gedepleteerde gas- en oliereservoirs, zoutgrotten, diepe (zout)watervoerende lagen en onontginbare steenkoollagen. Een aantal reservoireigenschappen bepalen de efficiëntie, capaciteit en veiligheid van het opslagproces. Heterogeniteit van de formatie, het "opsluiten" van gas in de poriën, de adsorptiecapaciteit van het gesteente (of de steenkool) en de mate van doorlatendheid van de afsluitende laag boven het reservoir, worden beschouwd als de meest belangrijke parameters. Echter, twee belangrijke eigenschappen zijn onderbelicht gebleven in de literatuur, namelijk: de capillaire druk en het bevochtigingsgedrag. Afhankelijk van de heterogene structuur kan de capillaire druk een positief of negatief effect hebben op de efficiëntie van de opslag CO_2. Verder hangt de afdichtingscapaciteit van de afsluitende bovenlaag af van het capillaire gedrag.
In koollagen zijn de opslagcapaciteit en de diffusiesnelheid gerelateerd aan het bevochtigingsgedrag van het steenkool-CO_2-water systeem. Een systeem waarin water de bevochtigende fase is zal het water accumuleren in de micro scheurtjes waar de diffusie van CO_2 laag is. In een systeem waar CO_2 de bevochtigende fase is zal de CO_2 de micro scheurtjes opvullen, en de diffusie van CO_2 zal daardoor veel groter zijn. Verwacht wordt dat de sorptie van CO_2 veel sterker zal zijn voor steenkool waarin CO_2 de bevochtigende fase is.

In ieder heterogeen medium zal de vloeistofverplaatsing worden gekarakteriseerd door een aaneenschakeling van drainage- en imbibitiegebeurtenissen. Hier wordt drainage gedefinieerd als de verwijdering van water en imbibitie als het omgekeerde proces. De capillaire druk tijdens drainage en tijdens imbibitie is niet uniek en

wordt daarom ook wel capillaire hysterese genoemd. Er wordt gesuggereerd dat de capillaire hysterese kan worden gezien als een unieke functie van de watersaturatie en het grensoppervlak tussen de verschillende fases. In principe kan dit grensoppervlak worden gemeten met speciale grensvlaktracers en in micromodellen, die respectievelijk gecompliceerd en minder realistisch zijn. In deze studie is er gebruik gemaakt van simultane metingen van de capillaire druk en de elektrische permittiviteit, die kan worden geïnterpreteerd in termen van het grensoppervlak.

Het meten van de capillaire druk, het bevochtigingsgedrag en de fundamentele aspecten van de capillaire hysterese vormen de thema's van dit proefschrift. Om deze metingen uit te voeren is er een unieke opstelling, gebaseerd op de poreuze plaat techniek, ontworpen en gebruikt. Tijdens de metingen wordt er een constante, maar kleine hoeveelheid CO_2 of water geïnjecteerd en wordt de capillaire druk continu geregistreerd. Het apparaat meet zowel de drainage en imbibitie capillaire druk als de elektrische permittiviteit. De maximale druk die kan worden bereikt tijdens de simultane metingen is 20 bar. Tijdens het meten van alleen de capillaire druk kan de druk maximaal 100 bar zijn, en kunnen er temperaturen tot 45°C worden toegepast, waarbij CO_2 onder superkritische omstandigheden aanwezig is.

Hoofdstuk 2 behandelt het capillaire drukgedrag van het zand-gas(N_2/CO_2)-water systeem. De vergelijking tussen de meetresultaten van de twee gassen kan worden gebruikt om de oplosbaarheid van de CO_2 in het water te beschrijven. Oplosbaarheidseffecten zijn alleen gemeten voor lage CO_2 drukken, dit in tegenstelling tot hoge drukken, waarbij een instantaan evenwicht tussen water en CO_2 kan worden aangenomen. De afname van de capillaire druk met toenemende CO_2 drukken is in overeenstemming met de drukafhankelijkheid van de grensvlakspanning tussen water en CO_2.

In hoofdstuk 3 wordt de capillaire druk en het bevochtigingsgedrag van steenkool besproken. Om de interpretatie van de capillaire drukmetingen in steenkool te vergemakkelijken worden de resultaten vergeleken met de resultaten uit hoofdstuk 2. Tijdens de primaire drainage is het water de bevochtigende fase in steenkool, maar tijdens de imbibitie wordt de CO_2 de bevochtigende fase. Geen dynamische effecten zijn waargenomen tijdens het verkleinen van de injectiesnelheid van CO_2

met een factor drie. Echter, wanneer de CO_2 injectie wordt gestopt daalt de capillaire druk aanzienlijk. Vice versa, de imbibitie capillaire druk stijgt wanneer de water injectie stopt. Vergelijkbare effecten treden niet op of zijn veel kleiner voor het zand-CO_2-water systeem. Dit gedrag kan worden uitgelegd door het breken van de water en gas films. Geconcludeerd kan worden dat het bevochtigingsgedrag van steenkool het best kan worden verkregen door middel van imbibitie experimenten en dat de injectiesnelheden te klein zijn om de macroscopisch dynamische effecten, als gevolg van viskeuze krachten te kunnen observeren, en dat de injectiesnelheden te groot zijn om macroscopisch dynamische effecten als gevolg van het breken van de films te kunnen meten.

In de hoofdstukken 4 en 5 worden de simultane metingen van de capillaire druk en de elektrische permittiviteit beschreven. Hoofdstuk 4 behandelt de calibratie, precisie en de validiteit van het impedantie apparaat. In hoofdstuk 5 wordt de data gepresenteerd van de elektrische permittiviteit als functie van de watersaturatie voor frequenties tussen 100 kHz en 3 MHz. De resultaten met lage frequenties laten een typisch gedrag zien dat gerelateerd kan worden aan de het grensoppervlak.

Deze dissertatie is gebaseerd op 4 artikelen, zoals opgenomen in hoofdstuk 2 tot en met 5. Voor het overzicht zijn de samenvattingen van deze artikelen hieronder weergegeven.

Hoofdstuk 2: Capillaire druk van het zand-CO_2-water systeem
Accurate modelering van koolstofdioxide (CO_2) in heterogene watervoerende pakketten vereist experimenten waarbij de capillaire druk wordt gemeten als functie van de druk en de temperatuur. Wij presenteren een methode waarmee statische drainage en imbibitie capillaire drukken continu kunnen worden gemeten als functie van de watersaturatie bij verschillende temperatuur- (T) en drukcondities (P). De metingen zijn uitgevoerd bij (T, P) condities die relevant zijn voor de praktijk. Statische condities kunnen worden aangenomen wanneer kleine injectiesnelheden worden toegepast. De capillaire drukcurves zijn verkregen voor het ongeconsolideerde zand-gedestilleerd water-CO_2 systeem. De experimentele resultaten laten zien dat de drainage en imbibitie capillaire druk afneemt voor toenemende CO_2 drukken en dat uitgesproken oplosbaarheidseffecten zijn waargenomen voor gasvormig CO_2. Significante capillaire drukfluctuaties en negatieve waarden zijn gemeten voor (bijna) superkritische omstandigheden tijdens de imbibitie. The meetprocedure is gevalideerd aan de hand van een numeriek model dat de experimenten simuleert.

Hoofdstuk 3: Capillaire druk en het bevochtigingsgedrag van het steenkool-CO_2-water systeem bij hoge drukken
Bij *Enhanced Coal Bed Methane* (ECBM) wordt de winning van CH_4 uit steenkool gecombineerd met de opslag van CO_2. De efficiëntie van ECBM hangt af van de CO_2 interactiesnelheid van de macroscheuren, via de microscheuren, naar de steenkoolmatrix. Diffusie van CO_2 in de kleinste scheurtjes wordt verbeterd wanneer de CO_2 de bevochtigende fase is in de steenkool. Feitelijk wordt het systeem van scheurtjes gevuld met water wanneer water de bevochtigende fase is en daardoor wordt de sorptiesnelheid van CO_2 en de desorptiesnelheid van CH_4 bepaald door de lage CO_2 diffusie. In deze studie wordt het bevochtigingsgedrag van steenkool bij in situ condities onderzocht, waarbij gebruikt wordt gemaakt van de capillaire druk, continu gemeten als functie van de watersaturatie. Om de interpretatie te vereenvoudigen hebben we de capillaire drukcurves gemeten voor ongeconsolideerde zandmonsters. Voor steenkool met een gemiddelde inkolingsgraad laten de primaire drainage capillaire drukcurves zien dat water de bevochtigende fase is. De secondaire imbibitie experimenten laten zien dat voor steenkool met een gemiddelde inkolingsgraad CO_2 de bevochtigende fase wordt wanneer de CO_2 druk toeneemt. Steenkool met een hoge inkolingsgraad heeft CO_2 als de bevochtigende

fase tijdens primaire imbibitie. Het gedrag bij imbibitie is in overeenstemming met contacthoekmetingen. Daarom kunnen wij concluderen dat de imbibitie experimenten de relevante data geven voor in de praktijk om het bevochtigingsgedrag van steenkool te evalueren.

Hoofdstuk 4: Simultane meting van hysterese in capillaire druk en elektrische permittiviteit voor meerfasenstroming in poreuze media

In dit hoofdstuk wordt een apparaat gepresenteerd die simultaan de complexe permittiviteit en de capillaire drukkarakteristieken voor meerfasenstroming meet. De monsterhouder is een parallelle plaat condensator en een *precision component analyzer* wordt gebruikt om the amplitude van de impedantie en de fasehoek te meten als functie van de frequentie (van 1 kHz tot 3 MHz). De complexe impedantie van het (gedeeltelijk) gesatureerde monster is direct gerelateerd aan de effectieve complexe permittiviteit. Primaire drainage en imbibitie cycli zijn uitgevoerd voor ongeconsolideerd zand-water-gas (CO_2/N_2) systemen bij drukken van 8 bar en temperaturen tussen de 27°C en 28°C. Hysterese tussen de drainage en imbibitie voor $f = 3$ MHz is gemeten in de capillaire druk en de elektrische permittiviteit en is een gevolg van de verdeling van de fases en wordt neemt toe naarmate de watersaturatie toeneemt. De goede overeenstemming tussen de gemeten elektrische permittiviteit en het complexe refractie index model (CRIM) wijst erop dat er geen geïnduceerde polarisatie plaatsvindt bij 3 MHz en dat de watersaturatiebepaling acceptabel is. De experimenten zijn uitgevoerd binnen het kader van het onderzoek naar het gedrag van capillaire druk tijdens CO_2 opslag.

Hoofdstuk 5: Capillaire druk als unieke functie van de elektrische permittiviteit en de watersaturatie

De relatie tussen de capillaire druk (P_c) en het grensoppervlak is onderzocht door het simultaan meten van P_c en de elektrische permittiviteit (ε^*) bij 100 kHz als functie van de watersaturatie, (S_w). Drainage- en imbibitie-experimenten zijn uitgevoerd voor zand-gedestilleerd water-gas (CO_2/N_2) systemen. De primaire capillaire cycli en de *scanningscurves* laten hysterese zien, waarbij de drainagecurves hogere waarden hebben dan de imbibitiecurves. De permittiviteitsmetingen bij 100 kHz laten ook hysterese zien tussen drainage en imbibitie. Daarenboven is er niet-monotoon bedrag geobserveerd, dat analogie

vertoont met de karakteristieken van het grensoppervlak, verkregen door netwerk en *micro-pore* modellen. Het gedrag van de permittiviteit wordt toegekend aan de polarisatie van het gas-water en water-zand grensvlak. De hysterese in permittiviteit wordt teweeggebracht door de verschillende distributie van de fases en de geometriën. Onze meetresultaten laten zien dat P_c een unieke functie is van de permittiviteit en S_w, en dat daarom met deze studie aantoonbare bewijzen zijn geleverd dat de permittiviteit een mate is voor het grensoppervlak.

About the author

Willem-Jan Plug was born on the 16th of February 1978 in Katwijk aan Zee, the Netherlands. In 1996, he completed his secondary education (VWO) at the Pieter Groen College in Katwijk. In the same year, he started his academic education at Delft University of Technology, the Netherlands. He studied at the department of Civil Engineering and in 2002 he earned his M.Sc. degree in Water Management. The topic of his thesis was the development of a numerical model for density dependent flow in porous media to simulate movement of the fresh-salt water interface in coastal areas.
In 2002 he started his Ph.D. research in the Petroleum Engineering Section in the Department of Geotechnology of the Delft University of Technology. He conducted research on capillary pressure and electric permittivity in porous media with applications to geological storage of CO_2 in aquifers and unmineable coal layers. The work involved theoretical work and experimental investigations on capillary pressure and electric permittivity. The results of his research are presented in this Ph.D. thesis.
Since November 2006, he is working as a reservoir engineer at Horizon Energy Partners, the Hague, the Netherlands.

In his free time, he is active as a youth worker and is a member of the consistory of the Dutch Reformed Church of Katwijk.

Acknowledgements

This dissertation is the final result of my Ph.D. research. A number of people were involved to help me and to establish my ideas, to give a hand in writing and to support me over the last years.

First of all, I would like to thank Hans Bruining. As a supervisor and promoter, you helped me during the easy and the hard times of my research. The door was always open for questions and a social chat with jokes and "movie quotes". Even when you were not in your room and the door was locked, I could trace you in the Geotechnology building, using the yellow papers you stuck on the door. Your experience, advice and ideas throughout the years were very useful, as well as the discussions we had at your place on the Monday evenings.

I would like to thank Evert Slob. You always had time for answering my questions, explaining the fundamentals of geophysics or for drinking a cup of good fresh coffee. The discussions were very stimulating and your ideas on the different aspects of my research are much appreciated.

I would like to thank Karl-Heinz Wolf for adding me at the CATO program and his advice during the writing of this thesis. I appreciated the discussions in "het Torentje" on coal properties or the boring paper work scientists must do.
As advisors during my research, I would like to thank Fred Vermolen en Jan van Turnhout for their help and time.

It would have been impossible to conduct my experiments without the help and support of the Dietz Laboratory staff. Leo Vogt, Henk van Asten, Andre Hoving, Peter de Vreede, Karel Heller, Jan Etienne, Gerard Mathu, Adri Maljaars, Ellen Meijvogel, Jolanda Verhagen, Gerard Sigon and Henny van der Meulen, thank you for your advice in the laboratory.

I would thank the M.Sc. students I supervised; Johannes Visser, Siyavash Motealleh, Alireza Hassanzadegan and Leticia Moreno.

And of course I would like to thank my fellow Ph.D. colleagues from the Department of Geotechnology: Koen, Nicolai, Saikat, Bert-Rik, Hein, Twan, Roald, Ainhoa, Jeroen, Firas, Mohammed, Rouhi, Hamidreza, Patrick, Renato, Joris, Maarten, Talal and Jorn. We had a great time together with sharing our experiences, the advices and the good lunches in the Dietz laboratory including the interesting topics and conversations.

I am very grateful to my friends and family for their support during this research. Your interest in the topic and asking the most asked question "when do you finish your thesis?" are very appreciated as well.

At the end of these acknowledgements, I want to say thanks to the most important person in my life, my dear Wilma. Thank you so much for your support and help during this period of my life, especially in the last months. All the time you were right beside me to support and to help me. You were the person I could share the good and the bad moments with during my research, and you always showed your understanding, even when our time together was minimal. Wilma, without you I should not be the person I am now: I love you!

Katwijk, 22 Augustus, 2007

Willem-Jan Plug

Nomenclature

Quantity	*Symbol*	*Unit*
Permittivity of free space (8.854×10^{-12})	ε_0	F/m
Effective complex permittivity	ε_s^*	[-]
Real part of complex permittivity	ε'_s	[-]
Imaginary part of permittivity	ε''_s	
Sorting factor	λ_s	[-]
CO_2 viscosity	μ_{CO_2}	Pa s
N_2 viscosity (1.8×10^{-5})	μ_{N_2}	Pa s
Water viscosity	μ_w	Pa s
Phase angle	θ	rad
Water density	ρ_w	kg/ m^3
Density	ρ_{CO_2}	kg/ m^3
Sample density	ρ_s	kg/ m^3
Interfacial tension	σ	N/m
Rock porosity	φ	m^3/ m^3
Angular frequency	ω	Hz
Sample area	A / A_s	m^2
Water vapor concentration	c_{gw}	mol/m^3
Gas concentration	c_{gg}	mol/m^3
Gas concentration in water	c_{wg}	mol/m^3
Diffusion coefficient of CO_2 in water	D_{CO_2}	m^2/s
Diffusion coefficient of gas in water	D_g	m^2/s
Diameter hydrophobic filter	D_G	m
Characteristic length	D_L	m
Diameter coal/sand sample	D_{sample}	mm
Diameter of the perforations	D_p	mm
Diameter SIPERM filter	$D_{s,1}$	mm
Diameter SIPERM filter	$D_{s,2}$	mm

Diameter perforated plate	$D_{ss,1}$	mm
Diameter perforated plate	$D_{ss,2}$	mm
Diameter hydrophilic filter	D_{w}	mm
Average grain size	D_{50}	m
Frequency	f	Hz
Gravity constant	g	m/s^2
Sample height	H	mm
Henry's constant for	k_{Henry}	Pa
Water, gas relive permeability	k_{rw} , k_{rg}	m^3/m^3
Rock effective permeability	k	m^2
Pressure	P	mbar/bar/Pa
Atmospheric pressure	P_{atm}	Pa
Capillary pressure	P_{c}	mbar
Gas pressure	P_{g}	Pa
Water pressure	P_{w}	Pa
Universal gas constant	R	m^3Pa (mol K)$^{-1}$
Gas saturation	S_{g}	[-]
Residual gas saturation	S_{gr}	m^3/m^3
Water saturation	S_{w}	m^3/m^3
Residual water saturation	S_{wc}	m^3/m^3
Water saturation where ε'_{s} is max.	$S_{w,m}$	m^3/m^3
Time	t	s
Temperature	T	K
Injection rate	u_{inj}	ml/h
Gas injection rate	u_{g}^{inj}	m^3/s
Darcy gas/water velocity	u_{g}, u_{w}	$m^3/(m^2s)$
Volume	V	ml
Molar fraction gas in water	x_{gw}	[-]
Gas compressibility CO_2	z_{g}	[-]
Impedance	Z	Ω
Complex impedance	Z^*	Ω

Appendix A Capillary pressure in porous media

A.1 Introduction

Capillary pressure (P_c) plays an important role in the description of multiphase flow in subsurface formations. Because of the large systems considered in two-phase flow problems, we distinguish two scales: the micro-scale (pore scale) and the macro-scale (representative elementary volume, REV) at which the micro-scale properties are valid under specific assumptions. Since capillary pressure is an interfacial property, we first focus on the micro-scale, where two immiscible fluids are present in a pore. Subsequently we discuss the macro-scale relationships and the behavior of the capillary pressure.

Capillary pressure exists because of interfacial interaction between two fluids and the interaction between the fluids and the porous medium. In Figure A.1 a schematization of two mobile phases, the water (w) and gas (g) phase, in contact with a solid (s) surface is shown.

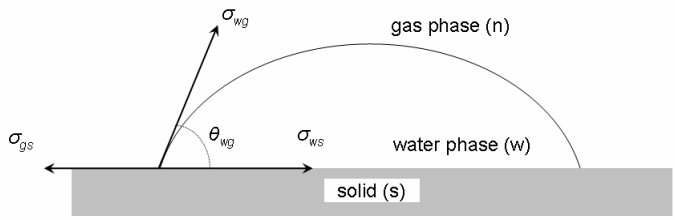

Figure A.1 Configuration of two fluids in contact with a solid surface. The water is the wetting phase and the gas is the non-wetting phase.

The interfacial tension between the water and the gas (n) phase is indicated by σ_{wg} [N/m] and σ_{ws} and σ_{gs} is the interfacial tension between the water phase and the solid and the gas phase and the solid phase respectively. The contact angle is

represented by θ_{wn} [°] and is by convention measured in the densest phase. The force balance in the equilibrium case yields

$$\sigma_{wn} \cos\theta_{wn} = \sigma_{ns} - \sigma_{ws} \,. \tag{A.1}$$

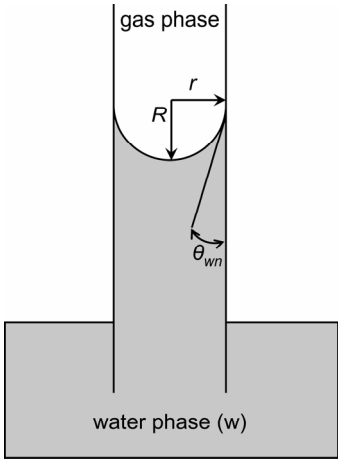

Figure A.2 Capillary rise of water in a capillary tube.

Depending on θ_{wn} we can distinguish three cases:

1. $\theta_{wn} = 0°$: the water phase completely spreads the solid surface and wets the solid.
2. $0° < \theta_{wn} < 90°$: the water phase preferentially wets the solid and water is the wetting phase.
3. $90° < \theta_{wn} < 180°$: the gas phase preferentially wets the solid and gas is the wetting phase.

Based on these situations the wettability of the porous medium can be defined as "the tendency of one phase to spread on or adhere to a solid surface in the presence of other immiscible phases" [*Anderson*, 1986].

As two immiscible phases are in contact then a curved interface exists because of the contact angle. For the two phases present in a vertical capillary tube, with radius r, this is schematized in Figure A.2. The curvature results in a higher pressure in the gas phase and a lower pressure in the water phase. The pressure

difference between the internal pressure and external pressure is known as the capillary pressure and is given by Laplace´s formula

$$P_c = \sigma_{wg}\left(\frac{1}{r_1}+\frac{1}{r_2}\right) \tag{A.2}$$

Where r_1 [m] and r_2 [m] are two mutually perpendicular radii that can be drawn through the surface. Depending on the curvature of the surface the capillary pressure can be positive (water-wet) or negative (gas-wet). In the vertical configuration, as drawn in Figure A.2 there is equilibrium between the capillary forces and the gravity forces, $\Delta\rho gh$, and the capillary rise of the water is over a height h. In Figure A.2 $R = r_1 = r_2$ and from Eq. A.2 it follows that (e.g. *Anderson*, 1987)

$$P_c = \frac{2\sigma_{wg}\cos\theta_{wg}}{r} = \Delta\rho gh \tag{A.3}$$

From Eq. A.3 (Washburn equation) it is clear that the capillary is determined by local pore geometry (r) and the wettability (θ_{wg}).
When our view expands from micro (pore) scale to the macro scale (REV) the capillary pressure is defined as the difference between the average water phase pressure and the average gas phase pressure, given by

$$P_c = P_g - P_w \tag{A.4}$$

At the macro-scale, multi-phase flow phenomena are characterized by the displacement of one phase by another. Displacing the wetting phase with the non-wetting phase is called drainage and imbibition is the reverse process. It appears that that the capillary pressure, as defined in Eq. A.4, must be seen as a function of the total amount of wetting phase present in the porous medium. This leads to the characteristic macro-scale relation for the capillary pressure, the so-called $P_c - S_w$ relationship. A general empirical based expression is described by *Leverett* [1941] and can be written as

$$P_c(S_w) = P_g - P_w = \gamma\sigma_{wg}\sqrt{\frac{\varphi}{k}}J(S_w) \tag{A.5}$$

where φ is the porosity, k [m^2] is the permeability and $J(S_w)$ is the dimensionless capillary pressure, the so-called Leverett-J function. Due to the complex structure and behavior of porous media, even on small scales, different characteristics of the $P_c - S_w$ relationships must be investigated.

The capillary pressure strongly depends on the phases, which are present in the pore space. The surface tension between the phases results in a linear scaling of the capillary pressure curves. Physical and chemical attractiveness of the solid with respect to the phases, defined by the contact angle θ_{wg}, results in the wettability behavior, which have direct influence on the sign of P_c. The pore geometry (see also Eq. A.3) and the connectivity of the pore space, lumped in the permeability, have direct effects on the shape of the $P_c - S_w$ curve. Highly heterogeneous media shows a steep gradient, whereas for homogeneous media the capillary pressure curve is almost horizontal.

The minimum capillary pressure required for the non-wetting phase to invade a porous medium is called the entry pressure or the threshold pressure and is directly related to the largest pores considered. To establish the drainage capillary pressure curve, the wetting phase saturation is reduced from its maximum to its residual minimum, the connate water saturation (S_{wc}). The capillary pressure during this reduction in water saturation is increasing from the entry pressure to a large positive value. At the stage of S_{wc} the bulk wetting phase has been disconnected and will form small coatings on the surface of the grains or will manifest as trapped blobs. The imbibition curve is developed when the wetting phase is re-entering the porous medium and the wetting saturation is increased until the residual stage of the non-wetting phase has been reached. Similar to S_{wc}, the non-wetting phase distribution, present as trapped blobs or arising due to snap-off mechanisms, directly affects the capillary pressure.

During the imbibition process two distinct regions can be measured. The first is the spontaneous imbibition part, where P_c drops to zero. The second part is the forced imbibition curve, where the capillary pressure is decreased from zero to large negative values. Generally, drainage and imbibition are irreversible processes, resulting in capillary hysteresis. The term hysteresis can be defined as the

difference between the drainage P_c and imbibition P_c measured at equal saturations. Between these extremes, scanning curves can be found.
The classical formulation where P_c is only a function of S_w, see Eq. A.5, is considered valid at static conditions. Recent theories have indicated that capillary pressure should be given a more general thermodynamic definition, and its functional dependence should be generalized to include dynamic effects [*Hassanizadeh et al.*, 2002]. This implies that the time dependence of the saturation will have effect on the up-scaled capillary pressure in terms of the phase distribution [need revision].

A.2 Hysteresis in capillary pressure

Capillary pressure hysteresis is extensively investigated and is poorly understood. We have seen that P_c is a function of the saturation, the saturation history, the rate of change in saturation, the pore geometry and wettability and all together these will give the contribution to hysteresis. In literature three different mechanisms are discussed, that cause capillary hysteresis: contact angle hysteresis [*Anderson*, 1987], irreversible redistribution of phases [*Morrow*, 1970; *Hassanizadeh and Gray*, 1993] and interfacial area [*Reeves and Celia*, 1996] Contact angle hysteresis is manifested by the direction of the displacement. The irreversible redistribution of phases is described by Morrow and deals with the preference of the wetting fluid for the smaller pores during drainage and the occupation of the larger pores during imbibition. Dynamic effects arise when the time span is limited for the phases to redistribute, and non-equilibrium situations are considered. Haines jumps illustrate these effects [*Morrow*, 1970].
For the case of hysteresis between drainage and imbibition, *Hassanizadeh and Gray* [1993] found that capillary pressure is seen to be a function of the specific area of the fluid-fluid interface per unit volume, as well as of saturation. They attribute the difference between imbibition and drainage capillary pressure to the increase of the oil/water interface during the entire drainage/imbibition cycle. *Reeves and Celia* [1996] performed network studies, which supports this idea. They found for similar saturations different fluid-fluid areas and ascribe the phenomena for hysteresis to the creation and destruction of interfaces.

A.3 Experimental results on flow rate dependency and dynamic capillary pressure

As discussed in Chapter 2, multi-rate experiments haven been conducted on the coarse sand sample ($360 < D_{50} < 410$) to investigate the flow rate dependency and the validation of assumption 3 (Section 2.3). These experimental results have not been published in one of the papers. However, because our experimental procedure is based on small injection rates (<1 ml/h), such that viscous forces are negligible, we briefly present and discuss these results.

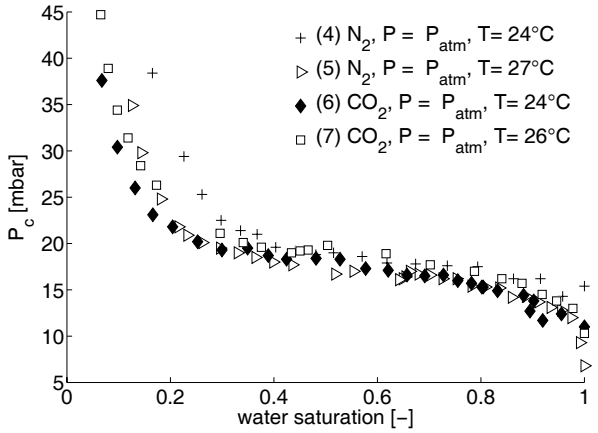

Figure A.3 Primary drainage capillary pressure curves for N_2 and CO_2 injection at atmospheric conditions. Different injection rates are applied during the drainage process and no flow rate dependency is observed.

The assumption that the capillary pressure is measured under quasi-static conditions ($u_{inj} < 0.02\, PV/\ h$) is corroborated by four multi-flow rate experiments for either N_2 (experiment 4 and 5, Chapter 2) or CO_2 injection (experiment 6 and 7, Chapter 2) at atmospheric conditions. These experiments are conducted on four different coarse sand packs. The range of grain size of the coarse sand is $360 < D_{50} < 410\,\mu m$. The results for the primary drainage curves are presented in Figure A.3 and the corresponding gas injection rates as function of S_w are shown in Figure A.4. The applied injection rates are chosen, such that for different parts of the $P_c - S_w$ curves the flow rate dependency can be investigated.

For small injection rates (low Peclet numbers) no dynamic response in the measured capillary pressure is observed Moreover, no relevant effects of changing injection rates on the capillary pressure behavior are noticed for a large water saturation range from near S_{wc} (residual water) to $S_w = 1$ (Figure A.3). Strictly static conditions are considered for approximately 1 hour when the gas injection is stopped for experiment 4 and 7 at $S_w = 0.25$ and $S_w = 0.31$ respectively. Because P_c does not change in this period, this will imply that static conditions can be considered.

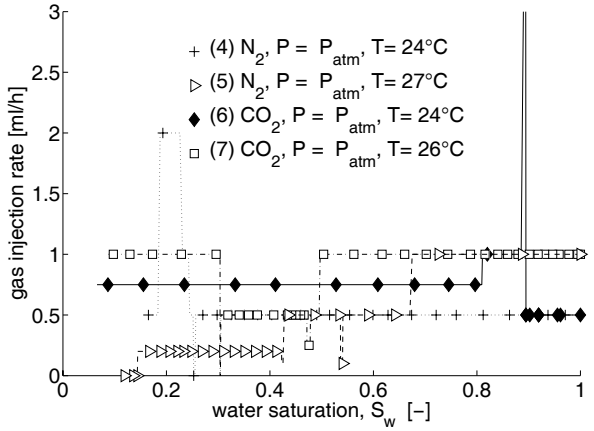

Figure A.4 Injection rates as a function of the water saturation for N_2 and CO_2 primary drainage experiments.

Due to different packing and temperature conditions, the curves in Figure A.3 do not exactly overlap. However, the results are within the precision of the experimental method (see Figure A.4). The peak at $S_w = 0.5$ (experiment 6, Chapter 2) is attributed to an experimental artifact. A difference in connate water saturation is observed between the CO_2 drainage and N_2 drainage experiments. Comparing both the N_2 experiments S_{wc} is 0.16 and 0.11 for respectively experiment 4 and 5. For the CO_2 experiments, the difference in residual water saturation is much smaller, $S_{wc} = 0.06$ and $S_{wc} = 0.08$ for respectively experiment 6 and 7.

The dynamic behavior of the capillary pressure, e.g., described by *Hassanizadeh et al.* [2002], is not implemented in the model, as presented in Appendix C. When we compare the change in S_w with respect to time, for the stages with different injection rates (Figure A.4), we find $\partial S_w / \partial t$ values between 2×10^{-6} and 0.65×10^{-5} for all experiments shown in Figure A.3. For the dynamic expression for the capillary pressure, using $\tau \approx 1 \times 10^{6} - 1 \times 10^{7}$ kg m-1 s-1 [*Hassanizadeh et al.*, 2002], we find that the dynamic part of P_c is 2-65 Pa, which is in between the precision of our experimental method (see Chapter 2.4).

Bibliography

Anderson, W.G. (1986), Wettability Literature Survey- Part 1: Rock/oil/brine interactions and the effects of core handling on wettability, *JPT*, 1125-1144, SPE 13932.

Anderson, W. G. (1987), Wettability literature survey - Part 4: Effects of wettability on capillary pressure, *JPT*, 1283–1300, SPE 15271.

Hassanizadeh, S.M., and W. G. Gray (1993), Thermodynamics basis of capillary pressure in porous media, *Water Resources Research, 29 (10)*, 3389–3405.

Hassanizadeh, S. M., M. Celia, and H. K. Dahle (2002), Dynamic effect in the capillary pressure - saturation relationship and its impacts on unsaturated flow, *Vadose Zone Journal*, *1*, 38–57.

Leverett M. C. (1941), Capillary behavior in porous solids, *Trans. AIME*, *142*, 152-168.

Morrow, N. R. (1970), Physics and thermodynamics of capillary action in porous media, *Ind. Eng. Chem., 62 (6)*, 32–56.

Reeves, P. C., and M. A., Celia (1996), A functional relationship between capillary pressure, saturation and interfacial area as revealed by a pore-scale network model, *Water Resources Research, 32 (8)*, 2345–2358.

Wipfler, E. L. (2003), *Effects of capillarity and heterogeneity on flow of organic liquid in soil*, Dissertation, Wageningen University.

Appendix B Numerical model for the unconsolidated sand-water-CO_2 system

B.1 Introduction

We consider the injection of CO_2 and N_2 in a cylindrical unconsolidated sample, originally filled with water. The sample consists of unconsolidated sand with constant porosity, φ and permeability, k. The sample is vertical, with a height H and a diameter $D_{inner} = 84\,\text{mm}$. The gas inlet is at the top of the sample at $z = 0$, the water inlet is positioned at $z = -L$ and gravity is taken into account.
In Table B.1 the model input parameters are presented which are used in the simulations. Furthermore, the summaries of physical input parameters and variables are given in the nomenclature.

B.2 Model equations of the mathematical model

The conservation of mass of each component in each phase is given by the following equations, which express the liquid water mass balance (Eq. B.1), the gas mass balance in the gaseous phase (Eq. B.2) and the combined gas mass balance in the liquid water and the water vapor in the gaseous phase (Eq. B.3)

$$\frac{\partial}{\partial t}\left(S_w c_{wg}\right) + \frac{\partial u_w c_{wg}}{\partial z} - D_g \frac{\partial^2 c_{wg}}{\partial z^2} = -q_{g\to g,w} \tag{B.1}$$

$$\frac{\partial}{\partial t}\left(S_g c_{gg}\right) + \frac{\partial u_g c_{gg}}{\partial z} = q_{g\to g,w} \tag{B.2}$$

$$\frac{\partial}{\partial t}\left(S_g c_{gw}\right) + \frac{\partial u_g c_{gw}}{\partial z} + \frac{\partial}{\partial t}\left(S_w c_{ww}\right) + \frac{\partial u_w c_{ww}}{\partial z} = 0 \tag{B.3}$$

In these equations S_w is the water saturation and S_g is the gas saturation. Furthermore u_w and u_g is the Darcy velocity of the water and the gas respectively and $q_{g\to g,w}$ is the mass transfer between the gas phase and the liquid water (see Eq. B.9). The component concentration is denoted by $c_{\alpha j}$, where α denotes the phase ($\alpha = w, g$) and j is the component ($j = w, g$). This system of equations is solved for S_w, P_g and c_{wg} using the relations described in Appendix B.3.

B.3 Model assumptions

The following model assumptions for the quasi 1-D model are made:

1. temperature is constant over the experimental time.
2. for the initial condition, equilibrium water saturation is present such that the gas and water velocities are zero.
3. only vertical flow is considered.
4. for the drainage process gas is injected as pure gas.
5. two components are present in the sample: the water (w), and gas (g) component.
6. for N_2 the ideal gas law is used and for CO_2 the Span and Wagner EOS [*Span and Wagner*, 1996] is used.
7. thermodynamic equilibrium between the water component in the water and gas phase is considered.
8. the volume of water and gas are additive, i.e., there is no volume contraction upon mixing.
9. mass transfer for the gas component in the gas and water phase is considered.
10. no interaction between the solid and mobile phases is taken into account.
11. the water and the rock are incompressible.

B.4 Constitutive relations

The volumetric flux of phase α is given by Darcy's law, which reads

$$u_\alpha = -\frac{kk_{r\alpha}}{\mu_\alpha}\left(\frac{\partial P_\alpha}{\partial z} - \rho_\alpha g\right) \tag{B.4}$$

In Eq. B.4, the viscosity of the gas component, μ_g is a function of P and T (Table A.1) and the water viscosity, μ_w is a function of T (Eq. B.20). The phase pressures and densities are denoted by P_α and ρ_α (see nomenclature) respectively.

The absolute permeability, k, is obtained from the Carman-Kozeny equation, and given by

$$k = \frac{1}{150}(D_{50})^2 \frac{\varphi^3}{(1-\varphi)^2} \tag{B.5}$$

where φ (Table B.1) and D_{50} are respectively the sample porosity and the average grain size. The relative permeability functions k_{rw} and k_{rg} are given by the Brooks-Corey functions,

$$\begin{aligned} k_{rw} &= k'_{rw}\left(S_{we}\right)^{\frac{2}{\lambda_s}+3} \\ k_{rg} &= k'_{rg}\left(1-S_{we}\right)^2\left(1-\left(S_{we}\right)^{\frac{2}{\lambda_s}+1}\right) \end{aligned} \tag{B.6}$$

Here the effective water saturation, S_{we}, is defined as

$$S_{we} = \frac{S_w - S_{wc}}{1-S_{wc}} \tag{B.7}$$

The capillary pressure is defined as $P_c = P_g - P_w$, and derived from the Leverett-J function,

$$P_c\left(S_w\right) = \gamma\sigma\sqrt{\frac{\varphi}{k}}\left(\frac{\frac{1}{2}-S_{wc}}{1-S_{wc}}\right)^{\frac{1}{\lambda_s}}\left(\frac{S_w - S_{wc}}{1-S_{wc}}\right)^{-\frac{1}{\lambda_s}} \tag{B.8}$$

where the interfacial tension and the connate water saturation are respectively denoted by σ (Table B.1) and S_{wc} (Table B.1). For N_2 it is assumed that σ does not vary for the pressure range from 1 to 10 bar and for CO_2 the interfacial tension changes as function of pressure and temperature. During the simulation, σ for N_2 and CO_2 remains constant.

The dissolution rate of gas in water, $q_{g\to g,w}$ (Eq. B.1 and Eq. B.2), is a function of the gas saturation, S_g, the actual gas concentration in the water, c_{wg}, and the equilibrium gas concentration in the water, c_{wg}^{eq}, and is defined by

$$q_{g\to g,w} = k_L S_g \left(c_{wg} - c_{wg}^{eq}\right) \tag{B.9}$$

where k_L is the mass transfer for the dissolution of gas in the water defined by *Bird et al.* [1960],

$$k_L = D_g \frac{12}{\left(D_L\right)^2} \tag{B.10}$$

Here D_g is the diffusion coefficient of the gas in liquid water as function of T [*Gmelin*, 1973] and D_L is the characteristic length of the bubble size. We determine the equilibrium concentration of the gas in the liquid water, c_{wg}^{eq}, from Henry's law, given by

$$P_g = K_{Henry} x_{gw} \tag{B.11}$$

The Henry's constant is denoted by K_{Henry} and x_{CO_2} is the molar fraction, defined as

$$x_{CO_2} = \frac{c_{wg}^{eq}}{c_{www} + c_{wg}^{eq}} \tag{B.12}$$

Since ideal mixing [*Bruining and Marchesin*, 2006] is assumed in this work, and enthalpy changes due to mixing of the components are zero, the volumes of the components are additive,

$$\begin{aligned} \frac{c_{ww}}{c_{wW}} + \frac{c_{wg}}{c_{wG}} &= 1, \\ \frac{c_{gw}}{c_{gW}} + \frac{c_{gg}}{c_{gG}} &= 1, \end{aligned} \tag{B.13}$$

where subscripts W and G indicate the concentrations of the pure components. Both N_2 and vapor water are assumed to behave as an ideal gas, whereas for CO_2 non-ideal behavior is assumed (Eq. B.16). The ideal gas law is given by

$$PV = nRT, \tag{B.14}$$

in addition the pure concentrations of water and N_2 can therefore be written as

$$c_{gW} = \frac{P_g}{RT}, \quad c_{gG} = \frac{P_g}{RT} \tag{B.15}$$

where P_g is the total gas pressure, M_W, M_{N_2} are the molecular weights of water and N_2 respectively, and R is the universal gas constant. For CO_2 we use the Span and Wagner equation of state [*Span and Wagner*, 1996] and the pure CO_2 component can be written as,

$$c_{gG} = \frac{P_g}{z(P,T)RT} \tag{B.16}$$

where $z\left(P,T\right)$ is the gas compressibility of CO_2. From Eq. B.13, c_{gw} is determined from

$$c_{gw} = \frac{P_{w,sat}}{RT} \tag{B.17}$$

where the water vapor pressure, $P_{w,sat}$, is only a function of temperature, T (Eq. B.21).

The input parameters used for the numerical simulations are summarized in Table B.1. In each simulation, the sand column is discretized into 10 layers. The characteristic length used for the mass transfer coefficient, k_L, is chosen as $D_L = 0.01$ m (Eq. B.10). The input capillary pressure curves are obtained from a least square curve fitting procedure, from which we estimate the coefficients, S_{wc}, γ and λ_s of the Leverett-J function, given by Eq. B.8, using the experimental

$P_c - S_w$ (see Table B.1). The values for S_{wc}, λ_s and γ are adjustable model parameters and vary because different sand packing are used for each experiment. The capillary pressure, comparable to the measured capillary pressure, is derived from the pressure difference of the bulk phases and represented by

$$P_c = \left(P_{g,z=0} + \frac{\rho_g g H}{2}\right) - \left(P_{w,z=-L} - \frac{\rho_w g H}{2}\right). \tag{B.18}$$

The hydrostatic pressure correction for $P_{g,z=0}$ and $P_{w,z=-L}$ is due to placement of the PDT device in the experimental setup (see Section 2.2.1 and Figure 2.1).

B.5 Temperature and pressure dependent properties of N_2, CO_2 and water

The liquid water density, $\rho_w(T)$, viscosity, $\mu_w(T)$ and the water vapor pressure, $P_{w,sat}(T)$ are obtained from *Tortike and Farouq* [1989] (see also *Bruining and Marchesin* [2006]), and are respectively given by

$$\begin{aligned}\rho_w(T) &= 3786.31 - 37.2487T + 0.196246T^2 - 5.04708\times10^{4-}T^3 + \\ &+6.29368\times10^{-7}T^4 - 3.08480\times10^{-10}T^5,\end{aligned} \tag{B.19}$$

$$\begin{aligned}\mu_w(T) = -0.0123274 &+ \frac{27.1038}{T} - \frac{23527.5}{T^2} + \frac{1.01425\times10^7}{T^3} \\ &- \frac{2.17342\times10^9}{T^4} + \frac{1.86935\times10^{11}}{T^5}\end{aligned} \tag{B.20}$$

and

$$P_{w,sat}(T) = 103\begin{pmatrix}-175.776 + 2.29272T - 0.0113953T^2 + \\ +2.6278\times10^{-5}T^3 + 2.73726\times10^{-8}T^4 + 1.13816\times10^{-11}T^5\end{pmatrix}^2 \tag{B.21}$$

B.6 Boundary conditions

Two sets of boundary conditions are considered for the drainage process:

- a constant gas injection rate at $z = 0$ and a constant water pressure at $z = -L$.
- a constant gas pressure at $z = 0$ and a constant water extraction rate at $z = -L$.

The volume change of the gas injection pump is incorporated using the expression

$$\frac{1}{M}\frac{\partial \rho_{G,p} V_p}{\partial t} + A\left[c_{GG} u_g\right]_{z=0} = 0, \tag{B.22}$$

where $\rho_{G,p}$ is the density of the gas phase in the pump, V_p is the gas volume and A the sample area. Dependent on the boundary conditions, constant CO_2 injection or constant CO_2 pressure, we solve Eq. B.22 for $P_{g,p}$ or V_p respectively. Moreover, $u_w = 0$ at $z = 0$ and $u_g = 0$ at $z = -L$.

Exp	T [°C]	P [bar]	$k_{rw,a}$ [-]	$k_{rg,a}$ [-]	λ_s [-]	σ [mN/m]	φ [-]	γ [-]	S_{wc} [-]	D_{50} [μm]	D_L [m]
4	24	1	0.5	1	3.84	71	0.37	0.51	0.1	400	0.01
6	24	1	0.5	1	3.56	71	0.37	0.45	0.01	400	0.01
10	28	8	0.5	1	7.32	67	0.38	0.49	0.075	400	0.01
11	27	8	0.5	1	6.18	71	0.37	0.46	0.075	400	0.01
12	27	85	0.5	1	5.87	30	0.37	0.65	0.03	400	0.01

Table B.1 Input parameters for numerical simulation.

Bibliography

Bird, R. B., W. E. Steward, and E. N. Lightfoot (1960), *Transport Phenomena*, John Wiley and Sons, New York.

Bruining, J., and D. Marchesin (2006), Analysis of nitrogen and steam injection in a porous medium with water, *Transport in Porous Media, 62*, 251–281.

Duan, Z., and R. Sun (2003), An improved model calculation CO_2 solubility in pure water and aqueous NaCl solutions from 273 to 533 K and from 0 to 2000 bar, *Chem. Geology, 193*, 257–271.

Gmelin, L. (1973), Gmelin Handbuch der Anorganischen Chemie, 8. Auflage Kohlenstoff, Teil C3, Verbindungen.

Hassanizadeh, S. M., M. Celia, and H. K. Dahle (2002), Dynamic effect in the capillary pressure-saturation relationship and its impacts on unsaturated flow, *Vadose Zone J., 1*, 38–57.

Tortike, W. S., and S. M. Farouq Ali (1989), Saturated-steam-property functional correlations for fully implicit reservoir simulation, *SPE Res. Eng., 4 (4)*, 471–474, SPE 17094-PA.

Span, R., and W. Wagner (1996), A new equation of state for carbon dioxide covering the fluid region from the triple-point temperature to 1100 K at pressures up to 800 MPa, *J. Phys. Chem. Ref. Data*, *25 (6)*, 1509–1596.

Appendix C Theory for the impedance measurements

In this section a brief description and explanation is given for the error analysis of the impedance tool and the data analysis method as used in chapter 4 and 5. Different procedures are presented and investigated to analyze the experimental data including the layout of the impedance tool.

C.1 Theory for determination of the electrical permittivity in porous media

The experimental complex permittivity, ε_s^*, is obtained considering the sample holder as a parallel plate capacitor (see Figure C.1). A capacitor is an electric device constituted by two parallel metallic plates (denoted by b, Figure C.1) separated by a distance d, which is small compared with the width, D, of the plates (stainless steel perforated plates, see Figures C.1 and 4.2).

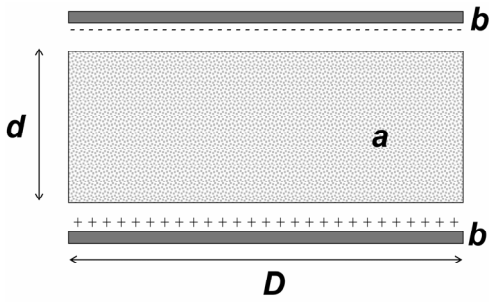

Figure C.1 Schematic layout of a parallel plate capacitor: a is the insulator (sample), b are the metallic plates (in the experimental set-up, Chapter 4, the top plate is the perforated plate and the bottom plate the SIPERM filter), D is the width and d is the separation distance between the capacitor plates.

In between the plates, an electrical insulator or dielectric (denoted by a) is placed. In this work the insulator can be: air, Teflon, PVC, 1-butanol, 1-decanol and ethanol, used as calibration samples (Chapter 4.4), or unconsolidated quartz sand, filled with water and gas (CO_2 and N_2), the media where our interests is in (see

Chapter 4 and 5). The two parallel plates store an electric opposite charge when a potential difference is applied. The electrons are transported from one plate to the other and therefore charging the capacitor or storing energy at the surface of the plates. Moreover, the potential difference or voltage applied is the work per unit charge required to transport charge from one plate to another and is given by,

$$V = \frac{d}{\varepsilon_0 A} Q \tag{C.1}$$

where Q is the total charge on each plate, A $(= \frac{1}{4}\pi D^2)$ is the area of the plates, and d [m] is the separation distance. It is evident that the potential difference applied is proportional to the charge of the capacitor, and this proportional coefficient is defined as the complex capacity C^* [F] of the capacitor, defined as

$$C^* = \frac{\varepsilon_0 \varepsilon_s^* A}{d} \tag{C.2}$$

where ε_0 is the dielectric constant of the free space ($\varepsilon_0 = 8.854$ F/m) and ε_s^* [-] is the complex electric permittivity of the material placed between the parallel plates (see Chapter 4), defined by $\varepsilon_s^* = \varepsilon'_s - i\varepsilon''_s$. The complex notation of the capacitance and the permittivity is a result of the frequency dependence of the material. This frequency dependence reflects the fact that a material's polarization does not respond instantaneously to an applied electric field. Here ε'_s and ε''_s represent the real and imaginary part of the permittivity respectively. The imaginary part of the permittivity is related to the rate at which energy is absorbed by the medium, i.e., the loss factor. It is clear from relationship C.2 that a material with $\varepsilon_s^* > \varepsilon_0$ will increase the capacitance, C^*, with a factor ε_s^* with respect to the free space. This factor ε_s^* depends only on the electrical nature of the material.

In the experimental set-up, the amplitude of the complex impedance, $|Z|$ [Ω], and the phase angel θ [rad] are measured as a function of the frequency, f [Hz]. The impedance is defined as the ratio between the voltage and the current applied across the capacitor.

The time varying current, $i_c\left(t\right)$, is represented by

$$i_c\left(t\right) = C^* \frac{dv_c\left(t\right)}{dt} \tag{C.3}$$

where, $v_c\left(t\right)$ is the time varying potential difference applied to the capacitor and t is the time. We can rewrite Eq. C.3 in phase notation. Therefore, let $v_c\left(t\right)$ be a sinusoidal voltage signal expressed by

$$v_c\left(t\right) = V_c \cos\left(\omega t + \theta\right) \tag{C.4}$$

Here θ [rad] is the phase angle and ω is the angular frequency, defined by $\omega = 2\pi f$. Applying Euler's[1] identity for Eq. C.4 yields the phase representation of the sinusoidal voltage

$$V = V_c \exp i\left(\omega t + \theta\right) \tag{C.5}$$

The current $i_c\left(t\right)$ can be expressed as

$$i_c\left(t\right) = I_c \exp i\left(\omega t + \theta\right) \tag{C.6}$$

and substitution of Eq. C.5 and Eq. C.6 in Eq. C.3 yields

$$I_c = C^* i\omega V_c \tag{C.7}$$

Finally, the expression for the complex impedance, Z^*, as the ratio between the voltage and current is given by

$$Z^* = \frac{V_c}{I_c} = \frac{1}{i\omega C^*}. \tag{C.8}$$

[1] Euler's identity: $V_c e^{i(\omega t+\theta)} = V_c \cos\left(\omega t + \theta\right) + i V_c \sin\left(\omega t + \theta\right)$

The (complex) impedance and the electric permittivity can now be related as follows

$$Z^* = \frac{1}{i\omega}\frac{d}{\varepsilon_0 \varepsilon A}. \tag{C.9}$$

C.2 Model for the experimental set-up

The measured impedance amplitude, $|Z|$, and phase angle, θ, apply to the total sample holder that consists of the PEEK ring and the sample inside the ring. To determine the effective permittivity, ε_s^*, of the sample from $|Z|$ and θ, the sample holder is considered as two parallel plate capacitors in a parallel array (see Figure C.2). The first capacitor (C_1) applies to the porous medium as insulator, whereas the second capacitor (C_2) applies to the PEEK-ring. A schematic of the two capacitors is shown in Figure C.2 (electrical circuit) and Figure C.3.

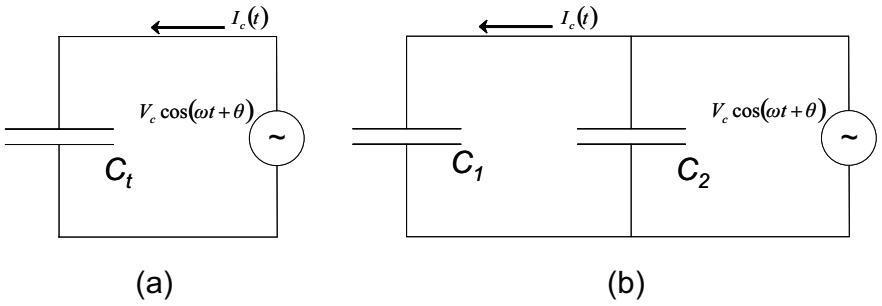

Figure C.2 The electrical circuit for the 'total' capacitor, C_t (a) and the electrical circuit for the two parallel plate capacitors C_1 (applies to the sample) and C_2 (applies to the PEEK ring and the additional capacitances, due to background noise, the electrodes etc.).

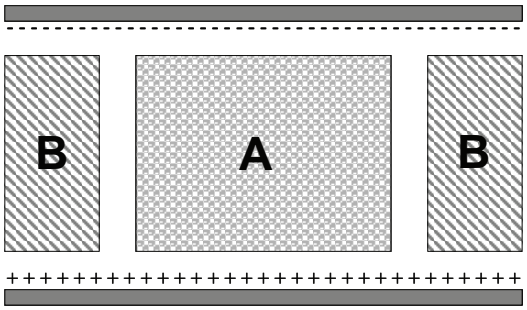

Figure C.3 Schematic cross section for the 2 capacitors: A denotes the sample and B denotes the PEEK ring.

To obtain the right value for the permittivity, ε_s^*, the different unknowns and uncertainties of the experimental procedure and analysis procedure must be investigated. The latter are due to the background noise of the electric devices, the capacitance of the connection cables and the physical layout of the PEEK-ring. In this thesis, we assume that these uncertainty effects are all lumped in the second capacitor, C_2 (see Eq. 4.1 in Chapter 4 where C_2 is denoted as $C^*_{residual}$).
The model that is used in Chapter 4 and 5, to obtain the electric permittivity from the impedance measurements deals with two unknowns, ε_s^* and $C^*_{residual}$.
As described above, the capacitor configuration results in a parallel circuit (see Figure C.3) for which the total complex capacitance C^* is considered as the sum of the capacitance of the sample, C_s^* ($C_s^* = C_1$, Figure C.2), the PEEK ring (C^*_{PEEK}), the cables (C^*_{cables}), the electrodes design ($C^*_{electrodes}$) and the background noise (C^*_{noise}). Under the assumption that only $C^*_{residual}$ is changing for different samples, the total capacitance, C^* (Figure C.3a), can be written as

$$C^* = C^*_{s1} + C^*_{residual} = \frac{\varepsilon_0 \varepsilon_s^* A_s}{d} + C^*_{residual} \tag{C.10}$$

C.3 Measurement and system accuracy

To obtain the experimental accuracy, measurements are conducted for the capacitor filled with the 7 calibration material. For each material the measurement is repeated 50 times. In Figure C.4 and C.5 the mean of $|Z|$ and θ for the 50 measurement are shown together with the upper and lower bound of the accuracy

of the apparatus (Precision Component Analyzer 6440A, Wayne Kerr Electronics). The straight lines in Figure C.4 indicate loss free materials for all samples except for ethanol (<200 kHz), Butanol (< 30 kHz) and decanol (< 500 Hz). Moreover, the measurement data for the impedance amplitude is within the limits of the measurement range of the component analyzer for $f>3$ kHz (see Chapter 4.4).

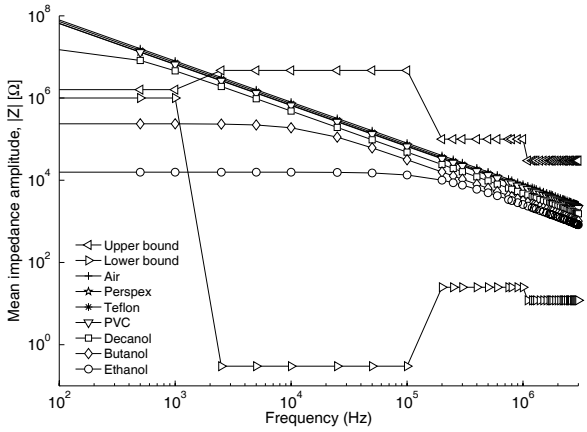

Figure C.4 $|Z|$ as function of the frequency for 7 calibration materials. The lower and upper bound represents the accuracy range of the component analyzer.

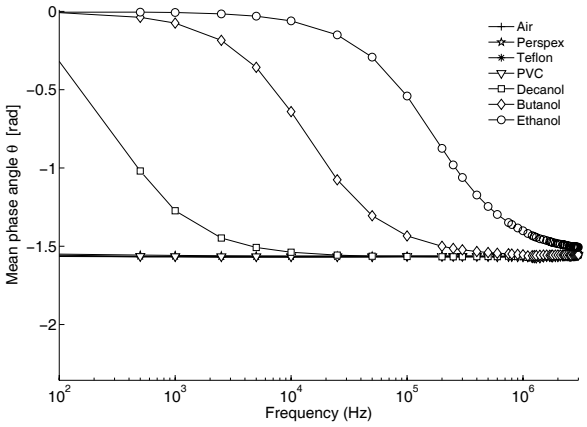

Figure C.5 θ as function of the frequency for 7 calibration materials. The minimum value is $-\pi / 2$, indicating a loss free material.

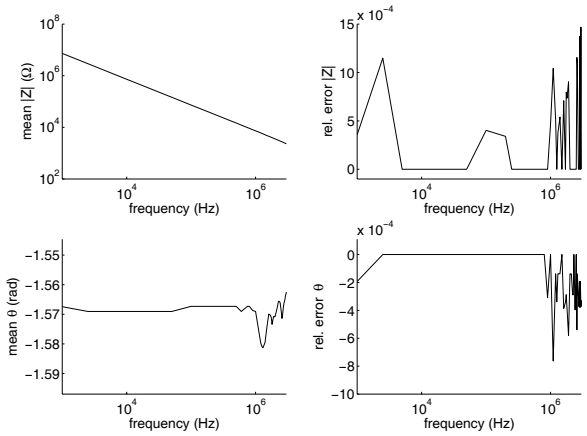

Figure C.6 The mean and relative error for 10 groups of 2 Teflon measurements for the impedance amplitude $|Z|$ and the phase angle θ [rad]. The straight line and the average phase angle of approximately $\theta = -\pi / 2$ indicate that no loss terms are measured. The relative error is of the order of 0.1%

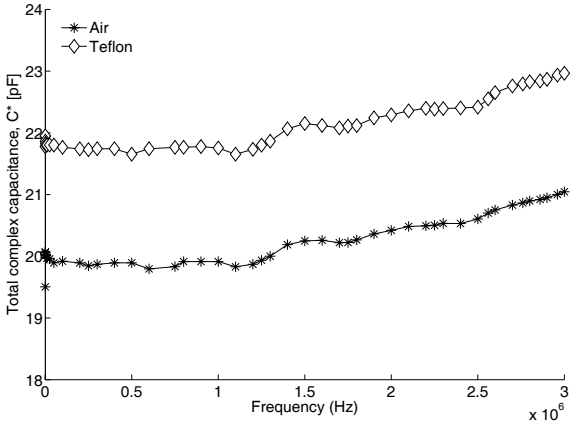

Figure C.7 C^* as function of the frequency for air and Teflon samples.

A statistical analysis with either air or Teflon, as described by *Gorriti and Slob* [2005] is performed where the relative error for $|Z|$ and θ is determined of ten

groups of two measurements. Air and Teflon are suitable, because the loss factor for both air and Teflon is zero and ε'_s is known (1 for air and 2.76 for Teflon). The results of the statistical analysis for air are shown in Figure in 4.4. In Figure C.6, the results for Teflon are presented. In Figure C.7, the values for C^* are shown for measurements with Air and Teflon, which are used for the data analysis procedure as described in the next section. The quantity on the y-axis is the mean of the 50 measurements.

C.4 Data analysis procedure for the (un)saturated sand samples

The first step is to obtain ε_s^* for the value for the (un) saturated samples is determining $C^*_{residual}$, by solving Eq. C.10 using the theoretical values of ε' for air (=1) and Teflon (=2.76). Assuming that $d = 27$ mm (see Figure 4.2) and $A_{sample} = \frac{1}{4}\pi D^2$ (with $D = 84\,\text{mm}$), the theoretical shape factor of C_s^* is $A/d = 0.2053\,\text{m}$. This factor can be evaluated experimentally using the air and Teflon measurements. Division of the capacitances of the two measurements gives

$$\frac{C^*_{air,measurement}}{C^*_{Teflon,measurement}} = \frac{C_{Teflon} + C^*_{residual}}{C_{air} + C^*_{residual}} \tag{C.11}$$

Substitution of $C_{air} = \dfrac{\varepsilon_0 A}{d}$ and $C_{Teflon} = \dfrac{\varepsilon_0 \varepsilon'_{Teflon} A}{d}$ in Eq. C.11 yields

$$\frac{A}{d} = \frac{\left(C^*_{air,measurement} - C^*_{Teflon,measurement}\right)}{\varepsilon_0 - \varepsilon'_{Teflon}\,\varepsilon_0} \tag{C.12}$$

In Figure C.8, the values for A/d are plotted as a function of frequency and compared to the theoretical value (0.2053 m). It is clear that the theoretical value of A/d is sufficient to use for the data analysis.

Under the assumption that for each measurement, regardless of the sample considered, the error remains constant (read $C^*_{residual}$), we can solve Eq. C.10 for ε_s^*. The first step is using C^* (Figure C.7) and the theoretical A/d to compute $C^*_{residual}$ from Eq. C.10. For ε_s^* we either use 1 (air) or 2.76 (Teflon). In Figure C.9, the results for $C^*_{residual}$ are shown. For the frequency range considered, the two

curves coincide. The experimental results as presented in Chapter 4 and 5, are analyzed using $C^*_{residual}$ as derived with air.

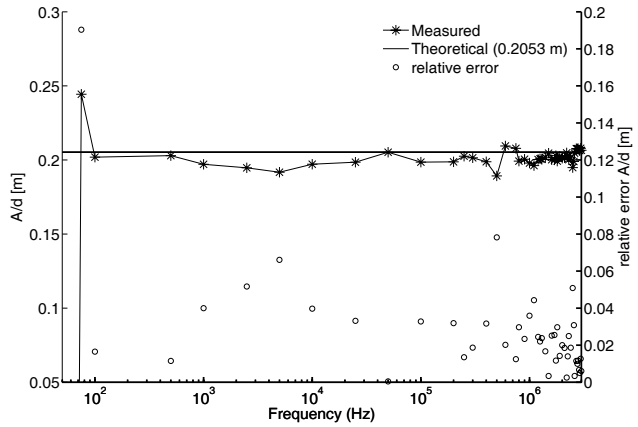

Figure C.8 The measured and theoretical A/d as function of the frequency. The relative is less than 0.08.

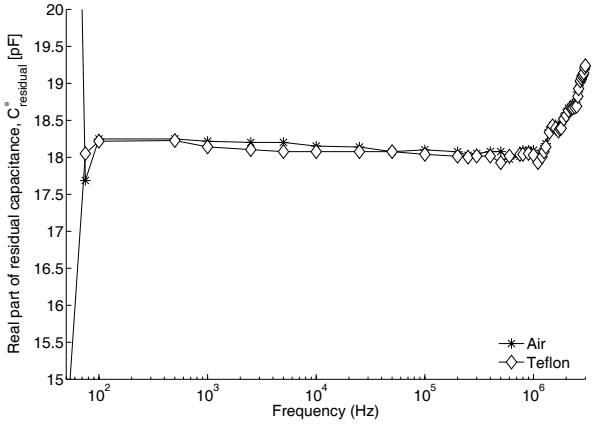

Figure C.9 The values for the real part of the residual complex capacitance measured with air and Teflon.

Bibliography

Gorriti, A. G. and E. C. Slob (2005), A new tool for accurate S-parameters measurements and permittivity reconstruction, *IEEE Transactions on Geoscience and Remote Sensing*, *43*, 1727-1735.

Weast, R. C., and M. J. Astle (1981), *CRC Handbook of Chemistry and Physics,* 62nd ed., CRC Press., Boca Raton, Florida.

Appendix D Experimental set-up

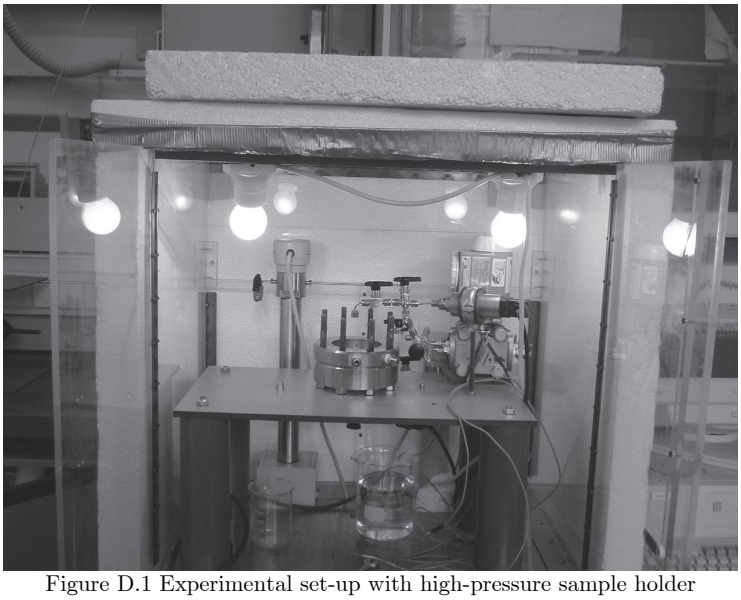

Figure D.1 Experimental set-up with high-pressure sample holder

Figure D.2 The Network analyzer (Wayne-Kerr) used for impedance measurements.

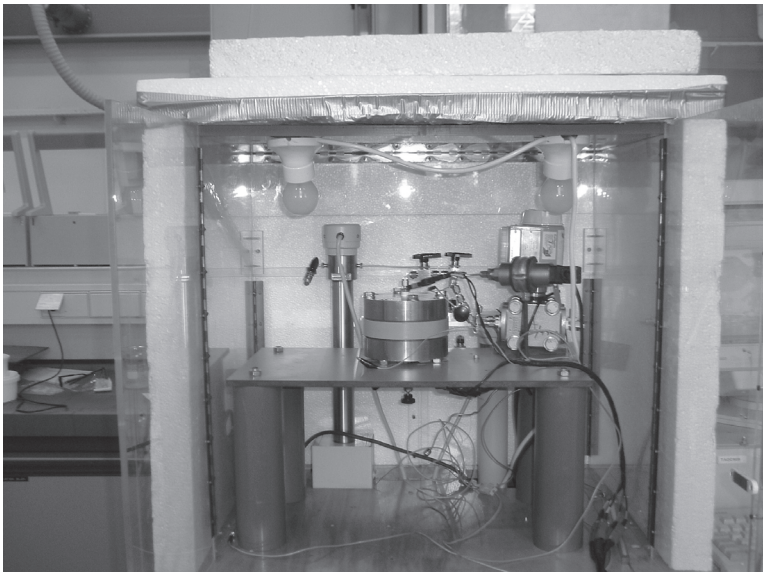

Figure D.3 Experimental set-up: the sample holder with the PEEK ring.

Figure D.4 The sample holder as parallel plate capacitor (with PEEK ring).

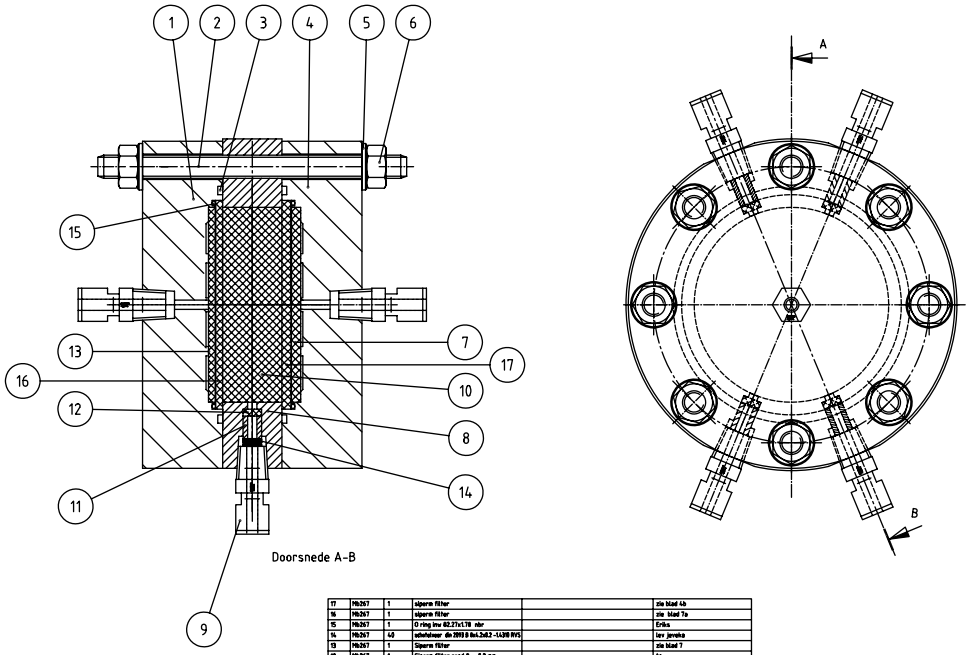

17	Hb267	1	sipeon filter		zie blad 4b
16	Hb267	1	sipeon filter		zie blad 7a
15	Hb267	1	O-ring inw 62.27x1.78 nbr		Eriks
14	Hb267	40	schotelveer do 2010 B 6x1.2x0.2 -1430 RVS		ter jonske
13	Hb267	1	Sipeon filter		zie blad 7
12	Hb267	1	Sipeon filter rond 8 -0.2 mm		fa
11	Hb267	4	Bus		zie blad 6
10	Hb267	1	Mantel		fa
9	Hb267	6	Koppeling SS-400-1-4		swagelok
8	Hb267	1	Ring		zie blad 5
7	Hb267	1	sipeon filter		zie blad 4a
6	Hb267	8	Moer M16		RVS
5	Hb267	8	Sluitring rond 16		RVS
4	Hb267	1	deksel		zie blad 3
3	Hb267	2	O-ring inw 94.92x2.62 viton		eriks
2	Hb267	8	draadstnd M16x150		Bohler V320
1	Hb267	1	Bodem		zie blad 2
Pos	Partslist Name	Quantity	Description 1	Standard/Supplier 1	Material 1
			Description 2	Standard/Supplier 2	Material 2
			ID Number	Price	Mass

Figure D.5 Schematic of the stainless steel sample holder as used for high-pressure experiments (Chapter 2 and 3).

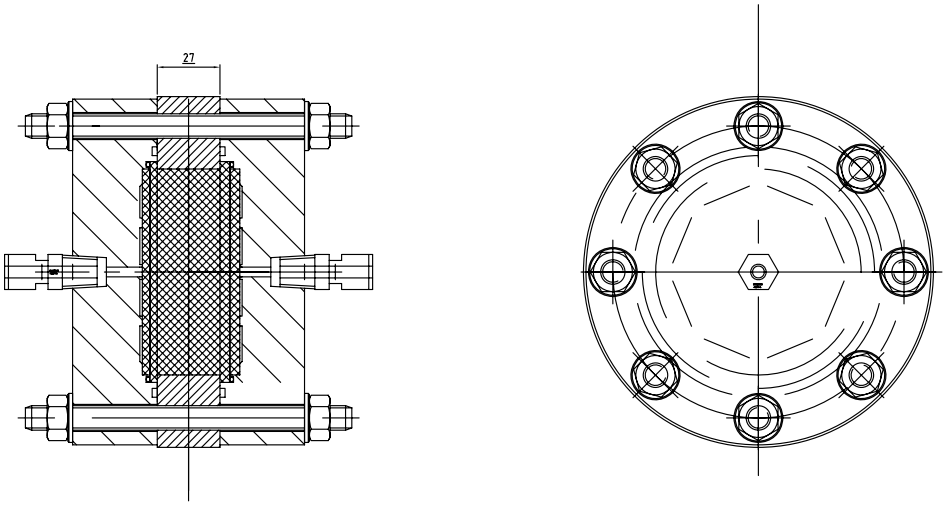

Figure D.6 Schematic of the impedance tool with the PEEK ring ($H = 27$ mm) as used for the permittivity measurements (see chapter 4 and 5).

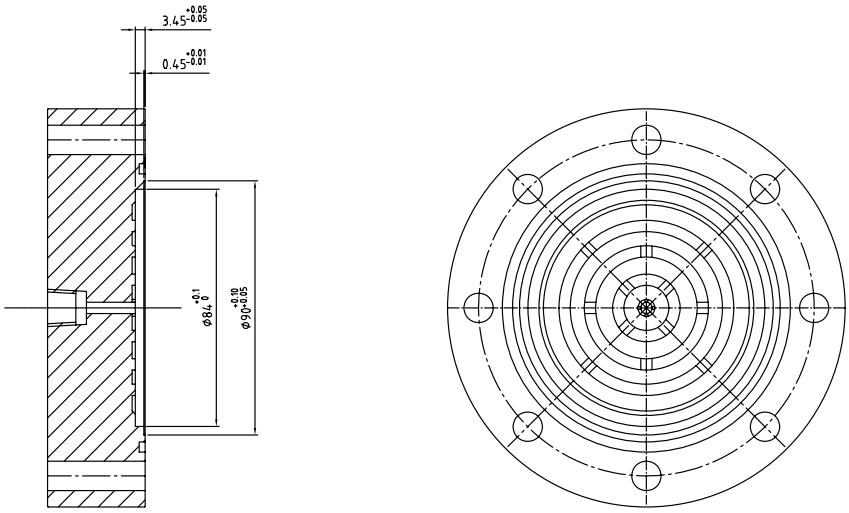

Figure D.7 Details of the concentric flow grooves in the top and bottom end-pieces of the sample holder.

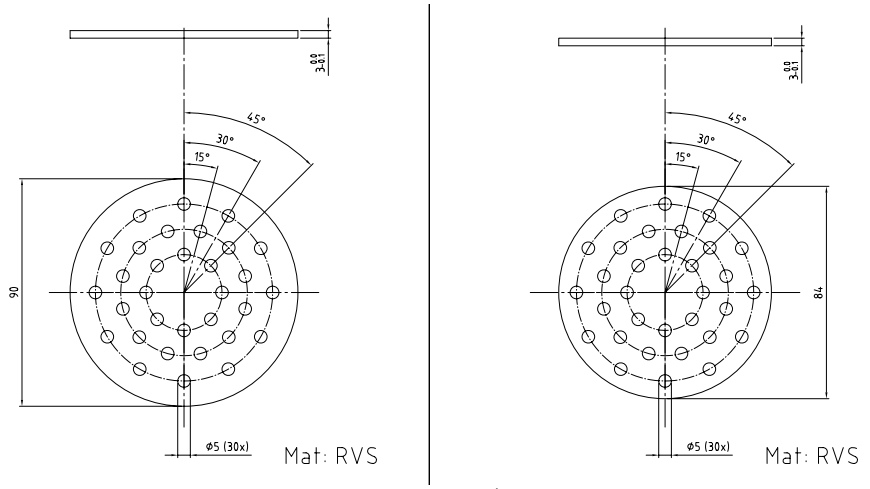

Figure D.8 Schematic of the perforated plates (left the perforated plate with diameter $D_{ss,1} = 90\,\text{mm}$, right the perforated plate with diameter $D_{ss,2} = 84\,\text{mm}$).

Appendix E Output list

2003

Saikat Mazumder, Willem-Jan Plug, Hans Bruining, *Capillary Pressure and Wettability Behavior of Coal – Water – Carbon dioxide System*, SPE 84339, Presented at: SPE Annual Meeting, Denver Colorado, 2003.

Plug, W.J., *Evaluation and applicability of different effective medium formulas for heterogeneous porous media*, Oral Presentation Scientific meeting, 27-2-2003, Delft.

2004

Mazumder, S., W-J Plug, & J. Bruining, "*Capillary Pressure and Wettability Behavior of Coal – Water – Carbon dioxide System*", Proceedings of the International Congress on Carboniferous and Permian Stratigraphy, Under review for MS ICCP-XV-5, 2004.

W-J. Plug, S. Mazumder, H. Bruining, *Capillary Pressure and Wettability Behavior of a Coal-Water-Gas System under Variable Pressure Conditions*, GRC, 2004, Oxford, presented as poster.

Plug, W.J., *Fundamentals of Capillary Pressure Hysteresis in Porous Media,* Oral Presentation Scientific meeting, April 2004, Delft.

Plug, W.J., *Measurements of Capillary Pressure at High Pressures: Determination of Wetting Alteration in Porous Media,* 1-4-2004, Shell.

Plug, W.J., *Evaluation and applicability of different effective medium formulas for heterogeneous porous media*, 17-6-2004, presentation Shell, Rijswijk.

2005

Presentation Scientific meeting, January 2005, Delft: *Capillary pressure, wettability and dielectric behavior in various porous media.*

Plug, W.J., SKB, June 2005: poster presentation: *Simultaneous Measurements of Capillary Pressure and Dielectric Properties in Porous Media.*

Plug, W.J. *Capillary Pressure and Wettability Behavior of the Coal-Water-Carbon Dioxide System under Various Pressure and Temperature Conditions, Poster presentation Workshop: "Upscaling Flow and Transport Processes in Porous Media*, 11-13 July 2005 in Zeist.

Presentation ECBM workshop, November 2005, Delft: *Wettability and capillary pressure behavior for the coal-water-CO_2 system in Unconsolidated coal samples.*

Poster, ECBM workshop, November 2005, Delft: see above.

Presentation Scientific meeting, November 2005, Delft: *dynamic capillary pressure and wettability properties in porous media.*

2006

Plug, W.J., Mazumder, S., Bruining, J., Siemons, N. and K.H. Wolf, *Capillary Pressure and Wettability Behavior of the Coal-Water-Carbon Dioxide System at High Pressures*, paper no. 606, Proceedings of the International Coalbed Methane Symposium, Tuscaloosa, Alabama, 2006.

Wolf, K-H.A.A., J. Bruining, S. Harpalani, D. Bossie-Codreanu, A. Busch, J-Q. Shi, F. van Bergen, D. Prinz, N. Siemons, S. Mazumder, P. van Hemert, W. J. Plug, A. Kumar, *CO_2-ECBM DEVELOPMENTS IN EXPERIMENTS AND THEORY,* paper no. 639, Proceedings of the International Coalbed Methane Symposium, Tuscaloosa, Alabama, 2006.

Plug, W.J., Bruining, J., Slob, E.C. and A.G. Gorriti, *Numerical Validation of Various Mixing Rules Used for Up-Scaled Geo-Physical Properties*, Proceedings of CMWR XVI, Copenhagen, 2006.

Plug, W.J., Mazumder, S., Bruining, J., Title of the poster: "*Pressure and Wettability Behavior of the Coal-Water-Carbon Dioxide System at High Pressures"*, 2nd CATO-day, June 9, 2006, Utrecht, poster presentation. Winner of best poster award.

Contribution presentation prof.dr.ir. S.M. Hassanizadeh, Berlin 2006.

Moreno, L.M., Plug, W.J., *Simultaneous Measurements of Capillary Pressure and Dielectric Constant in Porous Media*, SKB Bodemdiep June 2006, Zeist.

Plug, W.J., Bruining J., Mazumder, S., *Capillary Pressure and Wettability Behavior of the Coal-Water-Carbon Dioxide System at High Pressures*, SKB Bodemdiep June 2006, Zeist.

Moreno, L.M., *Simultaneous Measurements of Capillary Pressure and Dielectric Constant in Porous Media from 50 Hz to 3 MHz*, master thesis, September 2006.

Lecture PGK. (Petroleum Geologische Kring), 15 November 2006.

Plug, W.J., Mazumder, S., Bruining, J., *Capillary Pressure and Wettability Behavior of the Coal-Carbon Dioxide-Water System at High Pressures*, submitted to SPE Journal, November 2006 (under review).

2007

Plug, W.J., Moreno, L.M., Bruining, J., Slob, E.C., *Simultaneous Measurement of Capillary Pressure and Dielectric Constant in Porous Media*, Proceedings of PIERS 2007, Beijing. (reviewed conference paper).

Plug, W.J., Bruining, J., L.M. Moreno, E. Slob (2007), *Simultaneously measured capillary pressure and electric permittivity hysteresis in multi-phase flow through porous media*, Geophysics Letters, Vol. 72, Issue 3, pp. A41-A45; doi: 10.1190/1.2714684.

Plug, W., E. Slob, J. van Turnhout, and J. Bruining (2007), *Capillary pressure as a unique function of electric permittivity and water saturation*, Geophys. Res. Lett., 34, L13306, doi:10.1029/2007GL029674.

Appeared in "AGU Journal Highlight, August 2007"

Plug, W.J., Bruining, J., *Capillary pressure for the sand - CO2 - water system under various pressure conditions. Application to CO2 sequestration*, Accepted for publication in Advances in Water Resources, March 2007.

Plug, W.J. "Measurements of capillary pressure and electric permittivity of gas-water systems in porous media at elevated pressures. *Application to geological storage of CO_2 in aquifers and wetting behavior in coal".* Dissertation, Delft, 2007.